Measurement of the production cross-section ratio $\frac{\sigma_{t\bar{t}j}}{\sigma_{t\bar{t}X}}$ in $106.0 \pm 4.1 \ \mathrm{pb}^{-1}$ of data collected by CDF during Run1A+1B of the Tevatron

BY

Christopher Scott Hill

B.A. (Dartmouth College, New Hampshire) 1994

M.S. (University of California, Davis) 1998

DISSERTATION

Submitted in partial satisfaction of the requirements for the degree of

DOCTOR OF PHILOSOPHY

in

Physics

in the

OFFICE OF GRADUATE STUDIES

of the

UNIVERSITY OF CALIFORNIA

DAVIS

Approved:

Prof. Richard Lander

Prof. Dave Pellett

Prof. Jack Gunion

Committee in Charge

2001

i

Christopher Scott Hill

September 2001

Physics

Measurement of the production cross-section ratio $\frac{\sigma_{t\bar{t}j}}{\sigma_{t\bar{t}X}}$ in 106.0 ± 4.1 pb^{-1} of data collected by CDF during Run1A+1B of the Tevatron

Abstract

A measurement of the rate of gluon radiation in top events has been performed on the 106.0 ± 4.1 pb^{-1} of data collected collected by CDF during Run1A+1B of the Tevatron. Events are selected with a lepton, missing energy, and 2 or more jets, of which at least one is b-tagged with a reconstructed secondary vertex. Jet multiplicity distributions are generated using `MADGRAPH` matrix elements for the processes $qq, gg \rightarrow t\bar{t}; qq, qg, gg \rightarrow t\bar{t}g; qq \rightarrow t\bar{t}gg$ inserted into `PYTHIA 6.115 + QFL`$'$. A binned likelihood fit is performed on the data and relative cross-sections are extracted as a function of jet energy. These cross-sections are compared to leading order theoretical predictions. Agreement within errors is found. The performance of this measurement given the increased statistics of Run2A of the Tevatron is estimated.

Acknowledgements

This thesis is dedicated to my grandfather, Carmine Masullo.

I would like to thank the following people who have helped make this thesis possible:

- At BBPHS Gary Weeks, who stimulated my mathematical interests.

- At Dartmouth, Bill Doyle, who re-kindled my interest in experimental physics (although he may not know it).

- At UC Davis, Dick Lander, Dave Pellett, Jack Gunion, and Max Chertok for their useful discussions regarding this thesis. I also acknowledge the UCDHEP group for their generous support.

- At CDF, the FNAL silicon and Yale DAQ people, especially David Stuart, for taking me under their wings when I first arrived. UCD was not in the CDF collaboration at the time and I appreciate them giving me the opportunity to find my way within CDF. I would like to thank Joe Incandela for introducing me to this measurement. I am grateful to Joe and David as well as Joel Goldstein, Tim Nelson, Auke-Pieter Colijn, Doug Glenzinski, Tony Affolder, and Amy Connolly for their insightful comments on this analysis. Thanks also to Mark Kruse, Pierre Savard and the CDF top group.

- At Fermilab, Dave Rainwater in the theory division, with whom I developed the Monte Carlo employed in this thesis.

- I would also like to thank my friends and family for all their love and support, especially Amy Connolly, Kevin Stineman, John & Gayle Thayer whom I miss since I have left CA, my Uncle Bob & Aunt Eileen for their hospitality whenever I am in CA, and my parents Richard & Nancy Hill for always nurturing my scientific interests.

Contents

List of Figures

List of Tables

Chapter 1

Introduction

Surely, even before human beings could articulate the word "science", they had looked to the heavens with wonder, and asked what is the world made of? How does it work? It is in no small part due to to this legacy of curiosity that I find myself a student of science, and of particle physics in particular. Physics is the science that studies matter, energy and their interactions. Particle physics is the application of this study to its most fundamental scale - the interactions of matter's elementary constituents. Thus particle physics is at once comprehensive (all things are composed of matter) and irreducible, seductively intimating that it holds the key to the deepest secrets of the universe.

Particle physicists come in two varieties that play complementary roles in this quest to understand nature: theorists who formulate mathematical models of particles and their interactions, and experimentalists who test these models in the laboratory. The physics of matter such as protons, neutrons and electrons is the domain of other fields of investigation, such as nuclear physics or chemistry. Particle physics is concerned with matter that does not exist on the energy and time scales of human observation. Thus, much as the biologist needs a microscope to study the workings of the cell, the experimental particle physicist too needs tools to test the musings of his theoretical counterpart. The principal tools which experimentalists employ in these tests are the particle accelerator, which speeds particles up to nearly the speed of light, and the detector which records the debris resulting from smashing this highly

energetic particle into a target.

In Batavia, Illinois at Fermi National Accelerator Laboratory, there is the world's highest energy particle accelerator called the Tevatron, in which protons and anti-protons are made to collide head on. There are two detectors to study these collisions, each operated by an international collaboration of several hundred particle physicists, the Collider Detector at Fermilab (CDF) and D0. These experiments collected data from 1989 - 1995, culminating in the discovery of a particle called the top quark.

In this thesis, a measurement of the production cross-section ratio $\frac{\sigma_{t\bar{t}j}}{\sigma_{t\bar{t}X}}$ is presented. This is an attempt to quantify the rate of gluon[1] radiation in the events that formed the top quark discovery at CDF. The Tevatron still holds a monopoly on the production of these top quarks, therefore this measurement represents the first of its kind in the world.

In Chapter 2, the theoretical framework for this measurement is outlined. The Standard Model of particle physics is introduced, including the theory of strong interactions, called Quantum Chromodynamics, which governs gluon radiation. A discussion of top production, decay, and gluon radiation, at the Tevatron is given. Theoretical motivations for the measurement are advanced.

In Chapter 2, the laboratory environment is discussed. A brief description of the Tevatron collider is given. The CDF detector is explained in detail, with emphasis

---

[1]A gluon is another fundamental particle in the Standard Model - see Chapter 2.

on detector sub-systems that were critical in this analysis.

In Chapter 4, selection of data collected by CDF is discussed. A data sample rich in top events is created.

In Chapter 5, analysis of CDF's top events is performed. The numbers of $t\bar{t}$ events with and without gluon radiation are extracted. A discussion of systematic errors is given. The $t\bar{t}j$ cross-section ratio is computed.

In Chapter 6, a comparison between the theory and data is given. Theoretical predictions for the rate of gluon radiation are compared to those rates measured in the data.

In Chapter 7, conclusions are drawn, and implications are discussed.

In Appendix A, a list of selected events is given.

In Appendix B, a list of hardware triggers required is given.

In Appendix C, the choice of cuts used to avoid the singularities in the matrix elements is discussed.

In Appendix D, the choice of the cut used to match partons to jets when making the jet multiplicity templates is discussed.

In Appendix E, the expected performance of this analysis in Run 2A is estimated.

In Appendix F, the construction of Feldman-Cousins confidence intervals is explained.

Chapter 2

Theory and Motivation

2.1 Standard Model of Particle Physics

The Standard Model(SM) of particle physics is the currently accepted theory of matter and its (non-gravitational) interactions. The SM holds that all matter is made up of fermions that interact via the exchange of bosons. These interactions are what is commonly called a force. The boson that mediates the familiar electromagnetic interaction is none other than the photon[1], symbolized as γ. There are three bosons that mediate the weak nuclear interaction responsible for radioactive decay of unstable nuclei[2], the W^-, W^+, and Z^0. There are eight bosons responsible for the strong nuclear interaction which binds quarks into hadrons (e.g. protons and neutrons). These bosons are aptly named gluons, unimaginatively symbolized as g.

The SM is an example of what is known as a gauge theory, and the bosons listed above are sometimes referred to as gauge bosons. They are called this because the interaction is invariant[3] under a type of mathematical operation called a gauge transformation. A gauge transformation is defined by

$$\Phi \to \Phi' = e^{i\alpha^a t^a}\Phi \qquad (2.1)$$

where $\Phi = \Phi(\overrightarrow{x}, t)$ is a fermion or boson field and t denotes the generators of the

---

[1] The photon is the quanta of electromagnetic radiation, i.e. light

[2] In β-decay, for example, when a neutron decays to a proton and an electron it does so by emitting a virtual W^- which then decays to the observable electron and neutrino.

[3] Invariance here has a specific technical meaning. It means that the Lagrangian describing the interaction does not change in a way that effects the equations of motion, i.e. the physics is not changed by this mathematical re-formulation.

gauge group[4]

The SM employs three gauge groups to describe the three fundamental forces ($U(1)$ for the electromagnetic interaction, $SU(2)$ for the weak interaction, and $SU(3)$ for the strong interaction) and is therefore called an $U(1) \otimes SU(2) \otimes SU(3)$ theory. The fermions are classified as quarks, which participate in the $SU(3)$ interaction[5] and leptons which do not. There are six flavors of each, they are further grouped into $SU(2)$ isospin doublets[6] forming three families, or generations. The particles of the Standard Model are shown in Fig 2.1.

The SM is a very successful theory. The predictions of the $U(1)$ theory of the electromagnetic interaction, called Quantum Electrodynamics (QED) agree with many experiments up to eight significant digits making it "the most stringently tested - and the most dramatically successful - of all physical theories."[1] The Electroweak theory advanced by Glashow, Salam and Weinberg (GSW) [2][3][4] is the $U(1) \otimes SU(2)$ component. The GSW prediction of the existence and masses of the $W^{\pm}, Z^0$ bosons, and their subsequent discovery by the UA1[5][6] and UA2[7] experiments at CERN in 1983 remains one of the triumphs of high energy particle physics to this day. The $SU(3)$ component of the SM is called Quantum Chromodynamics (QCD) which has

---

[4]A group is an abstract mathematical entity which is useful in describing the symmetry of a system. For example, a system which is invariant under spatial rotations is said to have $SO(3)$ symmetry.

[5]This is also known as the strong nuclear force or color.

[6]A particle that feels the weak force is either isospin "up"- the top element of the doublet or isospin "down" - the bottom element. Isospin is not a "real" spin, but refers only to their orientation in the abstract $SU(2)$ space.
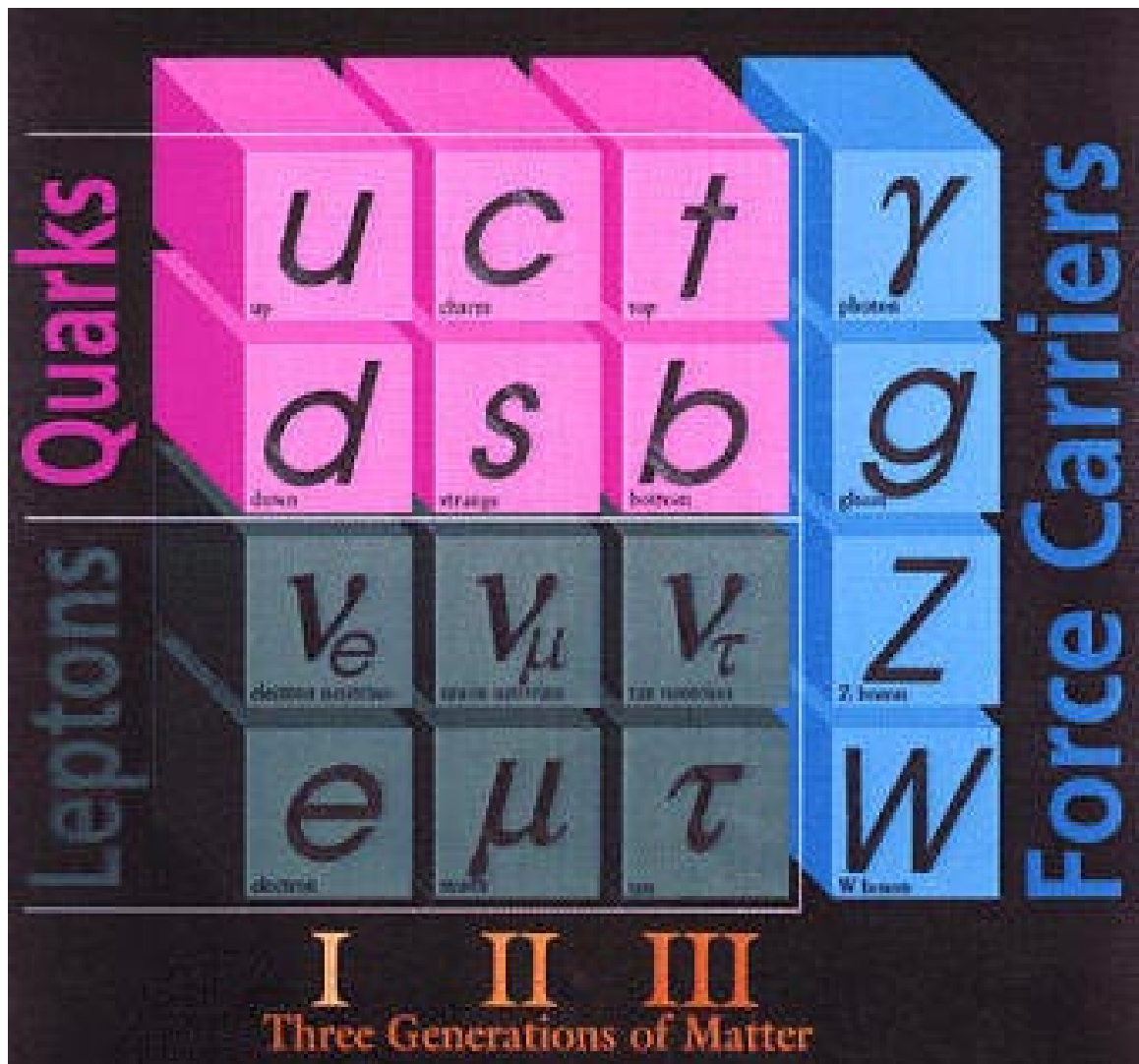
Figure 2.1: *Particle content of the Standard Model. From [8].*

been tested at high energy physics laboratories around the world since its inception 25 years ago. While QCD, owing to the very nature of the strong interaction as we shall see, has inherent calculational difficulties, the predictions it has been able to make have agreed well with experiment such that "hardly anybody seriously doubts its validity."[9]

2.1.1   Quantum Chromodynamics

This thesis, a measurement of gluon radiation in top events, is really a QCD measurement. Therefore, what follows is a brief summary of the salient aspects of this theory.

QCD, is best introduced via analogy to its simpler predecessor QED. QED describes the electromagnetic interactions of charged particles.

The strength of this interaction is given by the electromagnetic coupling constant e, which is simply the electromagnetic charge and is related to the fine structure constant, α by[7]

$$\alpha = \frac{e^2}{4\pi} \tag{2.2}$$

QED processes are calculated using a perturbation[8] expansion in e. The lowest order (tree-level) process is depicted in Fig 2.2, called a Feynman diagram, which

---

[7]Here, and throughout this thesis, Heaviside-Lorentz units are employed where $\hbar = c = 1$.

[8]A perturbation expansion is a power series expansion where each successive term is smaller than the previous one. Thus, for QED, interactions are principally described by the terms linear in e with small corrections coming from the terms quadratic in e, and even smaller corrections from even higher-order terms.

shows a fermion and an anti-fermion scattering via photon exchange.

While calculation of tree-level QED processes is trivial, treatment of higher-order (loop) diagrams present a technical problem in that they contain divergent momentum integrals, *i.e.* infinities. The removal of these infinities is accomplished by the redefinition or renormalization of the electric charge as follows:[9]

$$e_R^2(q^2) \rightarrow \frac{e^2}{1 - Ce^2 \ln\left(\frac{q^2}{-M^2}\right)} \tag{2.3}$$

where q is momentum and M is mass. Note that through the q^2 dependence the strength of the interaction depends on the scale of the interaction. At higher energy scales, the strength of the electromagnetic coupling increases. The physical interpretation of this "running" of the coupling constant is that virtual e^+e^- pairs in the vacuum screen the bare electric charge at lower energies, making the apparent charge less.[9] At sufficiently high scales the coupling constant is so large that perturbative calculation becomes impossible and the theory breaks down.

Similarly, QCD describes the strong interactions of quarks and gluons. The strengths of these interactions are proportional to the strong coupling constant g, which is in analogy to the electromagnetic fine structure constant, related to α_s by

$$\alpha_s = \frac{g^2}{4\pi} \tag{2.4}$$

Tree-level calculation of QCD processes, such as quark-antiquark annihilation, depicted in Figure 2.3, proceeds exactly as in the QED case with the addition of a

[9]This phenomenon is known as vacuum polarization.
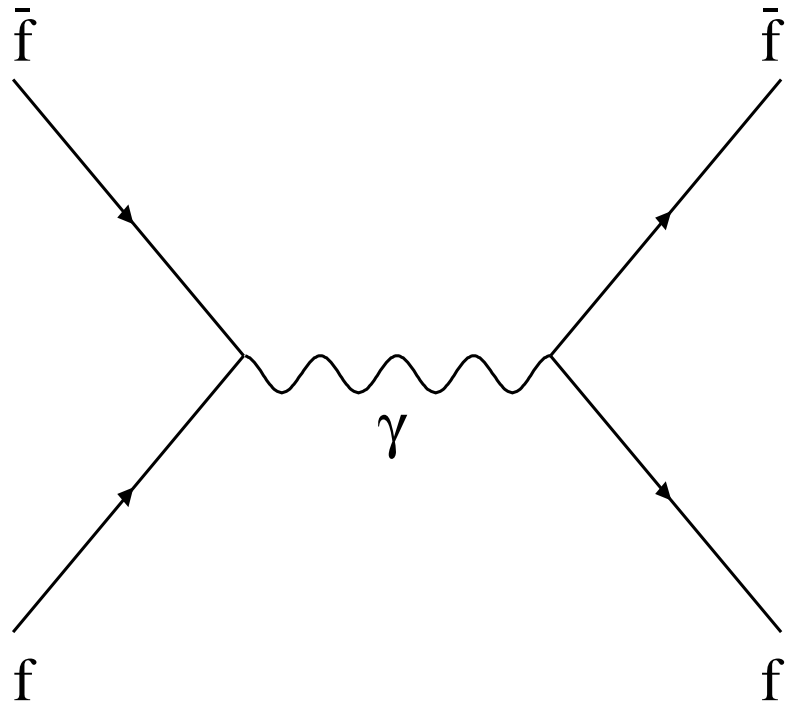
Figure 2.2: *Feynman Diagram for tree-level QED interaction.*

color factor to account for the different colors of the incoming and outgoing quarks. In calculation of loop corrections in QCD, however, the analogy with QED begins to break down. Renormalization is required and proceeds as in QED, leading to the following analogous expression for the renormalized strong coupling constant[9]

$$\alpha^2_{s_R}(q^2) \rightarrow \frac{\alpha^2_s}{1 + \frac{11 - \frac{2}{3}N_f(q^2)}{4\pi}\alpha^2_s \ln(\frac{q^2}{-M^2})} \tag{2.5}$$

which is often re-written with the introduction of a parameter called Λ_{QCD}.

$$\Lambda_{QCD} = \Lambda(M) \tag{2.6}$$

leading to the following expression for the running of α_s:[9]

$$\alpha^2_s(q^2) = \frac{4\pi}{\left(11 - \frac{2}{3}N_f(q^2)\right)\ln(\frac{-q^2}{\Lambda^2})} \tag{2.7}$$

where N_f is the number of quark flavors with $m \ll \frac{1}{2}\sqrt{-q^2}$

Here we see the principal difference between QED and QCD, whereas α increased with energy scale, α_s decreases, see Figure 2.4. As Λ_{QCD} gets small, the color force becomes stronger, leading to quark confinement (why quarks do not exist as free particles) . Conversely, as Λ_{QCD} gets large, the strong coupling becomes weaker and weaker, leaving quarks unbound, a phenomenon known as asymptotic freedom. Moreover, it is only in this region where quarks are asymptotically free that α_s is small enough that QCD is perturbative. That is to say, QCD calculations cannot be done accurately using perturbative techniques, *i.e.* expansion in Feynman diagrams as in QED, for all but the highest energy scale interactions!
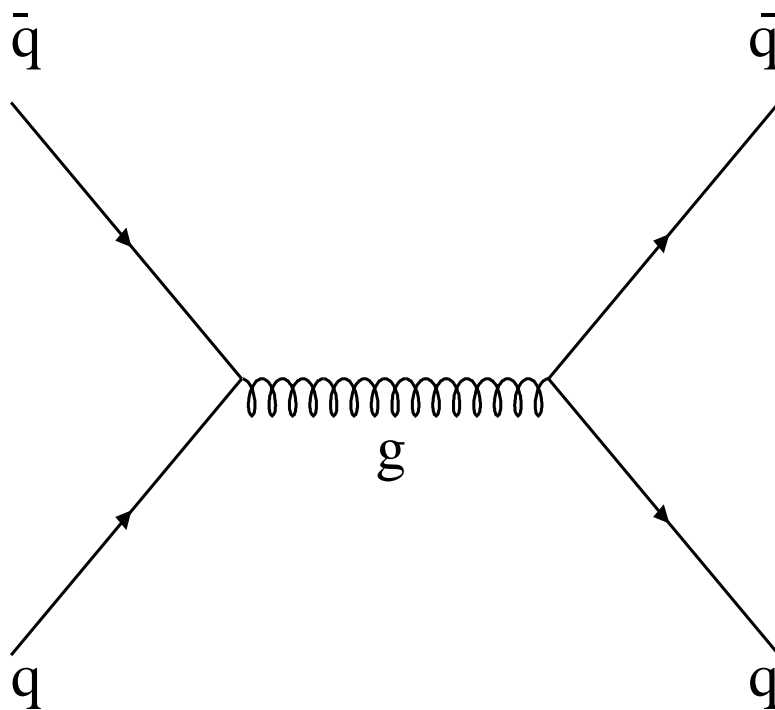
Figure 2.3: *Feynman diagram for $q\bar{q}$ strong interaction.*
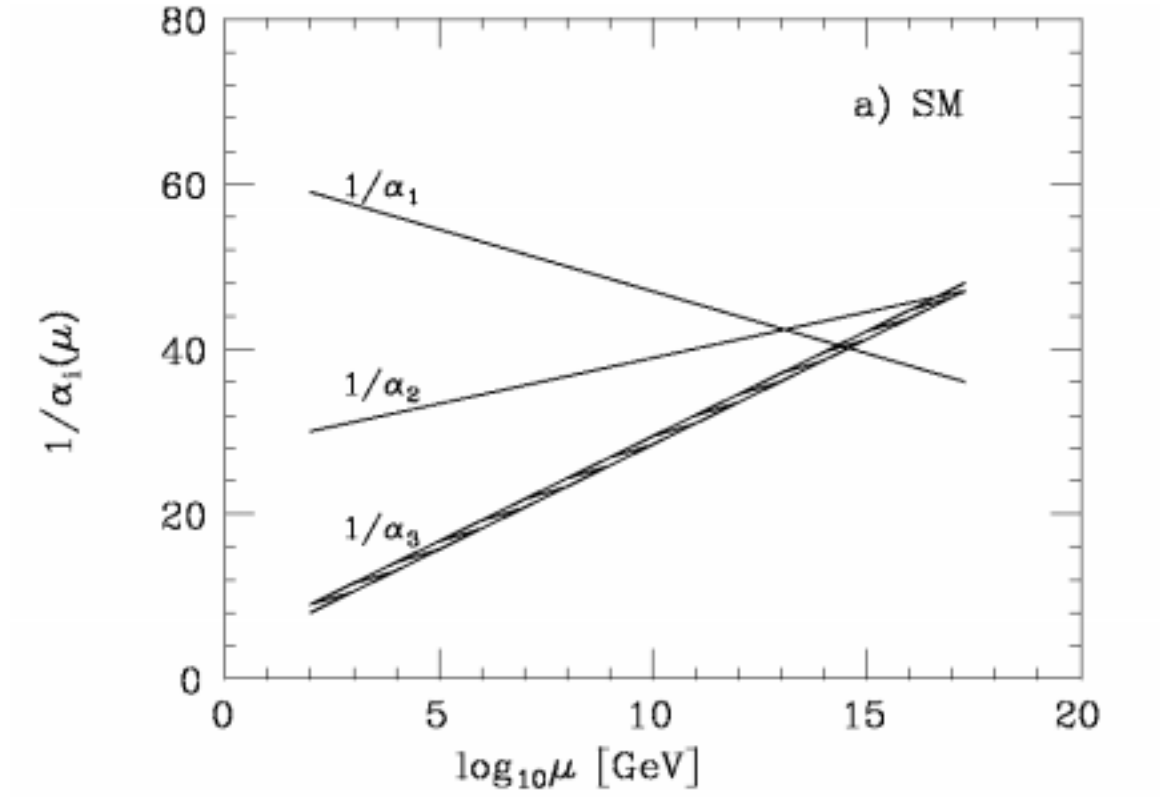
Figure 2.4: *Illustration of the "running" of the coupling constants in the standard model as a function of energy scale. α_1 is the EM coupling constant, α_2 is the weak coupling constant, and α_3 is the strong coupling constant. Adapted from [10].*

This thesis presents a measurement of gluon radiation at the energy scale associated with top, anti-top production. This measurement is the first such measurement at this energy scale. Thus, this measurement serves as a important check on the predictions of perturbative QCD.

2.2   The Top Quark at the Tevatron

2.2.1   Top Production

In 1995 the top quark was discovered by the CDF collaboration at the Fermilab Tevatron collider[11]. The production of top quarks at the Tevatron occurs through three primary processes: pair production by quark/anti-quark annihilation or gluon fusion (See Figure 2.5), Drell-Yan production of single top (See Figure 2.6), and W-gluon fusion (See Figure 2.7). Results of calculations of top quark production cross sections[10] at Tevatron energies are shown in Figure 2.8. This plot illustrates that, at the Tevatron, tops are dominantly pair produced, of which 90% occurs through quark/anti-quark annihilation and 10% through gluon fusion.

---

[10]Cross section is a high energy physicist's probability for a given process. It can be converted to the number of expected events when multiplied by the integrated luminosity or data collected by an experiment ($N = \sigma \int L dt$).
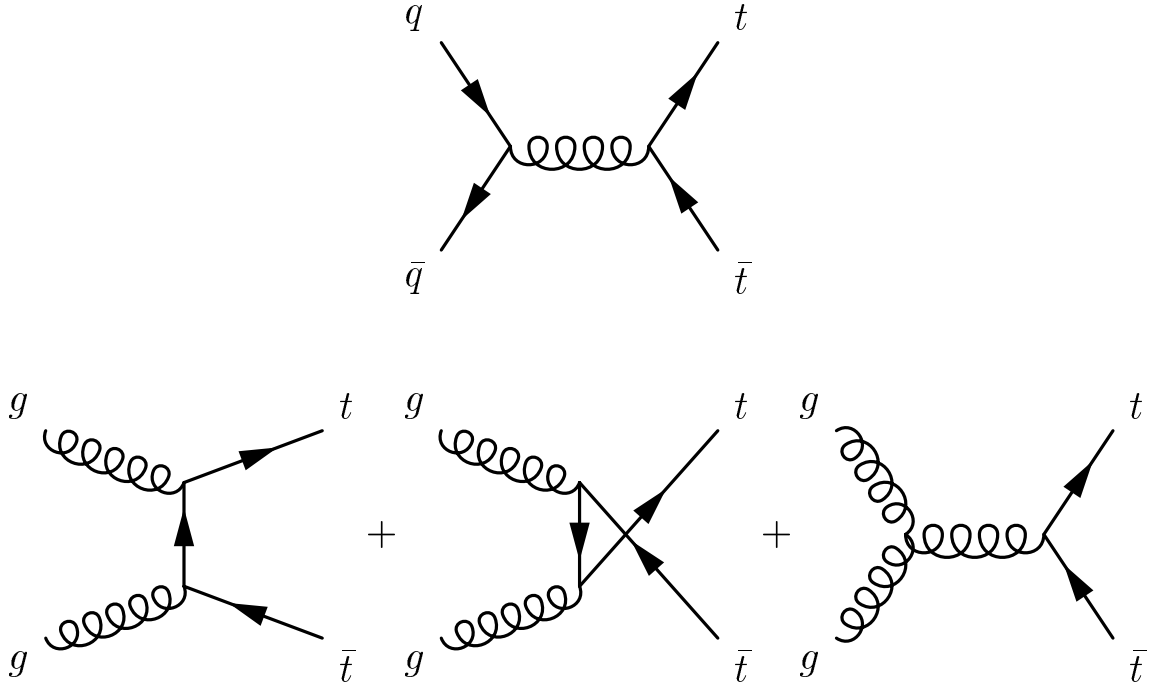
Figure 2.5: *Tree-level $t\bar{t}$ production diagrams. From [12].*
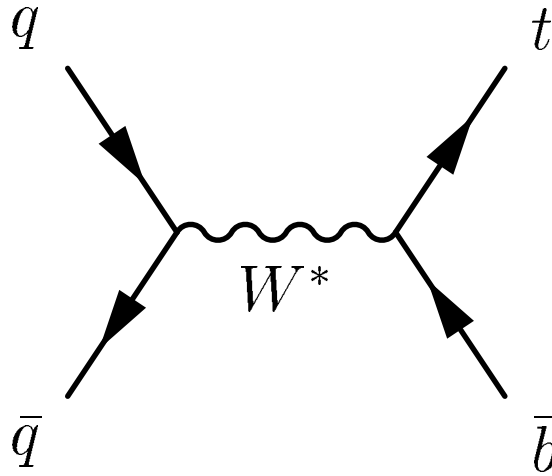
Figure 2.6: *Single top production via drell-yan mechanism. From [12].*
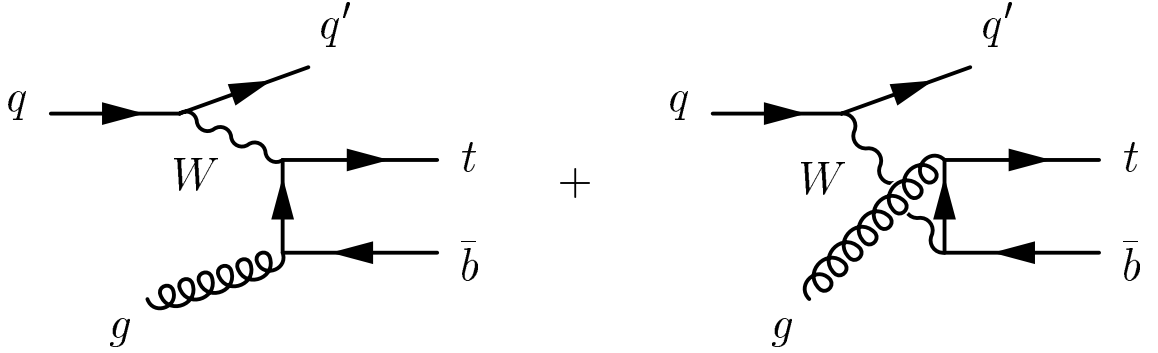
Figure 2.7: *Single top production via Wg fusion. From [12].*

2.2.2 Top Decay

Top quarks produced at the Tevatron nearly always decay via the weak interaction to a bottom quark ($t \rightarrow bW$). The W itself then decays hadronically ($W \rightarrow qq'$) or leptonically ($W \rightarrow \ell\nu$). Thus, $t\bar{t}$ events at the Tevatron are classified into different final state topologies by the decay mode of either W in the event. The various permutations of these decays and their relative frequencies (branching fractions) are given in Table 2.1.

2.2.3 Gluon Radiation from Top

Top quarks, being colored objects, can radiate a gluon, much like a charged object (*e.g.* electron) may radiate a photon. This process is illustrated by the Feynman diagram in Figure 2.9. Top quarks are not the only colored objects in a $t\bar{t}$ event. Thus, gluons can also be radiated from the incoming quark/anti-quark pair or the hadronic decay products of the top/anti-top pair. Since there are these multiple
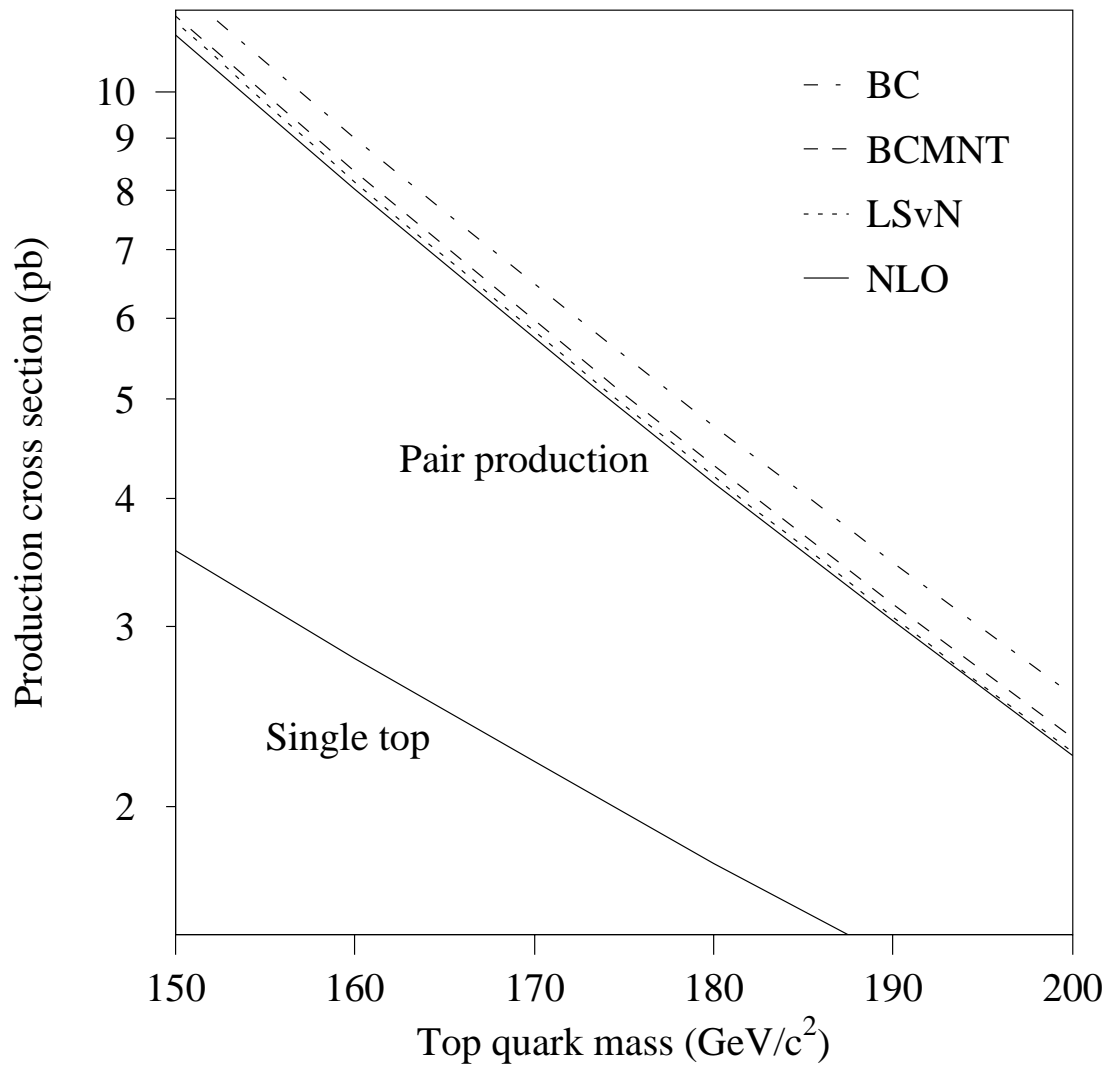
Figure 2.8: *Top production cross sections at $\sqrt{s} = 1.8$ TeV. From [12].*

Table 2.1: *Decay modes for a $t\bar{t}$ pair and branching fractions. From [12].*

	$W \to e\nu_e$ (1/9)	$W \to \mu\nu_\mu$ (1/9)	$W \to \tau\nu_\tau$ (1/9)	$W \to qq'$ (2/3)
$W \to qq'$ (2/3)	12/81 (e+jets)	12/81 (μ+jets)	12/81 (τ+jets)	36/81 (all hadronic)
$W \to \tau\nu_\tau$ (1/9)	2/81 ($e\tau$)	2/81 ($\mu\tau$)	1/81 ($\tau\tau$)	
$W \to \mu\nu_\mu$ (1/9)	2/81 ($e\mu$)	1/81 ($\mu\mu$)		
$W \to e\nu_e$ (1/9)	1/81 (ee)			

sources of gluon radiation in top events, the naive classification of radiation as either initial or final state is inadequate. In fact, Lynne Orr, a prominent theorist in this field, states "there is *no* meaningful separation of [gluon radiation] jets into 'initial-' and 'final-state' radiation" because at any point in phase space the $t\bar{t}$ + jets cross-section contains contributions from the incoming $q\bar{q}, gg$, the produced $t\bar{t}$, and the t, b, qq' quarks in the decay process $t \rightarrow bW \rightarrow qq'$, as well as interferences between them[13].

Orr, however, offers an alternative classification scheme where gluon radiation in top events is separated into production and decay phases with interferences between them as follows:

> Production emission is defined as those regions of phase space for which the masses of the $W^- + \bar{b}$ and $W^+ + b$ systems reconstruct the top mass. Decay emission is defined as those regions of phase space for which the either the $W^- + \bar{b}$ or $W^+ + b$ system requires the inclusion of the extra jet to give the top mass."

This classification is implemented via the following relations:

$$S_{prod} = |((p_{W^+} + p_b)^2 - m_t^2 + im_t\Gamma_t) \times ((p_{W^-} + p_{\bar{b}})^2 - m_t^2 + im_t\Gamma_t)| \qquad (2.8)$$

$$S_1 = ((p_{W^+} + p_b)^2 - m_t^2 + im_t\Gamma_t) \times ((p_{W^-} + p_{\bar{b}} + p_{jet})^2 - m_t^2 + im_t\Gamma_t) \qquad (2.9)$$

$$S_2 = ((p_{W^+} + p_b + p_{jet})^2 - m_t^2 + im_t\Gamma_t) \times ((p_{W^-} + p_{\bar{b}})^2 - m_t^2 + im_t\Gamma_t) \qquad (2.10)$$

$$S_{dec} = \min(|S_1|, |S_1|) \qquad (2.11)$$

An event is production phase if $S_{prod} < S_{dec}$ and decay phase if $S_{dec} < S_{prod}$. This definition is gauge invariant and valid in all regions of phase space.

In this thesis, I present a measurement of the ratios of the production cross-section for $t\bar{t} + 1$ jet relative to the inclusive cross-section. This is, in essence, a measurement of hard gluon radiation in top events, where hard means energetic enough to produce a distinct observable jet in the CDF detector. In this limit, where the contributions from soft gluon emissions are removed by experimental jet reconstruction cuts (*e.g.* E_T^{min}), most events have either $S_{prod} \ll S_{dec}$ or $S_{dec} \ll S_{prod}$. For such events, the production phase is well described by diagrams where radiation is off the incoming partons, propagator or the top before it decays, *i.e.* off-shell tops. The dominant decay phase diagrams are those with emissions off on-shell tops and off the hadronic decay products. The interference is only relevant for gluons with energy comparable to the top width[13].

2.2.4 Motivation

A measurement of tt+jets cross-sections is motivated for several reasons.Gluon radiation is an important systematic uncertainty in any measurement of the top quark mass[14]. Gluons can radiate from the incoming quark/anti-quark pair, the top/anti-top pair, or the the hadronic decay products of the $t\bar{t}$ resonance. Depending on the E_T threshold and cone cut employed in the jet clustering algorithm, the radiation may
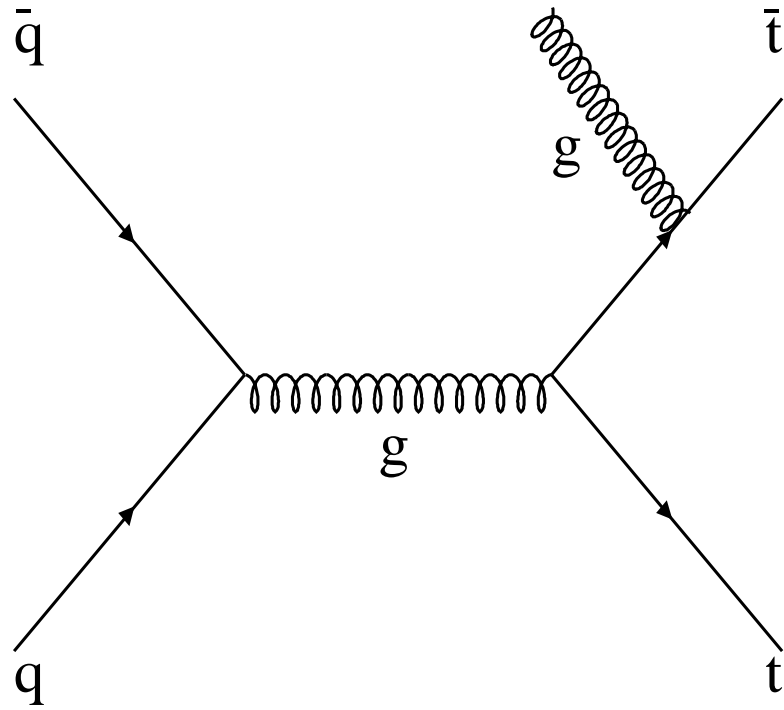
Figure 2.9: *Possible feynman diagram for gluon radiation in a top event.*

or may not be reconstructed as a distinct jet. If gluon jets are formed, for a top mass measurement, it is important to know from which parton the radiation originated. If, for example, a gluon jet is observed which was radiated from the incoming quark, then it clearly should not be included in the $t\bar{t}$ mass reconstruction, whereas if it was radiated from a b quark from the decaying top, this extra jet clearly needs to be incorporated into the top quark mass. Knowledge of the rate of radiation in top events will help to quantify this systematic error.

The largest theoretical uncertainty associated with top physics calculations is the renormalization scale choice which can lead to a cross-section variation as large as 40%. By comparing the measured rate of gluon radiation in top events to theoretical calculations with varied renormalization scale choices for the evaluation of α_s and parton distribution functions, the renormalization scale that the data supports best may be obtained, providing theorists with an experimentally motivated scale choice, thereby reducing the large uncertainty associated with these types of calculations.

Gluon radiation in top events is also the largest, and least well understood background to the search for a Standard Model Higgs boson via $t\bar{t}H$, which may be possible at the Tevatron given enough luminosity[15].

Finally, although the current measurement is statistics limited, a procedure has been developed which may be repeated in Run 2 taking advantage of the thousands of $t\bar{t}$ events CDF will observe, greatly reducing the statistical uncertainty of the result.

Chapter 3

Experimental Apparatus

3.1   The Tevatron

The Tevatron is a particle accelerator located at Fermi National Accelerator Laboratory (Fermilab) in Batavia, IL. The Tevatron is a ring, 6.28 km in circumference, which houses a beam of protons traveling at near the speed of light, and a beam of anti-protons traveling equally fast in the opposite direction. These beams are made to cross at two points around the ring causing the energetic collisions which particle physicists study. A schematic view of the Fermilab accelerator complex is shown in Figure 3.1. The acceleration/collision process is briefly explained in what follows.

3.1.1   Proton Source

Protons are harvested from molecular hydrogen, H_2. Negative hydrogen ions, H^-, are formed by the addition of electrons. In the Cockroft-Walton pre-accelerator a positive voltage is applied, accelerating these ions to 750 keV. Next, the ions enter a 150 m long linear accelerator (LINAC) where oscillating electric fields accelerate the ions to 400 MeV. At the end of the LINAC, the ions pass through a thin copper foil which strips the electrons, leaving only bare protons. The protons enter a 475 m circumference synchrotron accelerator called the Booster, where after approximately 20,000 revolutions, the protons have been accelerated to 8 GeV. Next the protons enter the Main Ring, a 6.28 km circumference synchrotron, where they are accelerated to 150 GeV. Finally, the protons are injected into the Tevatron, situated just below
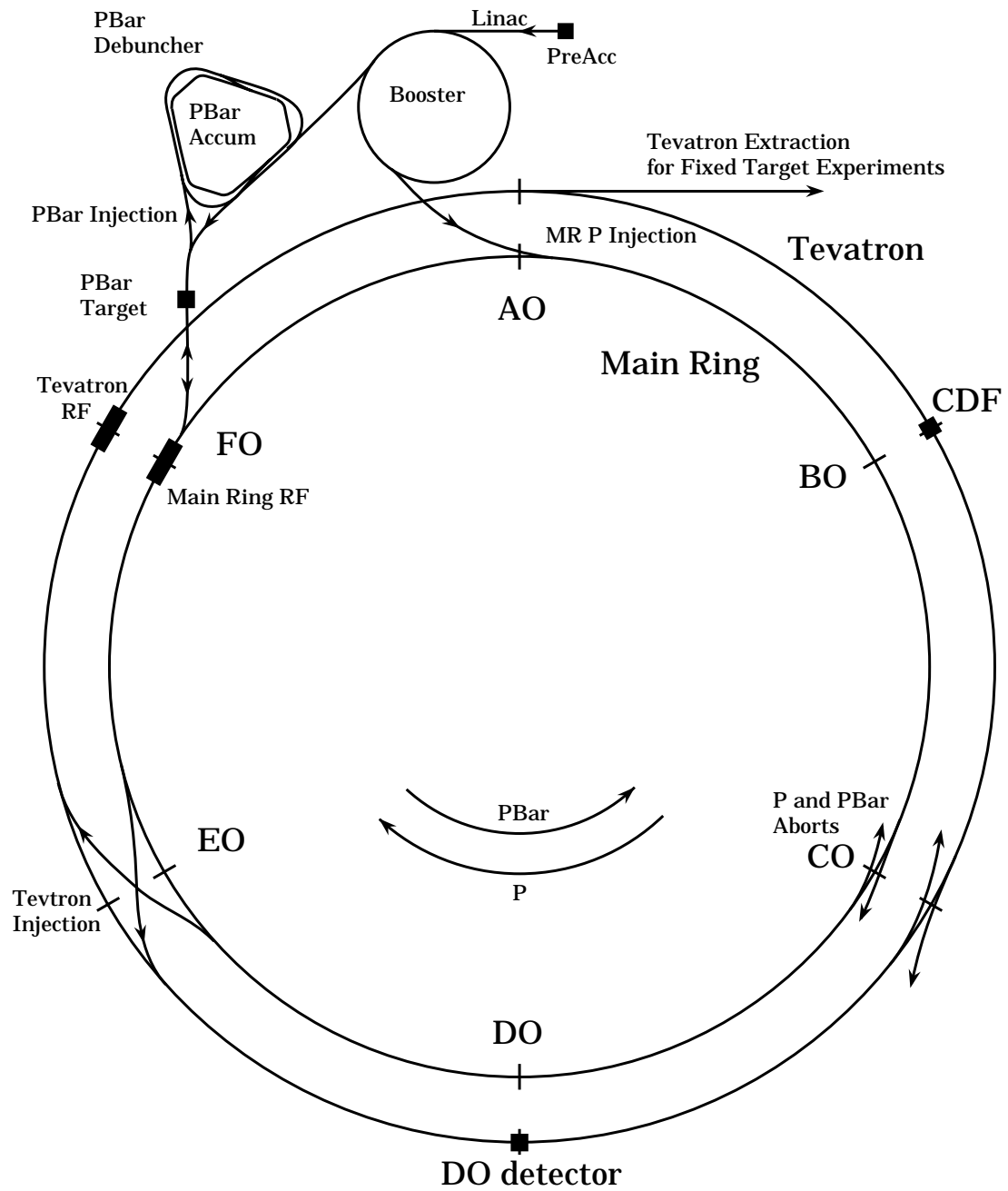
Figure 3.1: *Fermi National Accelerator Laboratory complex. From [16].*

the Main Ring, where they complete their acceleration to the colliding energy of 900 GeV. Unlike the other synchrotrons in the Fermilab accelerator complex which employ conventional electromagnets for steering and focusing the beam, the Tevatron uses super-conducting magnets.

3.1.2   Anti-proton Source

Anti-protons, not being present in ordinary matter, are more difficult to obtain than protons. A beam of 120 GeV protons is diverted from the Main Ring and forced to collide with a tungsten target. In the ensuing nuclear interactions many secondary particles are produced, including anti-protons, which are focused into a beam using a lithium lens. Anti-protons of about 8 GeV are filtered from this beam using a pulsed magnet as a charge-mass spectrometer and passed to the Debuncher. The anti-protons leave the target at a wide range of energies, positions and angles. Stochastic cooling is used to make the beam more homogeneous. Moreover, since the anti-protons are produced from "bunched" protons in the Main Ring, they too are bunched, *i.e.* arrive with a narrow spread in time. The Debuncher undoes this effect, converting the anti-protons into a beam with a large time spread, but more narrow spread in energy. From the Debuncher, anti-protons are transferred to the Accumulator, a set of concentric storage rings with radii of about 80 m. Anti-protons are "stacked" in the Accumulator at a rate of 4×10^{10} per hour until 100×10^{10} are

stored, at which point they are ready to be reverse injected into the Main Ring for acceleration and subsequent injection into the Tevatron.

3.1.3 Collisions

When in colliding mode, six bunches of 2×10^{11} protons and six bunches of 3×10^{10} anti-protons are injected into Tevatron in opposite directions. The bunches are 50 cm in length. When these bunches have been accelerated to 900 GeV they are made to collide in the CDF and D0 experimental areas. These collisions occur every $3.5\mu s$ for up to 20 hours, at which point the ring is emptied and refilled with new bunches of protons and anti-protons in preparation for the next run. The collisions do not always occur at the same exact point in space. In fact, the luminous region, as it is called, is a gaussian distribution about the nominal interaction point with a width of 30 cm in the longitudinal (along the beam axis) direction and 35 μm in the transverse direction.

Instantaneous luminosity is given by the following relation:

$$\mathcal{L} = \frac{N_p N_{\bar{p}} B f_0}{4\pi\sigma^2} \tag{3.1}$$

where N_p is the number of protons per bunch, $N_{\bar{p}}$ is the number of anti-protons per bunch, B is the number of bunches of each type, f_0 is the revolution frequency of the bunches, and σ^2 is the cross-sectional area of a bunch. Thus, due to transverse spreading of the beam, and losses due to collisions, instantaneous luminosity falls

Run	Average $\mathcal{L}$	Peak $\mathcal{L}$
Run 1A	$0.54 \times 10^{31} cm^{-2} s{-}1$	$0.92 \times 10^{31} cm^{-2} s^{-1}$
Run 1B	$1.6 \times 10^{31} cm^{-2} s{-}1$	$2.8 \times 10^{31} cm^{-2} s^{-1}$

Table 3.1: *Average and peak instantaneous luminosities during Run I of the Tevatron.*

off exponentially within a given run. Peak and average instantaneous luminosities achieved during Run 1A (1992-1993) and Run 1B (1994-1995) of the Tevatron are given in Table 3.1.

3.2   The CDF Detector

The Collider Detector at Fermilab is located at the B0 interaction point of the Tevatron. CDF is a 5,000 ton, multi-purpose, particle detector designed to study high-energy $p\bar{p}$ collisions by precise measurements of the observable debris from the interaction: electrons, photons, muons, and jets[1]. The measurements made include the energy, momentum, origin, and trajectory, of the debris particles. In CDF these measurements are accomplished by a set of detector sub-systems working alone or in combination. These sub-systems are described in subsections 3.2.1-3.2.5. A schematic of the CDF detector, showing the various sub-systems is given in Figure 3.2. A three-dimensional rendering of the CDF detector is displayed in Figure 3.3.

---

[1]Jets are described in subsection 4.8.1.

Figure 3.2: *Schematic of the Collider Detector at Fermilab. From [16].*

CDF Detector

Backward
Muon System

SVX

Central Muon
Upgrade

Central Muon
Extension

Forward
Muon System

Calorimeters

Magnet Yoke

Steel Walls

Solenoid

Tracking
Chambers

Low Beta Quads
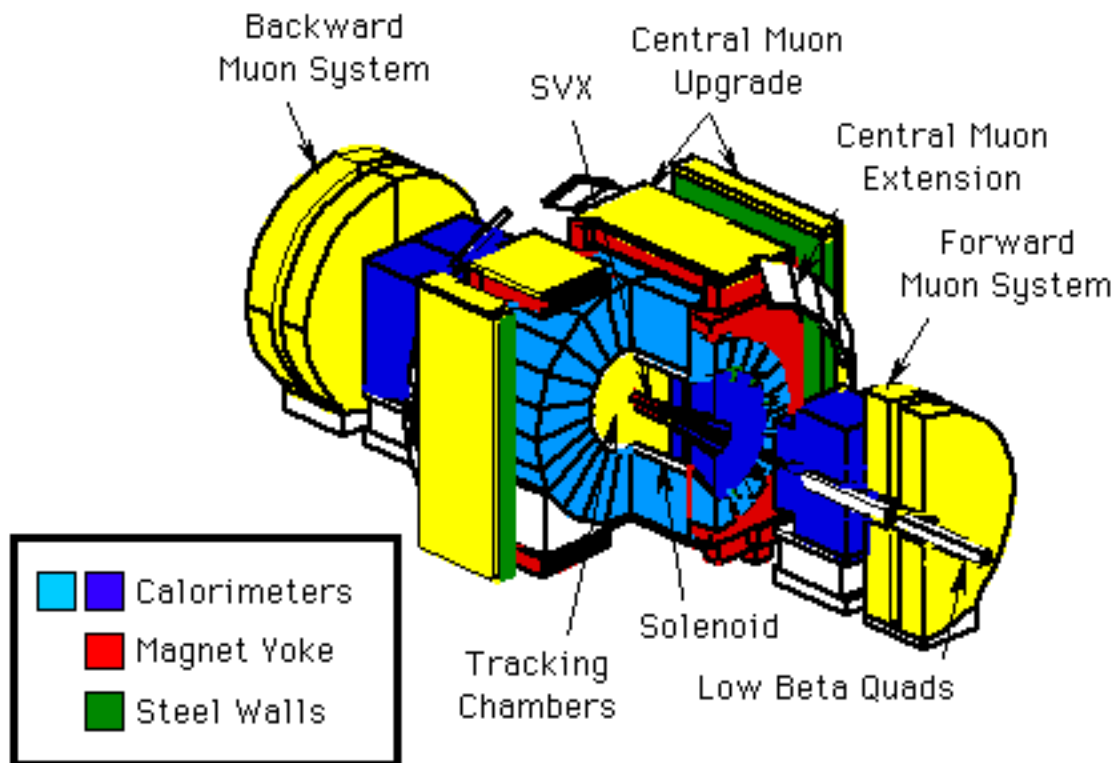
Figure 3.3: *Three dimensional rendering of the Collider Detector at Fermilab. From [16].*

CDF is cylindrically symmetric about the beam-line and forward-backward symmetric about the interaction region. The coordinate system used at CDF defines $x = 0, y = 0, z = 0$ to be the nominal interaction point, with positive z in the direction of the proton beam, and negative z in the direction of the anti-proton beam. The x direction is taken to be orthogonal to the z direction, lying in the plane of the Tevatron, with positive x pointing towards the center if the ring. The y direction is the normal to the plane of Tevatron with positive y pointing upwards. The polar angle, θ, is defined from 0 (along the positive z axis) to π (along the negative z axis). The azimuthal angle, ϕ, is defined from 0 (along the positive x axis) to 2π. Often, the lorentz invariant pseudo-rapidity, η, is used instead of the polar angle. Pseudo-rapidity is defined as follows:

$$\eta = -\log[\tan(\theta/2)] \tag{3.2}$$

3.2.1 Calorimetry

Calorimeters are used to measure the energy of an incident particle. There are two types of calorimeters, electromagnetic calorimeters for measuring the energy of electrons and photons, and hadronic calorimeters for measuring the energies of particles in a jet, *e.g.* pions. In CDF, the calorimeters are segmented into projective towers in $\eta - \phi$ space, *i.e.* they point back to the nominal interaction point. There are three calorimeter sub-detectors, covering different pseudo-rapidity regions: cen-

tral (CEM,CHA) for $|\eta| < 1.1$, plug (PEM,PHA) for $1.1 < |\eta| < 2.4$, and forward (FEM,FHA) for $2.4 < |\eta| < 4.2$.

EM calorimeters

Electromagnetic(EM) calorimeters measures the energy of an incident particle that interacts electromagnetically by inducing the particle to "shower." An EM shower is a collective term given to the many electrons/photons that can result from a single energetic electron/photon that interacts electromagnetically with matter. Consider an high-energy electron that traverses a radiation length[2] in matter and gives up half its energy in the form of a bremsstrahlung photon. This photon promptly interacts via pair-production with a nucleus in the material, resulting in an energetic (although less energetic than the original incident electron) electron/positron pair which can themselves radiate photons causing the showering process to repeat. The shower continues until the energy of the bremsstrahlung photons falls below the threshold for pair-production in the material. By measuring the summed energy of the shower particles, the energy of the incident particle can be inferred. Sampling calorimeters accomplish this by constructing alternating layers of radiator (to induce the shower) and active material (to detect the shower debris).

CDF's central electromagnetic (CEM) calorimeter is a sampling calorimeter con-

---

[2]A radiation length is the distance a particle travels while its energy falls to $1/e$ of its initial value through radiative losses[17].

sisting of 30 layers of 1/8 inch thick lead (18 radiation lengths) interleaved with 5 mm thick polystyrene scintillator as the active detector medium. Shower electrons impinging on the scintillator produce blue light which is wavelength-shifted to green, then transmitted by acrylic light guides to photo-multiplier tubes (PMTs) located at the back of each wedge. A cross-sectional view of a CEM wedge is depicted in Figure 3.4. The CEM has 48 wedges each containing 10 towers. Each tower is 0.1 units of η wide by 15°, in ϕ.

The CEM was initially calibrated by exposing the center of each tower to 50 GeV test-beam electrons. This calibration was checked periodically over the course of the run using ^{137}Cs sources. The energy resolution for electromagnetic showers has been measured to be:

$$\sigma(E)/E = 13.7\%/\sqrt{E_T} \oplus 2\% \tag{3.3}$$

Approximately 6 radiation lengths into the CEM, where the electromagnetic shower maximum is expected, there is a proportional strip and wire chamber. This shower max detector, called the CES, allows precise measurements of shower position and transverse development. Anode wires provide $r - \phi$ information, while cathode strips provide z information with a resolution of 2mm in either direction for 50 GeV electrons.

Located just inside (radially) the CEM is a pre-radiator detector called the CPR, useful in distinguishing hadrons from electrons.
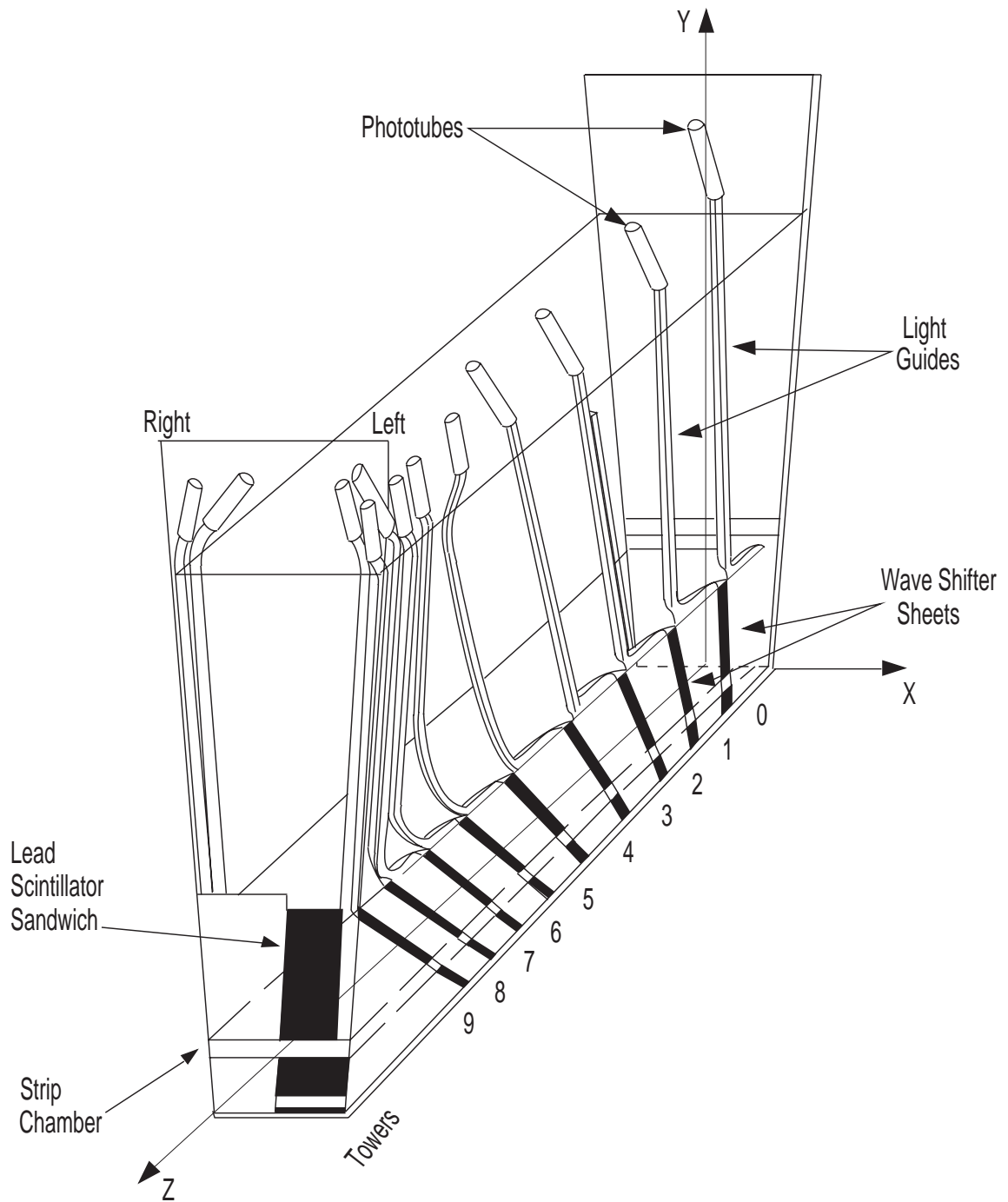
Figure 3.4: *Cross-section of a CEM wedge. From [16].*

CDF's plug electromagnetic (PEM) calorimeter is a sampling calorimeter consisting of 34 layers of 2.7 mm thick lead interleaved with proportional tube arrays as the active detector medium. Each proportional tube is filled with a 50% argon, 50% ethane mixture and contains an anode wire held at high voltage. Charged particles incident on the PEM ionize the gas mixture. The liberated electrons drift to the anode wire and by a gas avalanche process in the high field near the wire, induce a charge on the cathode (copper plated G-10 panels on one side of every proportional tube panel) proportional to the energy of the ionizing particle.

The energy resolution of the PEM has been measured with test-beam electrons to be:

$$\sigma(E)/E = 22\%/\sqrt{E} \oplus 2\% \tag{3.4}$$

CDF's forward electromagnetic (FEM) calorimeter is a sampling calorimeter consisting of 30 layers of antimony strengthened lead, 80% of a radiation length thick, interleaved with proportional tube arrays as in the PEM.

The energy resolution of the FEM has been measured with test-beam electrons to be:

$$\sigma(E)/E = 26\%/\sqrt{E} \oplus 2\% \tag{3.5}$$

HAD calorimeters

Analogous to EM calorimeters, hadronic (HAD) calorimeters measure the energy of an incident particle that undergoes nuclear interactions with matter by inducing the particle to shower hadronically. Hadronic showers are similar to electromagnetic ones except that they proceed via nuclear interactions instead of electromagnetic. Hadronic showers also take longer to develop than electromagnetic showers. As a result, HAD calorimeters must be deeper than, and placed behind, EM calorimeters.

CDF's central hadronic (CHA) calorimeter is a sampling calorimeter, situated behind the CEM, with identical segmentation in η and ϕ. It consists of 32 layers of 2.5 cm thick steel (4.7 interaction lengths) interleaved with 1 cm thick plastic scintillator as the active detector medium. Charged particles from the hadronic shower produce light in the scintillator which is collected, transmitted and amplified as in the CEM.

The CHA was initially calibrated by exposing the center of each tower to 50 GeV test-beam pions. The energy resolution for hadronic showers has been measured to be:

$$\sigma(E)/E = 50\%/\sqrt{E_T} \oplus 3\% \tag{3.6}$$

In the pseudo-rapidity region, $0.6 < |\eta| < 1.1$, particles do not pass through all the layers of the CHA. Consequently, the CHA is augmented by the end-wall hadronic calorimeter (WHA) covering the region, $0.7 < |\eta| < 1.3$. The WHA is an additional 15 layers of 5 cm steel interleaved with the same 1.0 cm thick plastic scintillator as

in the CHA.

CDF's plug hadronic (PHA) calorimeter is a sampling calorimeter consisting of 20 layers of 5.1 cm thick steel, interleaved with proportional tube arrays as the active detector medium as in the PEM.

The energy resolution of the PHA has been measured with test-beam pions to be:

$$\sigma(E)/E = 90\%/\sqrt{E} \oplus 4\% \qquad (3.7)$$

CDF's forward hadronic (FHA) is a sampling calorimeter consisting of 27 layers of 5 cm thick steel, interleaved with 2.5 cm ionization chambers as the active detector medium. The ionization chambers are rectangular cells made from aluminum on three sides, the fourth side being the copper cathode pad. The ends of the cells are plugged with molded Ryton plastic which fixes the sense wire (50 μm diameter nickel-flashed, gold-plated tungsten). The gas volume is filled with 50/50 argon/ethane as in the other calorimeters.

The energy resolution of the FHA has been measured with test-beam pions to be:

$$\sigma(E)/E = 137\%/\sqrt{E} \oplus 4\% \qquad (3.8)$$

3.2.2 Tracking

To measure the trajectory of a particle through the CDF detector, a three component tracking system is used. Closest to the interaction point is a silicon strip

detector (SVX) which provides high resolution $r - \phi$ position measurements enabling the resolution of secondary vertices. Further out in radius, there is a time projection chamber (VTX) which provides $r - z$ information to establish the primary vertex of the event. Finally, there is a drift chamber which tracks charged particles as they traverse the detector.

In addition to measuring the trajectory of particles through the detector volume, CDF uses tracking information to make precise measurements of the momenta of charged particles. This is accomplished by enclosing the tracking volume in a 1.4 Tesla magnetic field. The momentum of a charged particle is obtained from the radius of curvature of the charged track via the following relation:

$$p = qB\rho \qquad\qquad (3.9)$$

where p is the momentum, q is the charge of the particle, B is the magnetic field strength, and ρ is the radius of curvature.

Indirectly, CDF uses tracking systems to perform particle identification. Tracking chambers work by detecting the ionization of matter by energetic charged particles without respect to particle type. The amount of ionization energy deposited per unit length of matter (dE/dx), however, is strongly dependent on the particles velocity as shown in Figure 3.5. Comparison of the particle's velocity with its measured momentum gives the particles mass, which may aid in establishing its identity.

Finally, before discussing the details of the specific tracking sub-systems, I will
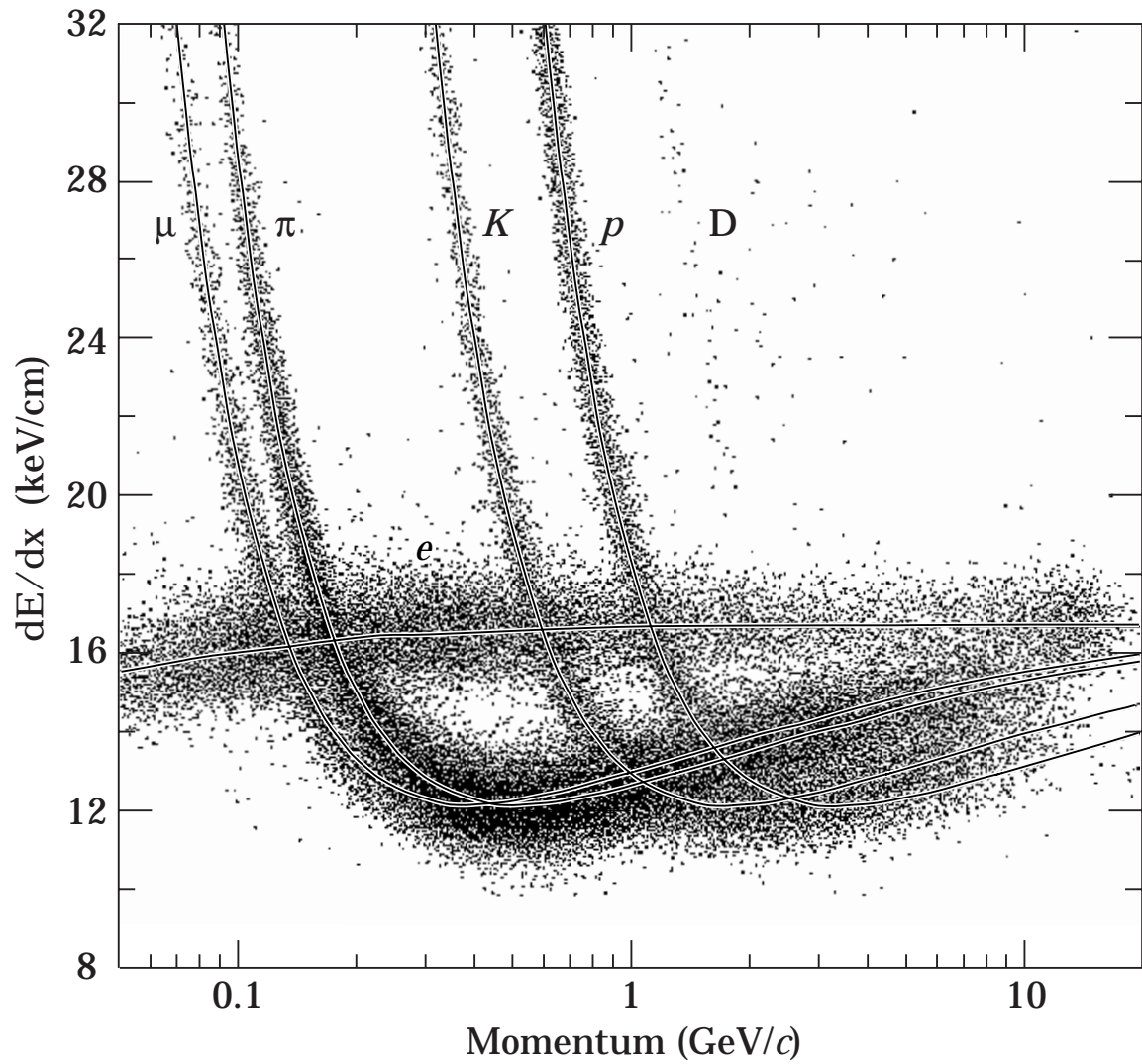
Figure 3.5: *dE/dx curves for particles with different masses showing how dE/dx can be used for particle identification. From [18].*

briefly mention the tracker-wide concern of detector material. An ideal tracking detector measures a particle's trajectory without disturbing the particles energy and momentum. In reality, however, there will be energy losses (*e.g.* ionization, radiation) and deflections (*e.g.* multiple coulomb scattering). Care must be taken to minimize these effects through material choices and thicknesses. For example, the Tevatron beam-pipe that passes through CDF is constructed out of beryllium, chosen for its low Z value[3]. In CDF, the whole tracking system, was kept to less than 5.5% of a radiation length[4].

Silicon Vertex Detector

Hadrons containing bottom quarks have a significant lifetime ($\sim 1.5ps$) and can receive large boosts (*e.g.* in top events). Thus, B-decays can, in principle, be observed as a secondary vertex in an event. B-tagging, as the process of identifying a b-quark is called, is an essential tool in many physics analyses (including this one). The reconstruction of a secondary vertex requires very precise tracking information in a region with very high track density. In this environment, a gas tracking chamber is inadequate, and a solid-state ionization detector must be utilized.

Solid-state ionization detectors offer better resolution than their gaseous counterparts because the ionization energy is substantially less in a solid than in a gas.

---

[3]The amount of multiple coulomb scattering is proportional to the charge of the atoms in the material, given by Z.

[4]$3.5\%X_0$ comes from the SVX alone.

Silicon is an ideal choice for a solid-state detector. The energy required to create an electron-hole pair in silicon is only 3.6 eV. Moreover, silicon is a semi-conductor, allowing high electric fields to be present without large DC currents generated. This is achieved by placing p-type silicon implants (strips) in an n-type silicon bulk, forming a p-n junction diode. When operated at reverse bias, a high field, sensitive region depleted of mobile charge carriers is formed. Minimum ionizing particles will liberate about 22000 electrons when traversing 300 μm of silicon. These electrons are swept to the readout electrodes by electric field set up by the bias voltage. Typical charge collection times are about 10-30 ns.

CDF used two different silicon vertex detectors over the course of Run 1 of the Tevatron: SVX in Run 1A, SVX' in Run 1B.

CDF's original Silicon Vertex Detector (SVX) consisted of two barrels on either side of $z = 0$, with a 2.15 cm gap between them. Each barrel contains four concentric layers of silicon strip detectors (ladders), divided into 12 30° wedges. The innermost layer is at a radial distance of 2.86 cm, and the outermost layer is situated at a radius of 7.87 cm. The ladders are mounted at each end onto one of two beryllium bulkheads (one for each barrel) which in addition to mechanical support, house tubes for coolant and gas flow. Each ladder is composed of three 8.5 cm long, 300 μm thick, DC-coupled, single-sided silicon crystals (n-type with p^+-type implants) with

aluminum readout strips oriented parallel to the beam-line, with a 60 μm pitch[5]. Each ladder was tilted 3° to provide overlap between adjacent wedges. The three silicon sensors in a ladder are wire-bonded end-to-end and to the readout chips mounted on an aluminum-nitride substrate hybrid circuit called the ear board. The ear board is located at the large z end of the ladder. The readout chip was a custom designed ASIC[6], called SVXD, with a feature size of 3 μm. The SVXD chip has 128 channels, each containing an analog pre-amplifier, sample-and-hold capacitors, a programmable threshold discriminator, and nearest-neighbor logic. 360 SVXD chips were required for the 46080 channels in the SVX detector. Since reading out all these channels in parallel would mean a huge readout time per event, only those channels (and their nearest neighbors) with hits (charge above programmed threshold) are read out. Even with only 5% of channels being readout, the SVX can have readout times as long as several ms. A schematic of an SVX ladder is shown in Figure 3.6. A drawing of one of the SVX barrels is shown in Figure 3.7.

Due to radiation damage[7] , SVX needed to be replaced at the conclusion of Run 1a. It was replaced with SVX', which was designed to be a radiation tolerant, but otherwise (mechanically and electrically) identical version of SVX. The chief design changes were a change from DC to AC-coupled silicon sensors and the use of the radiation hard readout chip SVXH, instead of SVXD. The tilt angle was also increased

---

[5]The outermost layer actually has a 55 μm pitch.

[6]Application Specific Integrated Circuit

[7]Signal to noise ratio had degraded from 9:1 to 6:1

PIG TAIL

READOUT EAR

MECH. ALIGNMENT
HOLE

CHIP

WIREBONDS

WIREBONDS

SILICON DETECTOR

ROHACELL AND CARBON
FIBER SUPPORT

DUMMY EAR

MECH. ALIGNMENT HOLE
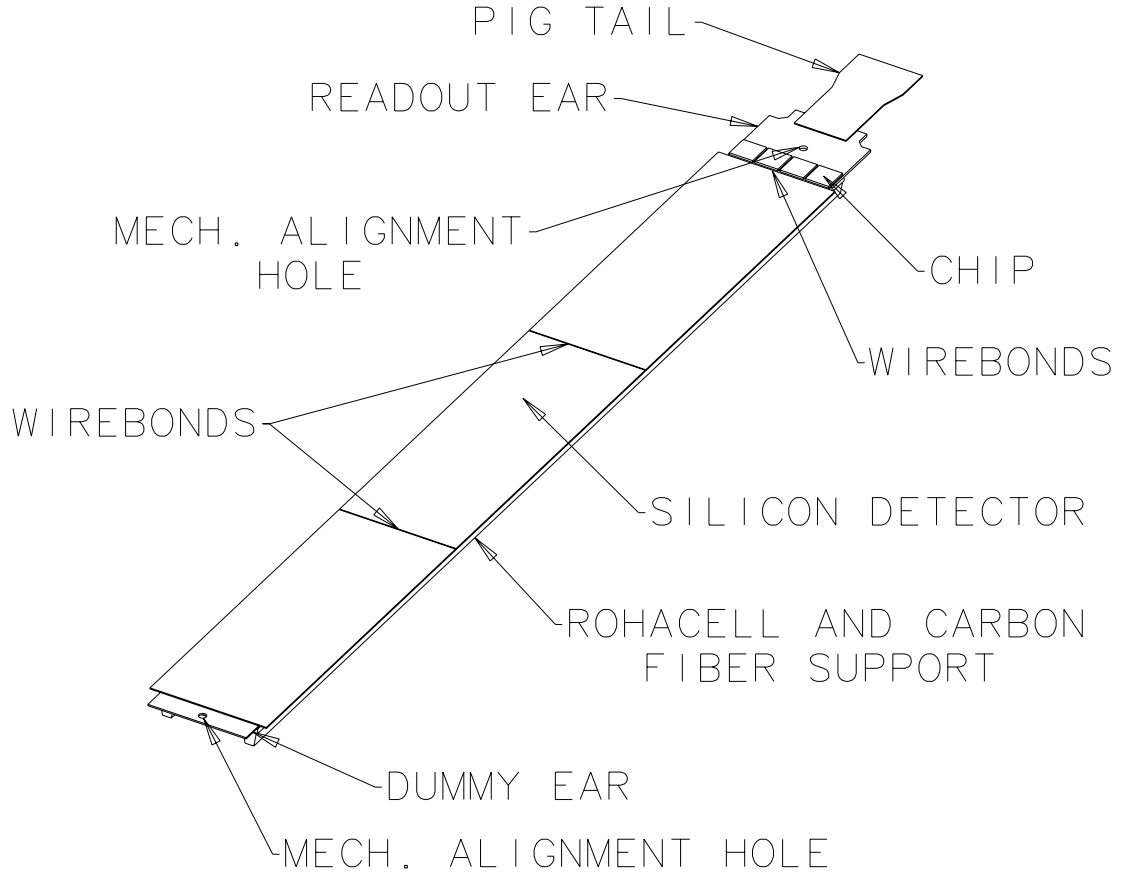
Figure 3.6: *Schematic of a Silicon Vertex Detector ladder. From [16].*

to 4.5° to provide more overlap coverage.

Vertex Tracking Chamber

As mentioned in subsection 3.1.3, the primary interaction in a proton/anti-proton collision at the Tevatron occurs at $z = 0$ with a standard deviation of $\pm 30 cm$. Moreover, due to the high luminosity of the Tevatron beam, there may be more than one interaction per crossing. CDF employs a time-projection-chamber (TPC) to determine which vertex in an event is associated with the primary interaction, and where
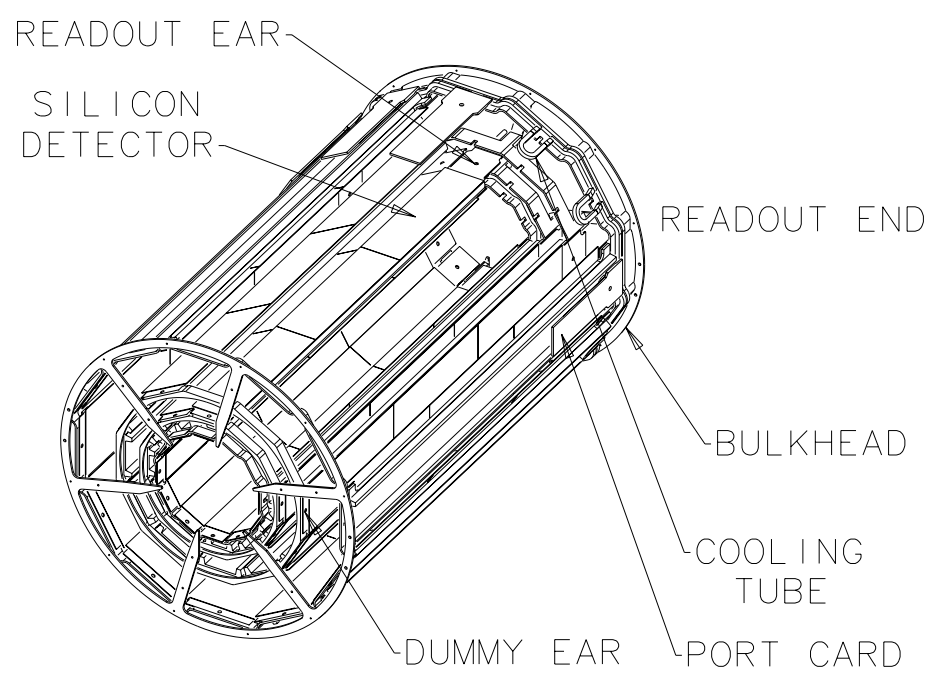
Figure 3.7: *Drawing of one of the Silicon Vertex Detector barrels. From [16].*

in z this primary vertex is located.

CDF has had two different vertex TPCs. The original, called the vertex time-projection-chamber (VTPC) was in place for Run 0 of the Tevatron, where there was no SVX. The VTPC was replaced by the VTX when SVX was installed prior to the start of Run 1.

The VTPC was composed of eight separate TPC modules. It was 2.8 m long, with an inner radius of 6.8 cm, and an outer radius of 21 cm. Each module is divided into two 15 cm long drift regions, at the end of which are proportional chambers arranged in octants. Each octant has 24 anode sense wires and 24 cathode pads. The modules are filled with a 50% Argon/50% Ethane gas mixture and an electric field of 320 V/cm is applied. Incident charged particles ionize the gas liberating electrons which drift to the sense wires with a maximum drift time of 3.5 μs. The sense wires are strung perpendicular to the radial direction. The arrival time[8] of the drift electron at these sense wire provides $r - z$ information with a z-resolution of 1 mm.

The VTX is similar in design to the VTPC, the principle modification being the VTX has space for the SVX. Additionally, the number of TPC modules was increased to 28, while the size (and corresponding maximum drift time) of each module was reduced. A cartoon of the VTX is given in Figure 3.8.

---

[8]Hence the name time-projection-chamber.
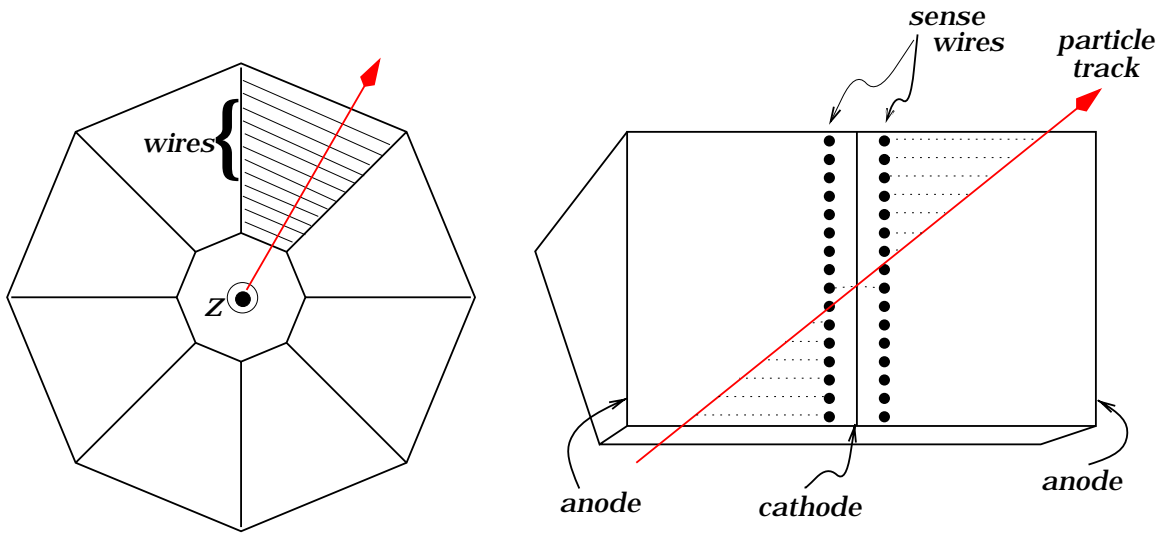
Figure 3.8: *Cartoon of the Vertex Tracking Chamber. From [16].*

Central Tracking Chamber

The heart of the CDF tracking system is the central tracking chamber (CTC). The CTC is a 3.2 m long (in the z-direction) cylindrical, open-wire, drift chamber with an inner radius of 0.3 m and an outer radius of 1.3 m. A drift chamber consists of a volume of gas in a high electric field, containing one or more sense wires. Charged particles incident upon the drift chamber ionize the gas. Ionized electrons drift to the sense wires providing spatial information with resolution better than the inter-wire spacing[9].

In CDF, there are 84 layers of sense wires made of 40 μm gold-plated tungsten, grouped into 9 "super-layers" of drift cells. Positioned about the sense wires are HV field wires which set up an electric field within the cell of 1350 V/cm, uniform to

---

[9]This requires a precise knowledge of the drift velocity of the electrons in the gas.

within 1.5%. The gas mixture used as the ionization medium is 49.6 % Argon, 49.6 % Ethane, and 0.8 % Ethanol. The maximum drift time of ionization electrons is 800 ns, much shorter than the bunch spacing. The wire planes are tilted 45° relative to the radial to account for the lorentz angle produced by the crossed electric and magnetic fields. Five of the super-layers have 12 sense wires per cell oriented along the beam line providing $r - \phi$ tracking information and are thus called axial super-layers. Interspersed between the 5 axial super-layers are 4 stereo super-layers with 6 sense wires per cell, offset from the beam-line by $\pm 3°$ (alternating each layer). The stereo super-layers provide $r - z$ tracking information. The 9 super-layers taken together provide 3-D tracking coverage over the pseudo-rapidity range, $|\eta| < 1.0$. A transverse view of the CTC end-plate is shown in Figure 3.9.

The transverse momentum resolution of the CTC is

$$\delta p_T / p_T = 0.002 GeV^{-1} \times p_T \tag{3.10}$$

This can be improved by combining the tracking information from the SVX. The transverse momentum resolution of the CTC+SVX is

$$\delta p_T / p_T = 0.001 GeV^{-1} \times p_T \tag{3.11}$$

3.2.3   Muon Systems

Muon detection is comparatively simple. Muons, since they are 100 times heavier than an electron, have a much lower bremsstrahlung cross-section; they will not
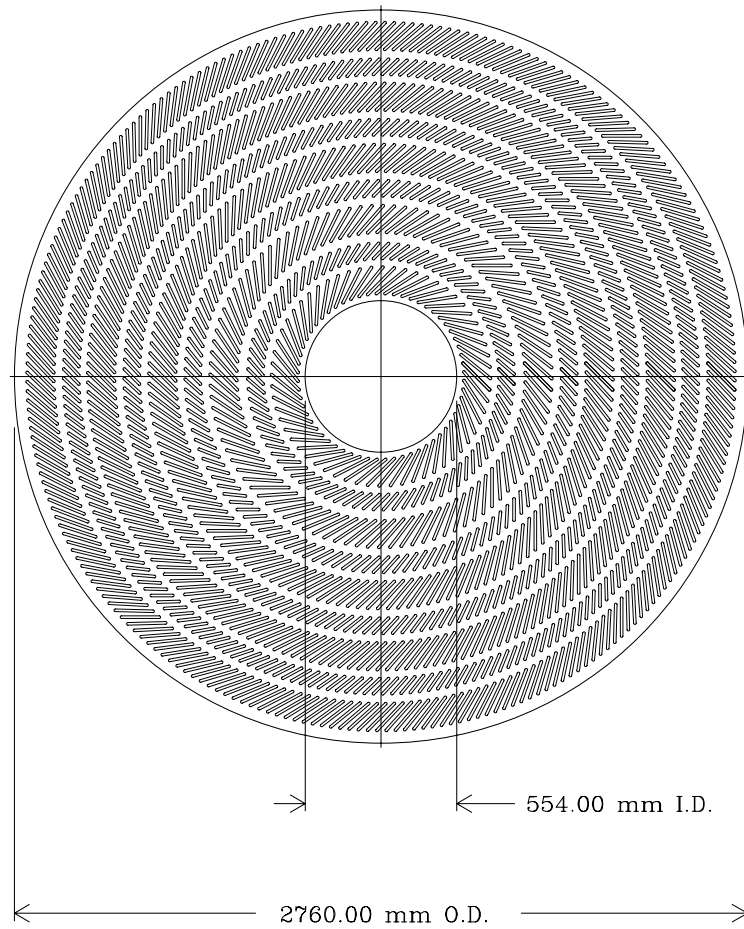
Figure 3.9: *Transverse view of the CTC end-plate. From [16].*

shower in the EM calorimeters. Muons, being leptons, only interact weakly with nuclei; they will not shower in the HAD calorimeters either. Thus, any charged particle surviving beyond the calorimeters is a muon, the detection of which is accomplished by a drift chamber.

CDF's central muon system consists of three separate muon detectors: the original Central Muon Chambers (CMU), the Central Muon Upgrade (CMP), and the Central Muon Extension (CMX). The CMP and CMX were added in 1992. The combined muon coverage by the central muon system in $\eta - \phi$ space is illustrated schematically in Figure 3.10.

Central Muon Chambers

The CMU is situated behind the CHA at a radial distance of 3.47 m from the beam-line, covering the pseudo-rapidity range $|\eta| < 0.6$. The CMU is segmented in ϕ into twelve 12.6° wedges. There are, therefore, 2.4° gaps between each module, providing only 85% coverage in ϕ. Each CMU detector is further segmented into three modules, each of which consists of four layers of four rectangular drift cells. The drift gas is 49.6 % argon, 49.6 % ethane, and 0.8 % ethanol. Sense wires are 50 μm steel and are held at 3150 V. The maximum drift time is 700 ns. The sense wires in each layer are offset from one another by a 2 mm to remove ambiguity in ϕ. The position resolution of the CMU is 250 μm in ϕ, 1.2 mm in z. Figure 3.11 is a cartoon
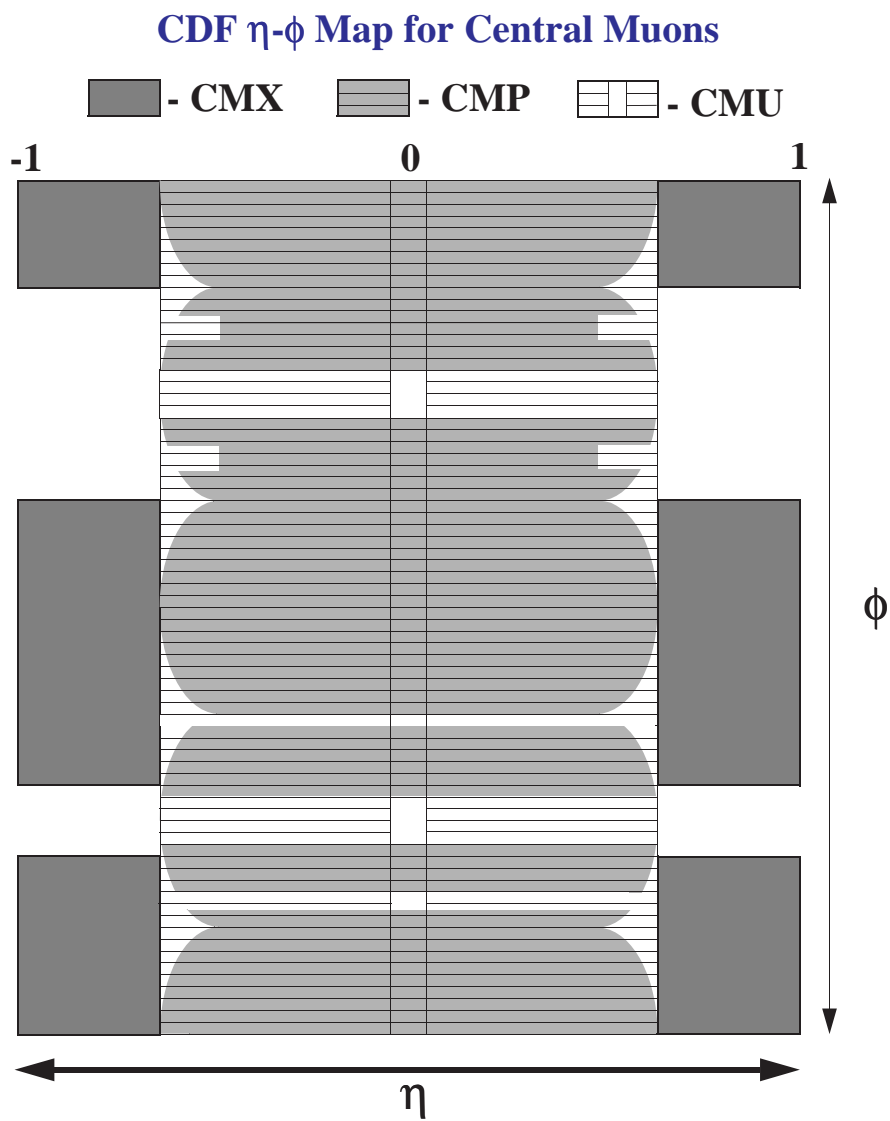
Figure 3.10: *Schematic showing central muon coverage. From [16].*
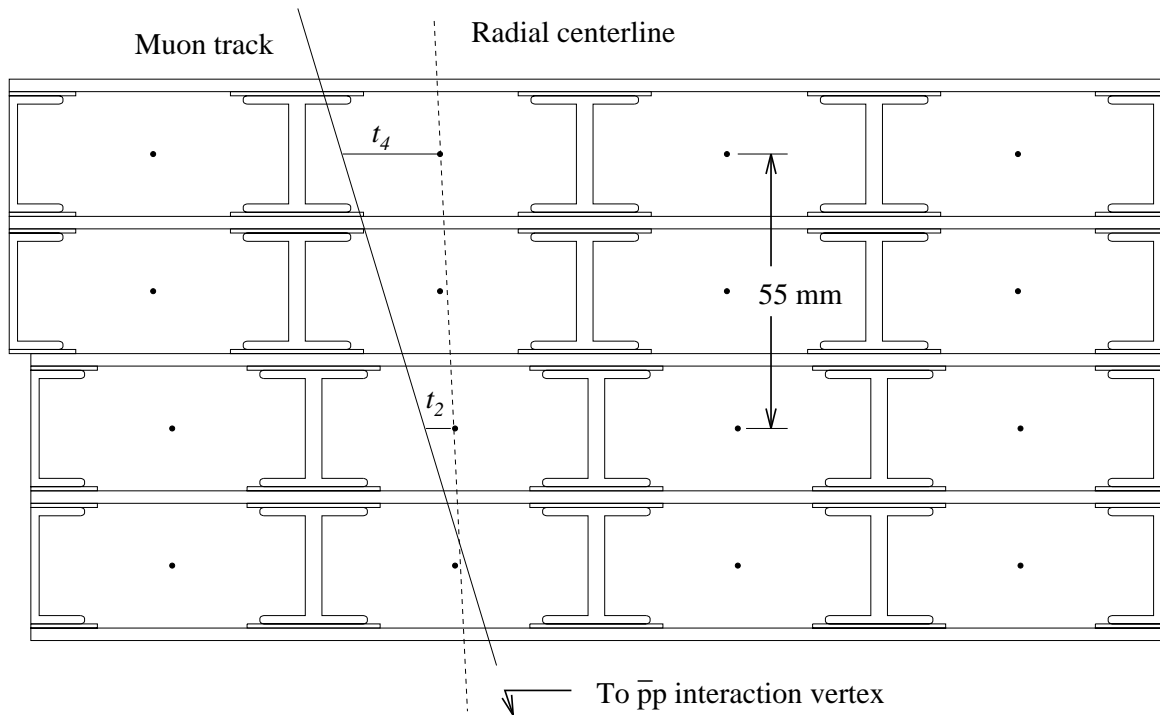
Figure 3.11: *Cartoon showing track passing through four muon chambers. Note the sense wires are offset to remove ambiguity in phi. From [16].*

showing the passing of a track through the muon chambers.

Central Muon Upgrade

During initial operation of the CDF detector, it was observed that the fake rate in the CMU due to energetic hadrons which "punch through" the calorimeters, was higher than desirable. To remedy this an additional 0.6 m (2.4 interaction lengths) of steel was added, behind which were placed four more layers of drift chambers called the CMP. The CMP also plugs the gaps in ϕ in the CMU. The inner and outer surfaces of the CMP are lined with scintillator planes, called the CSP, used to provide timing

information.

Central Muon Extension

When the CMP was added, muon coverage was also extended to the pseudo-rapidity range $0.6 < |\eta| < 1.0$ with the addition of the the CMX. The CMX consists of four free-standing conical arches of drift tubes, behind 6.2 interaction lengths of material, covering 71% of the solid-angle in the $0.6 < |\eta| < 1.0$ region. On its inner and outer surfaces, the CMX has scintillator planes, analogous to the CSP, called the CSX.

In addition to the central muon detectors, CDF has a forward muon system (FHU) covering the pseudo-rapidity range $2.0 < |\eta| < 3.6$. The FHU consists of magnetized iron toroids instrumented with drift chambers and scintillators. The FHU was not used in this analysis.

3.2.4   Luminosity Counters

CDF monitors the instantaneous luminosity delivered to it by the Tevatron via scintillators mounted on the front wall of the forward calorimeters at $z = \pm 5.8m$, called the Beam-Beam Counters (BBC). The BBC cover the pseudo-rapidity region $3.2 < |\eta| < 5.9$ with a timing resolution of 200 ps. Coincident hits in the forward and backward BBC are required. Luminosity is calculated from the number of BBC hits

divided by the effective BBC cross-section, given by [19] as:

$$\sigma_{BBC} = \frac{16\pi(\hbar c)^2}{1+\rho^2} \cdot \frac{dN_{el}/dt|_{t=0}}{N_{inel} + N_{el}} \cdot \frac{N_{BBC}^{vis}}{N_{inel} + N_{el}} \qquad (3.12)$$

where N_{BBC}^{vis} is the number of BBC triggered events. The BBC measured instantaneous luminosity is integrated over time to give total delivered luminosity. By this measure, CDF received 19.3 pb^{-1} during Run 1A, and 90.1 pb^{-1} during Run 1B.

3.2.5 Data Acquisition

With bunch crossings occurring every $3.5\mu s$, and one or more interactions per crossing, CDF sees an event rate of 280 kHz. CDF's maximum rate of data transfer to permanent storage media, however, is less than 10 Hz, meaning not every event can be recorded. To reduce the data acquisition rate to manageable levels, without loss of interesting events, CDF employs a three-level trigger system. Only events which pass level 1 (L1) trigger requirements are passed to level 2 (L2), only events which pass L2 trigger requirements are passed to level 3 (L3), and finally, only events which pass L3 trigger requirements are written to tape. Since, each successive trigger level receives fewer events than the preceding level it can use more processing time per event, *i.e.* increasingly complex detector information is utilized to make the event accept/reject decision as one moves from L1 to L3. L1 triggers typically accept events at a rate of 1 in 600, L2 1 at a rate of 1 in 100, and L3 at a rate of 1 in 4. L1 and L2 triggers are implemented in hardware while L3 triggers are implemented in software.

Level 1 Trigger

The L1 trigger uses calorimeter energy and muon chamber hits to quickly identify electrons, jets, and muon candidates. HAD and EM calorimeter towers are summed into "trigger towers" covering 0.2 units of η and 15° in ϕ. L1 Calorimeter triggers require these towers to have energy above a given threshold. L1 muon triggers require at least two hits in a given muon chamber. These requirements are maintained in hardware in a programmable "trigger table." A L1 trigger decision is available before the next bunch crossing, and as such, there is no dead-time incurred at level 1. The typical L1 acceptance rate is 1 kHz.

Level 2 Trigger

The L2 trigger builds on the calorimeter information available at L1, and adds tracking information from the central fast tracker (CFT). The CFT is a hardware processor that uses $r-\phi$ information from the axial super-layers of the CTC to crudely reconstruct high-momentum tracks. CFT tracking begins with hits in the outermost super-layer, matching them to hits on inner layers, and forming track candidates. The CFT requires 14 (out of 15) CTC hits to pass a track candidate. The transverse momentum resolution of the CFT is $\delta p_T/p_T^2 = 3.5\%$. At L2, calorimeter clusters are formed by summing the deposited energy from neighboring towers around a seed tower above a certain threshold. This is done separately for EM and HAD towers.

Kinematic variables are calculated for each cluster (E_T, η, ϕ). Jets are identified and missing E_T calculated. Tracks found by the CFT are matched to EM clusters to form electron candidates (if no matching tracks are found, photon candidates are formed) and to muon chamber hits to form muon candidates. The trigger decision is then a selection on these physics objects alone or in combination as specified in the trigger table. A L2 trigger decision takes 20 μs. Bunch crossings which occur during this time are ignored by the detector. The resultant dead-time is a few percent. The typical L2 acceptance rate is 20-35 Hz.

Level 3 Trigger

The L3 trigger consists of `FORTRAN-77` filter algorithms running on a farm of Silicon Graphics processors for the last stage of online data reduction. L3 reconstructs events using a simplified version of the off-line analysis code, and groups them into datasets needed for various physics analyses. Events which pass the L3 trigger are written to 8 mm tape for off-line analysis. The typical L3 acceptance rate for Run 1A was 3-5 Hz, and 8 Hz for Run 1B.

Chapter 4

Data Selection

In section 2.2.2 the decay modes of the top quark were described. This thesis is a measurement of gluon radiation in top events. While this measurement technique could in principle be applied to all decay modes of the top, the lepton[1] + jets mode $(t\bar{t} \rightarrow bWbW \rightarrow bb\ell\nu jj)$ yields a clean, reasonably large dataset with well-understood backgrounds, and as such is the most appropriate channel on which to develop this technique. This analysis, therefore, restricts itself to the lepton + jets mode. The leptonic W is identified in the CDF detector as an isolated, high p_T lepton, with large missing energy. To reduce the background from W+jets, two or more high E_T jets are required, one of which must be tagged as a b with a displaced vertex reconstructed by the SVX. These selection criteria are described in detail in the following sections.

This thesis used 106.0 ± 4.1 pb^{-1} of data collected by CDF during Run1A and Run1B of the Tevatron [20].

4.1   Triggers

The creation of the top lepton + jets event sample begins with the high-p_T inclusive central lepton datasets: ICE1A1(ICMU1A1) for electrons(muons) from Run 1A and EIA(MUA) for electrons(muons) from Run 1B. These datasets are composed of events which passed the L3 triggers listed in Table 4.1. These triggers require a crudely identified central electron(muon) in the CEM(CMU/CMX/CMP) with a

---

[1]lepton here means e or μ

Run	Dataset	Lepton	Level 3 Triggers	Number of Events
Run 1A	ICE1A1	e	COMBINED_ELE2_CEM	133,805
Run 1A	IMU1A1	μ	COMBINED_MUO2_CMU	83,051
Run 1B	EIA	e	ELEA_CEM_18	128,761
			ELEA_CEM_50	
Run 1B	MUA	μ	MUOA_CMU_18	90,908
			MUOA_CMX_18	
			MUOA_CMP_18	
			MUOA_CMX_18	
			MUOA_CMU_AND_CMP_18	
			MUOA_CMU_ETA_GAP	

Table 4.1: *Run 1 High p_T inclusive central lepton samples. The disproportionately large samples from Run 1A are due to differences in the triggers.*

$p_T > 18$ GeV.

Off-line selection criteria ("cuts") are applied to the high-p_T inclusive central lepton datasets[21]. These cuts eliminate fake events, refine the L3 lepton identification, and reject background. They are detailed in the following sections.

4.2   Event Criteria

Events from a known bad run (*e.g.* one or more detector sub-systems malfunction-ing) are rejected. Events are required to have passed L2 with an appropriate trigger given the primary lepton in the event. A list of L2 triggers allowed for Run 1A and Run 1B is given in Appendix B. The primary vertex of the event, as measured by the VTX, is required to be near the nominal interaction point. A $|Z_v| < 60$ cm cut is applied.

4.3   Electron Identification

In order to remove fake-electrons, and real electrons that do not originate from the primary interaction, from the electron candidates identified at L3, several standard cuts are made. The E_T requirement on the CEM cluster is raised to 20 GeV. The ratio of the calorimeter energy to the magnitude of the measured track momentum (E/p) is compared. Electrons are essentially massless, so this ratio should be equal to 1. E/p is required to be less than 1.8. As explained in section 3.2.1, electron showers should be contained in the EM calorimeter, with very little energy deposition in the HAD calorimeter. Thus, the ratio of calorimeter energies (HAD/EM) is required to be less than 5%. Also recall from section 3.2.1 that the CEM was calibrated with test-beam electrons. Real electrons in the experiment should have a lateral shower

profile consistent with that of the test-beam electrons. The variable L_{SHR} is defined to quantify this comparison.

$$L_{SHR} = 0.14 \sum_i \frac{E_i^{obs} - E_i^{pred}}{\sqrt{(0.14\sqrt{E})^2 + \sigma_{pred}^2}} \tag{4.1}$$

where the sum is over adjacent towers, E_i^{obs} is the energy observed in tower i, E_i^{pred} is the energy predicted from test-beam data in tower i, $0.14\sqrt{E}$ is the uncertainty on the measured energy, and σ_{pred}^2 the uncertainty on the predicted energy. A cut is made at $L_{SHR} < 0.2$. The electron track in the CTC extrapolated to the CES is required to be well matched to hits in the CES. The cuts imposed are $|\Delta x| < 1.5$ cm and $|\Delta z| < 3.0$ cm. The CES was also calibrated with test-beam electrons, and electron candidates in the data are required to match the shower shape of the test-beam data. This requirement is enforced via a χ^2 test between the predicted and measured shower shapes, with the cut $\chi^2 < 10$. The electron is required to come from the primary interaction by comparing the z of the electron track projected back to $r = 0$ with the z of the primary vertex as measured by the VTX. The difference $|Z_v - Z_0^e|$ is forced to be less than 5.0 cm. Detector fiducial cuts are applied to reject electron candidates which passed near parts of the detector that are not well instrumented due to holes, gaps, etc.

Finally, conversion electrons are removed from the data sample. Conversion electrons are electrons that are pair-produced from photon interactions with detector material. Prior to conversion removal, the high-p_T inclusive central electron sample is

approximately 30-40% conversions[22]. Conversion electron candidates are identified by searching for an oppositely charged track in the vicinity of the electron candidate with a point of closest approach in a material laden detector region ($-20 < R_{conv} < 50$ cm). Since electron/positron conversion pair originate from a common point, the azimuthal(polar) angle separation of the two tracks at their point of tangency is required to be small. Conversions are removed by cutting on $|\Delta(r - \phi)| < 0.3$ cm, and $|\Delta \cot \theta| < 0.06$ for any conversion electron candidates. Finally, to remove conversions where no additional track is found, electron candidates in events with VTX occupancy less than 20% of the expected rate are removed. These cuts remove $\sim 99\%$ of conversion electrons from the dataset.

The electron id cuts used are summarized in Table 4.2.

4.4   Muon Identification

In order to remove fake-muons, and real muons produced by cosmic rays, from the muon candidates identified at L3, several standard cuts are made. The muon p_T, as measured by the CTC, is required to be at least 20 GeV. Muons are charged particles, and while they will not shower in the EM or HAD calorimeters (see section 3.2.3), they will deposit small amounts of ionization energy in them. The energy deposited in the EM calorimeters is required to be less than 2.0 GeV. The energy deposited in the HAD calorimeters is required to be less than 6.0 GeV. To reject muons from cosmic

$E_T > 20$ GeV

$E/p < 1.8$

$\frac{HAD}{EM}(3 \times 3) < 0.05$

L_{SHR}(3-Tower)< 0.2

$|\Delta x| < 1.5$ cm

$|\Delta z| < 3.0$ cm

$\chi_s^2 < 10$

$|Z_v - Z_0^e| < 5.0$ cm

Fiducial cuts

Conversion removal

Table 4.2: *Electron identification cuts.*

$$p_T > 20 \text{ GeV (beam constrained)}$$

$$E_{EM} \text{ (muon tower)} < 2.0 \text{ GeV}$$

$$E_{HAD} \text{ (muon tower)} < 6.0 \text{ GeV}$$

$$D_0 < 0.3 \text{ cm}$$

$$|Z_v - Z_0^\mu| < 5.0 \text{ cm}$$

$$\text{CMU:} |\Delta x| < 2.0 \text{ cm}$$

$$\text{CMP,CMX:} |\Delta x| < 5.0 \text{ cm}$$

Table 4.3: *Muon identification cuts.*

rays, the muon is required to originate from near the nominal interaction point. A cut is made on the impact parameter of the muon track, $D_0 < 0.3$ cm. The muon is required to come from the primary interaction by comparing the z of the muon track projected back to $r = 0$ with the z of the primary vertex as measured by the VTX. The difference $|Z_v - Z_0^\mu|$ is forced to be less than 5.0 cm. The muon track in the CTC extrapolated to the muon chambers is required to be well matched. For CMU muons the cut imposed is $|\Delta x| < 2.0$ cm. CMP and CMX muons have gone through more material, and consequently undergone more multiple coulomb scattering. For this reason, the track matching cut for CMP,CMX muons is loosened to $|\Delta x| < 5.0$ cm.

The muon id cuts used are summarized in Table 4.3.

4.5 W Selection

Having identified a high-p_T lepton, the next step in selecting the top lepton+jets dataset is the requirement of a leptonic W. A leptonic W decays via $W \to \ell\nu$. Since neutrinos do not interact in the detector, they are not directly observable, but must be identified by missing energy. Thus, a leptonic W is identified in CDF by the presence of an isolated lepton together with missing E_T. Isolation of the lepton means that there is no energy in the calorimeter towers surrounding the tower to which the lepton track points. This isolation is quantified by the following relation for electrons:

$$ISO^e = \frac{E_T^{cone} - E_T^e}{E_T^e} \tag{4.2}$$

where E_T^{cone} is the sum E_T contained within a cone of radius $\Delta R = 0.4$ around the electron cluster charge centroid in the CEM, and E_T^e is the calorimeter energy of the electron, and $\Delta R \equiv \sqrt{\Delta\phi^2 + \Delta\eta^2}$.

Isolation for muons is similarly defined as:

$$ISO^\mu = \frac{E_T^{cone} - E_T^\mu}{p_T^\mu} \tag{4.3}$$

where E_T^{cone} is the sum E_T contained within a cone of radius $\Delta R = 0.4$ around the muon track, and E_T^μ is the calorimeter energy of the tower pointed to by the muon track, and p_T^μ is the transverse momentum of the muon track.

The isolation cut on the primary lepton is $ISO < 0.1$. In an interaction, the transverse energy must be conserved, i.e. $\sum E_T = 0$. Missing transverse energy ($\not{E}_T$)

$$ISO^\ell < 0.1$$

$$\displaystyle{\not{E}_T} > 20 \text{ GeV (muon corrected)}$$

Table 4.4: *W selection cuts.*

is, therefore, defined as the energy needed to balance the observed E_T, making the sum zero. Missing energy calculated in this way, is equal to minus the vector sum of transverse energy in the calorimeters (clustered and unclustered), corrected for muons which do not deposit most of their energy in the calorimeters, or written symbolically:

$$\not{E}_T = -(\sum \vec{E}_T^{clus} + \vec{E}_T^{unclus} - \vec{E}_T^{\mu} + \vec{p}_T^{\mu}). \tag{4.4}$$

where $E_T^{clus}(E_T^{unclus})$ is the clustered(unclustered) calorimeter energy, E_T^{μ} is the calorimeter energy of the tower pointed to by the muon track, and p_T^{μ} is the transverse momentum of the muon track. Events are required to have $\not{E}_T > 20$ GeV.

The W selection cuts used are summarized in Table 4.4.

4.6 Z removal

Events where the primary lepton is a decay product of a Z boson $(Z \rightarrow \ell^+\ell^-)$ are removed. This is accomplished by identifying secondary leptons and reconstructing the dilepton invariant mass. Primary leptons with a secondary lepton passing the cuts listed in Table 4.5 are considered Z-candidates. If the dilepton invariant mass of the

Secondary lepton	Cuts
Electrons	$E_T > 10$ GeV
	$E/P < 2.0$
	$\frac{HAD}{EM} < 0.12$
	$ISO < 0.1$
Muons	$p_T > 15$ GeV
	$|\eta| < 1.1$
	$|\Delta x| < 5.0 cm$

Table 4.5: *Secondary lepton identification cuts for Z removal.*

Z-candidate pair is within a window around the Z mass (75 GeV $< M_{\ell\ell} < 105$GeV), the event is discarded[2].

4.7 Dilepton Removal

Non-Z dilepton events are also removed. These events include cosmic-ray fakes as well as dilepton top events ($t\bar{t} \rightarrow bWbW \rightarrow bb\ell\nu\ell\nu$). An event is considered a dilepton candidate event if an additional oppositely charged (with respect to the primary) lepton is identified with $E_T > 20$ GeV. If the dilepton candidates have an event topology consistent with that of a cosmic-ray (*e.g.* back-to-back), the event is rejected.

---

[2]The Z mass is 91.187 GeV[18].

$$\Delta\phi > 178.5° \text{ AND } \sum\eta < 0.1$$

$$\text{- OR -}$$

$$t_1^\ell, t_2^\ell > 18(22) \text{ ps}$$

$$t_1^\ell, t_2^\ell < -14 \text{ ps}$$

$$\Delta t > 14 \text{ ps}$$

$$\Delta\phi > 177.0° \text{ AND } \sum\eta < 0.25$$

Table 4.6: *Cosmic-ray identification cuts.*

The cosmic-ray id cuts used are summarized in Table 4.6. If the candidate event contains $\not{E}_T > 25$ GeV and exactly two jets with $E_T > 15$ GeV each, it is considered a top dilepton event and is removed. Additionally, if an isolated ($\sum p_T < 2.0$ GeV in a cone of radius 0.4) oppositely charged track with $p_T > 15$ GeV is present, the event is discarded.

4.8   Top Selection

Lepton + jet top events are selected from the W sample by requiring two or more jets with uncorrected $E_T > 15$ GeV, at least one of which has been b-tagged.

4.8.1 Jets

Quarks or gluons produced in an interaction fragment into a collimated spray of particles which deposit energy in several towers of the calorimeters. Since the desired kinematic quantity is the energy of the pre-fragmentation parton, the energy of these several towers must be summed. A jet clustering algorithm is employed to make this summation. The algorithm chosen, optimized to identify jets in top events, is summarized below:

1. Seed towers with $E_T > 3$ GeV are identified.

2. Clusters are formed from the seed tower plus (contiguous) neighboring towers with $E_T > 1$ GeV.

3. An energy-weighted centroid of the cluster is computed.

4. A jet is defined with energy equal to the sum of energy contained in a cone of radius $\Delta R = 0.4$ about the centroid.

The energy of a jet, so defined, is called "raw" or "uncorrected," meaning the calorimeter energy has not been corrected for either detector effects (*e.g.* cracks in the calorimeter) or physics effects (*e.g.* neutrinos in the jet). As mentioned above, to improve the signal-to-background ratio, events selected in this analysis are required to have at least two jets with uncorrected $E_T > 15$ GeV.

4.8.2   B-tagging

CDF uses 3 techniques to tag b-quarks. The first technique (`SECVTX`) uses the SVX to reconstruct a secondary vertex in a jet, displaced from the primary due to the long lifetime of the bottom quark, to identify the jet as having come from a b quark. The second technique, called a soft-lepton-tag (`SLT`) uses the presence of a lepton in a jet, resulting from a semi-leptonic B-decay, to b-tag the jet. The third technique called a jet probability (`JTPRB`) tag, assigns a probability to a jet for originating from a light quark (uds), based on the impact parameter of the tracks in the jet. Jets coming from b-quarks have near zero `JTPRB` and can be identified in this way. Of these three techniques, the `SECVTX` tag has the highest purity (lowest fake rate) and is the technique employed in this analysis. More detail on the `SECVTX` b-tag algorithm is given in the following section.

Secondary Vertex Tag

Bottom quarks from a decayed top quark travel several millimeters (3.4 on average) before they themselves decay, forming a vertex that is displaced from the primary vertex by an amount which may be measurable by the SVX. Such a vertex is called a secondary vertex and is shown in a schematic drawing in Figure 4.1. The algorithm employed to identify secondary vertices at CDF is called `SECVTX`. The `SECVTX` algorithm looks for two or more displaced tracks within a jet that form a vertex. Tracks

are considered within a jet if the opening angle between the track and the jet axis is less than 35°. Only jets with $E_T > 15$ GeV and $|\eta| < 2.0$ are considered. Displaced tracks are tracks in the SVX with an impact parameter[3] which is large compared to its uncertainty (computed as the ratio of these quantities and termed the significance of detachment). The SECVTX algorithm searches for secondary vertices in two passes. The first pass makes loose track quality and significance of detachment cuts and searches for a vertex containing three or more tracks. If that fails, tighter track quality and significance of detachment cuts are made and a search for a vertex containing two or more tracks is made. For secondary vertices identified by either pass 1 or pass 2, the distance in the transverse plane from the secondary to primary vertex is calculated. This quantity is called L_{xy} and is defined to be positive if the vertex is on the same side of the primary as the jet. A jet with an identified vertex with a positive L_{xy} that is large compared to its uncertainty is considered tagged. Vertices with negative L_{xy} are dominantly mistagged light quark jets. Table 4.7 lists in detail the cuts used in the SECVTX algorithm.

4.8.3 Event Count

Table 4.8 contains the number of events after selection cuts as a function of jet multiplicity along with a comparison to other relevant top analyses. A detailed list

---

[3]Impact parameter is defined as the distance of closest approach from a track to the interaction point.

Stage	N_{hits}^{SVX}	SVX Track Cuts
Pass 1 at finding vertex	2	$p_T > 1.5$ GeV
	≥ 3	$p_T > 0.5$ GeV
	≥ 2	$\frac{D_0}{\sigma_{D_0}} > 2.5$
	≥ 2	$\chi^2/d.o.f. < 6$
	≥ 2	≥ 3 tracks form a vertex, ≥ 1 w/ $p_T > 2.0$ GeV
Pass 2 at finding vertex	≥ 3	$p_T > 1.0$ GeV
	≥ 3	$\frac{D_0}{\sigma_{D_0}} > 3.0$
	≥ 3	≥ 2 tracks form a vertex, ≥ 1 w/ $p_T > 2.0$ GeV
Vertex found	-	$L_{xy} < 2.0$ cm
	-	$\frac{|L_{xy}|}{\sigma_{L_{xy}}} > 3.0$
	-	$L_{xy} > 0.0$
	-	$c\tau_{xy}^{sec} < 1.0$ cm

Table 4.7: *Cuts used in* **SECVTX** *algorithm.*
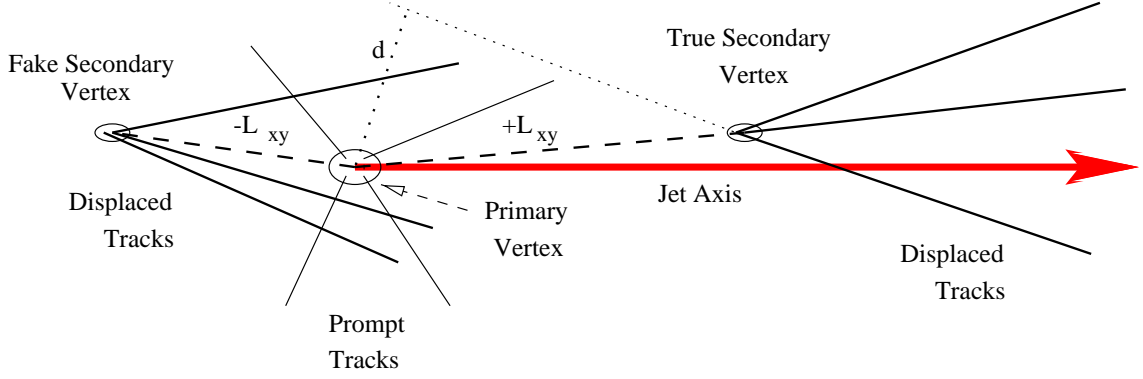
Figure 4.1: *Schematic drawing of secondary vertex resulting from b-decay.*

$W + 1j$	$W + 2j$	$W + 3j$	$W + \geq 4j$
67	40	16	14

Table 4.8: *Number of events passing selection cuts as a function of jet multiplicity (uncorrected $E_T > 15$ GeV).*

of the events passing all cuts can be found in Appendix A.

4.9   Backgrounds

The events passing the lepton + jets top selection cuts described above are not all top events. These remaining non-top events, *i.e* irreducible background, come from several sources. The dominant backgrounds can be collectively called $W +$ jets. The largest single background process is direct Wg production where the gluon splits to a heavy flavor quark which is tagged ($g \to b\bar{b}(c\bar{c})$). $W +$ heavy flavor also contributes to the background via the reaction $qs \to Wc$, where the strange quark

has come from the sea of the proton/anti-proton. After W plus heavy flavor, the next largest background source is from W + a light quark jet which is mistagged by SECVTX. Small background contributions also arise from other sources including diboson, non-W, and single top processes.

Background rates are calculated separately for each process[23]. The mistag rate is directly calculable from the data. A $-L_{xy}$ tag rate is derived form a generic jet sample. After correction for the fact that a small percentage of vertices with negative L_{xy} will actually have come from heavy flavor jets, this mistag rate is parametrized as a function of E_T, η, and the number of tracks in the jet. This parameterization is applied to the top lepton + jet dataset and the mistag background contribution estimated. Background rates for $Wb\bar{b}, Wc\bar{c}$ are calculated separately for the fraction of events with exactly one $b(c)$-jet in the final state and the fraction of events with exactly two $b(c)$-jets in the final state. For the one $b(c)$-jet case, the HERWIG general purpose parton-shower Monte Carlo program[24] is used while for the two $b(c)$-jet case the matrix element Monte Carlo program VECBOS[25] is used followed by HERPRT for fragmentation. Background rates for Wc are also estimated with HERWIG. Background rates for diboson, non-W, and single top are estimated with the PYTHIA general purpose parton shower Monte Carlo program[26]. The response of the CDF detector is simulated, with the exception of the b-tagging efficiency of the SVX, with a parametrized Monte Carlo tuned to electron and pion test-beam data called QFL.

Source	$W + 1j$	$W + 2j$	$W + 3j$	$W+ \geq 4j$
Mistags	18 ± 7	6.3 ± 2.6	1.6 ± 0.6	0.67 ± 0.26
$W/Z + b\bar{b}(c\bar{c})$	19.5 ± 7.5	9.7 ± 2.8	1.9 ± 0.6	0.26 ± 0.09
Wc	17 ± 6	4.3 ± 1.5	0.6 ± 0.2	0.06 ± 0.02
Diboson + Non-W	10 ± 4	3.7 ± 1.1	1.1 ± 0.4	0.65 ± 0.3
Single top	1.2 ± 0.4	2.5 ± 0.8	0.8 ± 0.4	0.2 ± 0.1
Total	65.7 ± 12.5	26.5 ± 4.3	6.0 ± 1.0	1.84 ± 0.4

Table 4.9: *Estimated background after selection as a function of jet multiplicity (uncorrected $E_T > 15$ GeV). From [27].*

A first-principles based Monte Carlo simulation, CDFSIM was used to calculate the b-tagging efficiency of the SVX. The computed background estimates are tabulated in Table 4.9.

Chapter 5

Data Analysis

5.1 Method

This analysis attempts to parse the top events collected by CDF in Run 1A+1B, and used in the measurement of the *inclusive $t\bar{t}$* production cross section, into fractions which contain zero, one, or possibly two jets with corrected E_T greater than a given threshold (see section 4.8.1) with the goal of converting these fractions into $t\bar{t} + \text{jet(s)}$ cross-section ratios, relative to the inclusive rate. These fractions will be denoted $f_{t\bar{t}}, f_{t\bar{t}j}, f_{t\bar{t}jj}$ where j can be a quark, but is dominantly a gluon at the Tevatron. In the Run 1 dataset it is expected that the $t\bar{t}jj$ contribution will be small, and that higher order terms may be neglected[28][29].

The presence of gluon radiation in a top (or any other) event is distinguished primarily[1] by the jet multiplicity of that event. It is important to note, however, that it is not necessarily the presence of an *extra* jet that indicates a gluonic top event. This is because not all partons in a top event (gluonic or not) are reconstructed as jets due to geometric acceptance of the calorimeter and/or merging of partons within the cone employed in the jet clustering algorithm. An ensemble of $t\bar{t}$ events, therefore, will have a jet multiplicity distribution, $N_{jet}^{t\bar{t}}$, which in general will have a distinct shape from the jet multiplicity distribution $N_{jet}^{t\bar{t}j}$ obtained from an ensemble of $t\bar{t}j$ events. $N_{jet}^{t\bar{t}jj}$ will be similarly distinguishable. Thus, if one can accurately model the topology of $t\bar{t} + \text{jets}$ events in the CDF detector (see section 5.2.1) and generate the-

---

[1]there are others like jet width - see CDF 3895

oretically expected jet multiplicity distributions (templates), the $f_{t\bar{t}}, f_{t\bar{t}j}, f_{t\bar{t}jj}$ can be determined from a shape comparison of the jet multiplicity of the data to these templates[2] $N_{jet}^{t\bar{t}}, N_{jet}^{t\bar{t}j}, N_{jet}^{t\bar{t}jj}$. A binned likelihood fit is employed to make this comparison. This analysis strategy is summarized below:

- Assume $t\bar{t}X = t\bar{t} + t\bar{t}j + t\bar{t}jj + \ldots$

- Model $t\bar{t}, t\bar{t}j, t\bar{t}jj$ where j is a jet with corrected $E_T > E_T^{thresh}$

- Exploit distinct shapes of jet multiplicity distributions, $N_{jet}^{t\bar{t}}, N_{jet}^{t\bar{t}j}, N_{jet}^{t\bar{t}jj}$ to parse inclusive dataset with a binned likelihood fit.

- Extract cross-section ratio, for $t\bar{t}j/t\bar{t}X$

5.1.1   Binned Likelihood Fit

The general form of a binned likelihood function for poisson distributed data in N bins is given by

$$\mathcal{L}_{Poisson} = \prod_{i=1}^{N} \frac{\mu_i^{n_i} e^{-\mu_i}}{n_i!} \tag{5.1}$$

where n_i is the observed events in bin i and μ_i is the expected number of events in bin i. In order to re-write the above in terms of the signal and background fractions make the replacement

$$\mu_i = n_{tot}^{data} \left(f_{t\bar{t}} \varepsilon_i^{t\bar{t}} + f_{t\bar{t}j} \varepsilon_i^{t\bar{t}j} + f_{t\bar{t}jj} \varepsilon_i^{t\bar{t}jj} + f_{bkgnd} \varepsilon_i^{bkgnd} \right) \tag{5.2}$$

[2]Note it is the shape of the theoretical distributions that are being utilized NOT the normalization

where the f's are the signal and background fractions to be fitted for, and the ε_i are the expected fraction of events with jet multiplicity i obtained from normalized template distributions $N_{jet}^{t\bar{t}}, N_{jet}^{t\bar{t}j}, N_{jet}^{t\bar{t}jj}, N_{jet}^{bkgnd}$ generated from the Monte Carlo described in sub-section 5.2.1.

The background is not, however, a complete unknown, as it has been estimated previously in the various CDF top cross section measurements. To incorporate an independent calculation of the background fraction and its associated uncertainty the following term is added to the likelihood function

$$\mathcal{L}_{Gaussian} = \frac{1}{\sqrt{2\pi}\sigma_{bkgnd}} e^{-\frac{1}{2}(n_{tot}^{data} f_{bkgnd} - \mu_{bkgnd})^2 / \sigma_{bkgnd}^2} \tag{5.3}$$

The combined likelihood is then

$$\mathcal{L} = \mathcal{L}_{Gaussian} \times \mathcal{L}_{Poisson} \tag{5.4}$$

Written explicitly, the final form of the likelihood function is

$$\mathcal{L} = \frac{1}{\sqrt{2\pi}\sigma_{bkgnd}} e^{-\frac{1}{2}(n_{tot}^{data} f_{bkgnd} - \mu_{bkgnd})^2 / \sigma_{bkgnd}^2} \tag{5.5}$$

$$\times \prod_{i=1}^{N} \frac{n_{tot}^{data}(f_{t\bar{t}}\varepsilon_i^{t\bar{t}} + f_{t\bar{t}j}\varepsilon_i^{t\bar{t}j} + f_{t\bar{t}jj}\varepsilon_i^{t\bar{t}jj} + f_{bkgnd}\varepsilon_i^{bkgnd})^{n_i^{data}} e^{-n_{tot}^{data}(f_{t\bar{t}}\varepsilon_i^{t\bar{t}} + f_{t\bar{t}j}\varepsilon_i^{t\bar{t}j} + f_{t\bar{t}jj}\varepsilon_i^{t\bar{t}jj} + f_{bkgnd}\varepsilon_i^{bkgnd})}}{n_i^{data}!}$$

The signal and background fractions sought are those that maximize this likelihood. This is equivalent to minimizing $-\log\mathcal{L}$, which is accomplished using the minimization package MINUIT[30]. The fractions $f_{t\bar{t}}$, $f_{t\bar{t}j}$, f_{bkgnd} are the free parameters of the fit. The $t\bar{t}jj$ fraction is included in the likelihood function since it may not be negligible,

but is not fitted for directly. Instead, it is constrained[3] by the assumption:

$$\frac{N_{t\bar{t}j}}{N_{t\bar{t}}} \approx \frac{N_{t\bar{t}jj}}{N_{t\bar{t}j}} \tag{5.6}$$

where $N_{t\bar{t}(j)(j)} = f_{t\bar{t}(j)(j)} \times n_{tot}^{data}$.

5.2 Jet Multiplicity Distributions

Recall that the likelihood fit described in sub-section 5.1.1 makes a shape comparison of jet multiplicity distributions $N_{jet}^{t\bar{t}}, N_{jet}^{t\bar{t}j}, N_{jet}^{t\bar{t}jj}, N_{jet}^{bkgnd}$ to the data. The generation of these distributions is described in what follows.

5.2.1 Matrix Elements

The currently available Monte Carlo event generators do not handle gluon radiation in top events very well. This is because they do not incorporate explicit matrix element (ME) calculations for gluonic final states (*e.g.* $q\bar{q} \rightarrow t\bar{t}g$) but rather employ a parton-shower (PS) algorithm to radiate gluons off the $t\bar{t}$ pair. While the PS approach is adequate for the modeling of soft gluons, collinear with their originating quarks, it underestimates the rate of hard, well-separated gluon radiation[31]. Although the PS Monte Carlo generators have recently improved their treatment of gluon radiation in top events, these improvements are confined to the decay phase of the event[4]. Unfor-

---

[3]This helps to stabilize the fit.

[4]`HERWIG 6.1`[24], for example, incorporates the explicit matrix element for the process $t \rightarrow Wbg$

tunately, the largest contribution to experimentally resolvable extra jet production, *i.e.* a stiff isolated gluon, comes from the production stage of a top event[28][29].

Thus, to properly model the expected jet multiplicity distributions, I, in collaboration with D.Rainwater[5], have incorporated the exact leading order[6] matrix elements generated by `MADGRAPH`[32] for the processes $q\bar{q} \rightarrow t\bar{t}g, qg \rightarrow t\bar{t}q, gg \rightarrow t\bar{t}g$, and $q\bar{q} \rightarrow t\bar{t}gg$ into `PYTHIA 6.115`[26]. For consistency, and to provide a means to check our code, we also inserted matrix elements for the processes $q\bar{q} \rightarrow t\bar{t}, gg \rightarrow t\bar{t}$ which, of course, already exist in `PYTHIA`. The contributing diagrams are shown in Figures 5.2-5.9. The ME take care of the hard gluon radiation in the production phase, `PYTHIA`'s PS scheme then takes care of the soft gluon radiation in the decay phase of the event. With this division into production/decay phases, double counting (of gluons) is avoided. The details of this procedure will appear in a forthcoming note. The $t\bar{t}g, t\bar{t}gg$ matrix elements contain soft singularities due to the massless gluon(s). These are removed by requiring $p_T^g > p_T^{min}$ where p_T^{min} is chosen so as to make the calculations largely perturbative, yet is sufficiently below any threshold which might be applied to count jets after simulation in QFL$'$ (see sub-section 4.8.1). In this thesis, $p_T^{min} = 10$ GeV is chosen. The $t\bar{t}gg$ matrix element also contains a collinear singularity. This is removed by the requirement that the gluons be separated in space with $\Delta R(gg) > \Delta R(gg)^{min}$, where $\Delta R = \sqrt{\Delta\phi^2 + \Delta\eta^2}$. In this thesis, $\Delta R(gg)^{min} = 0.4$ is

---

[5]FNAL Theoretical Physics

[6]NLO not available. Higher order corrections will mainly effect p_T distributions and consequently the normalization, but not the shape, of the jet multiplicity distributions.
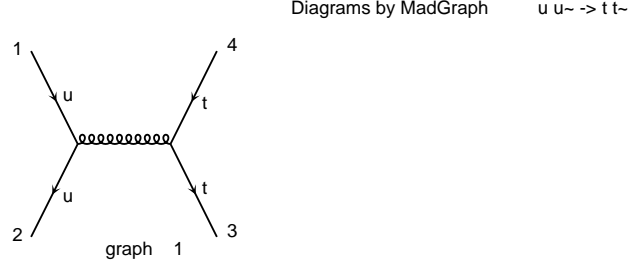
Figure 5.1: *Contributing diagram to $qq \rightarrow t\bar{t}$* MADGRAPH *matrix element.*
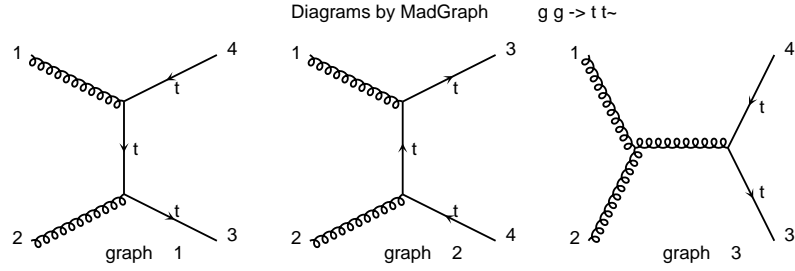
Figure 5.2: *Contributing diagrams to $gg \rightarrow t\bar{t}$* MADGRAPH *matrix element.*

chosen. The choices for p_T^{min} and $\Delta R(gg)^{min}$ are discussed in Appendix C.

5.2.2   Simulation

Using the MADGRAPH matrix elements inserted into PYTHIA 6.115 + QFL$'$ for detector simulation, with CTEQ4L for the parton distribution functions, and M_{top} as the renormalization scale[7], Monte Carlo samples[8] are produced for the $t\bar{t}, t\bar{t}j$, and

---

[7]M_{top} set to 175 GeV

[8]300,000 events were generated.

83
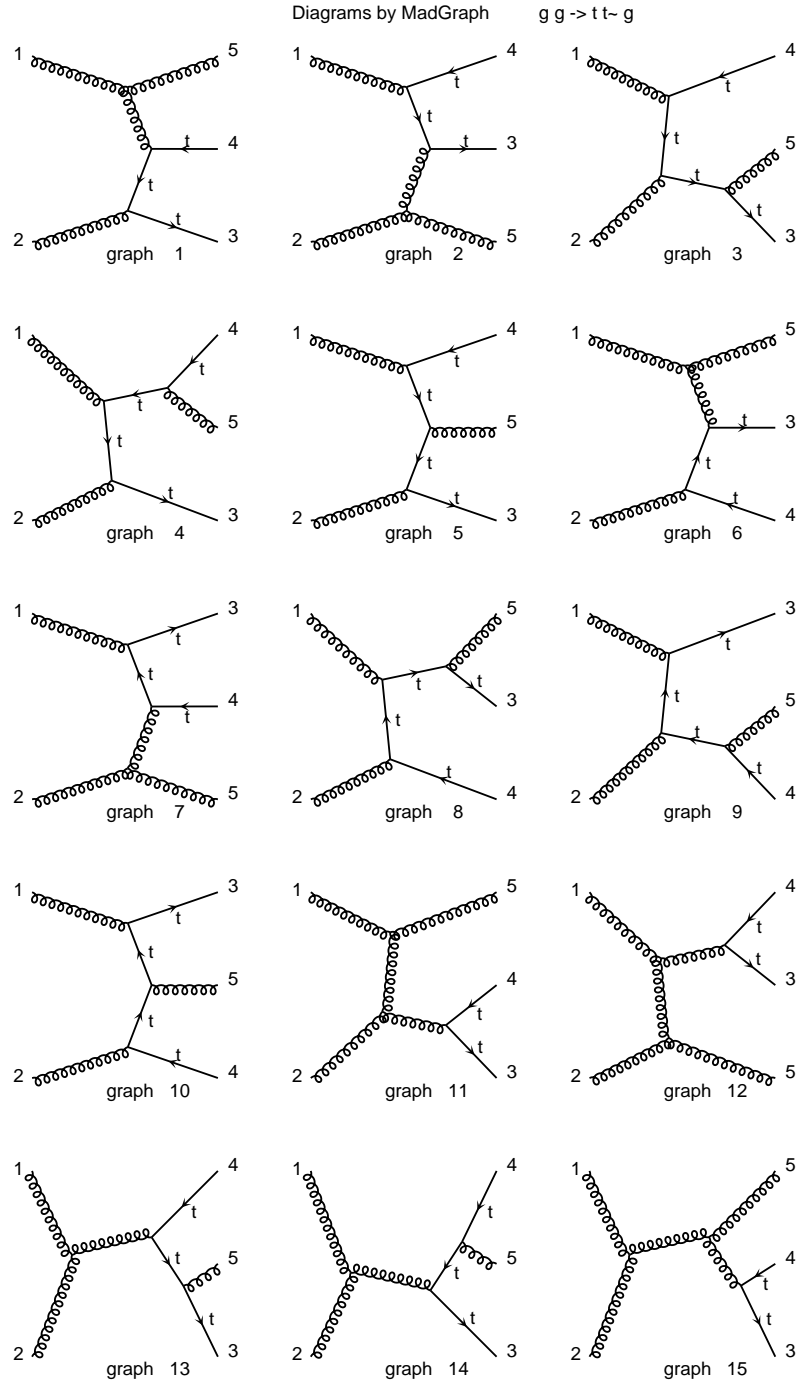
Figure 5.3: *Contributing diagrams to $gg \to t\bar{t}g$* MADGRAPH *matrix element.*
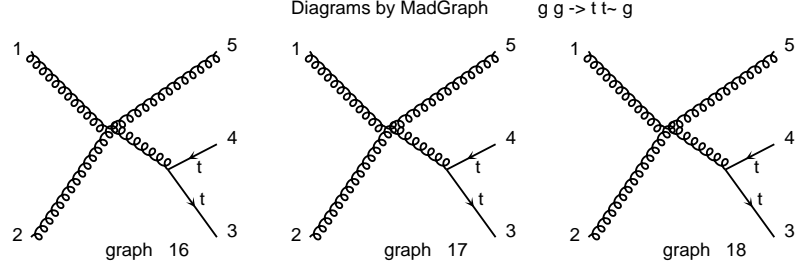
Figure 5.4: *Contributing diagrams to* $gg \rightarrow t\bar{t}g$ MADGRAPH *matrix element (cont.)*.
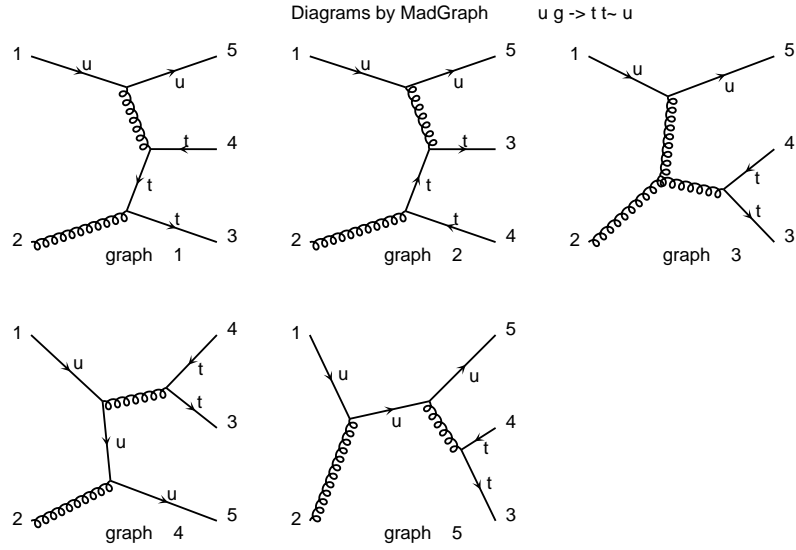
Figure 5.5: *Contributing diagrams to* $gq \rightarrow t\bar{t}q$ MADGRAPH *matrix element*.
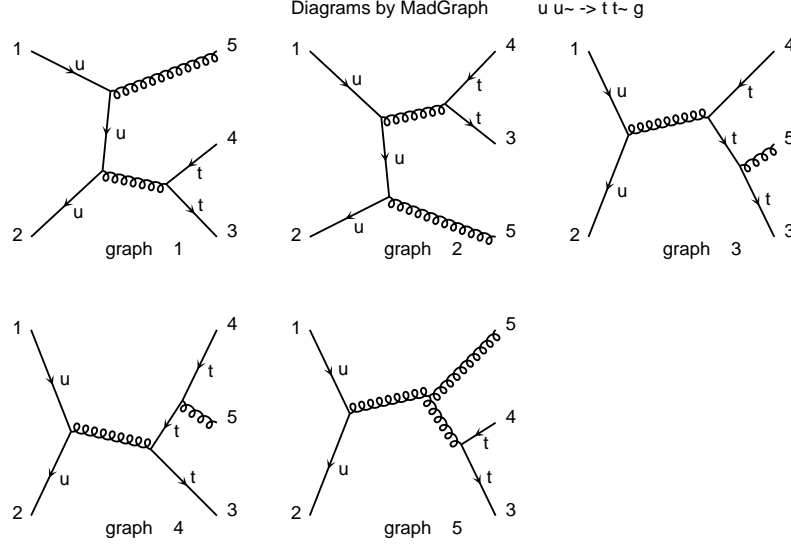
Figure 5.6: *Contributing diagrams to $qq \to t\bar{t}g$* `MADGRAPH` *matrix element.*

$t\bar{t}jj$ signal processes. Since these samples will be used to generate the template jet multiplicity distributions, the $t\bar{t}j$, $t\bar{t}jj$ samples are required to contain a production stage (from the matrix element) gluon(quark) jet(s) after simulation in `QFL`$'$ with a corrected E_T greater than or equal to the counting threshold. To accomplish this, gluons(quarks) from the ME must be matched to reconstructed jets in `QFL`$'$. The criterion for this match is $\Delta R < 0.5$ between the 4-momenta of the parton and the jet axis. The choice of this cut is discussed in Appendix D. For the background processes `VECBOS` $W + 2j$ with $b\bar{b}$ forced, followed by `HERPRT` is used. These samples are run through the same selection cuts as was done for the data and jet multiplicity distributions, $N_{jet}^{t\bar{t}}, N_{jet}^{t\bar{t}j}, N_{jet}^{t\bar{t}jj}$ and N_{jet}^{bkgnd} are produced.

Diagrams by MadGraph   u u~ -> t t~ g g
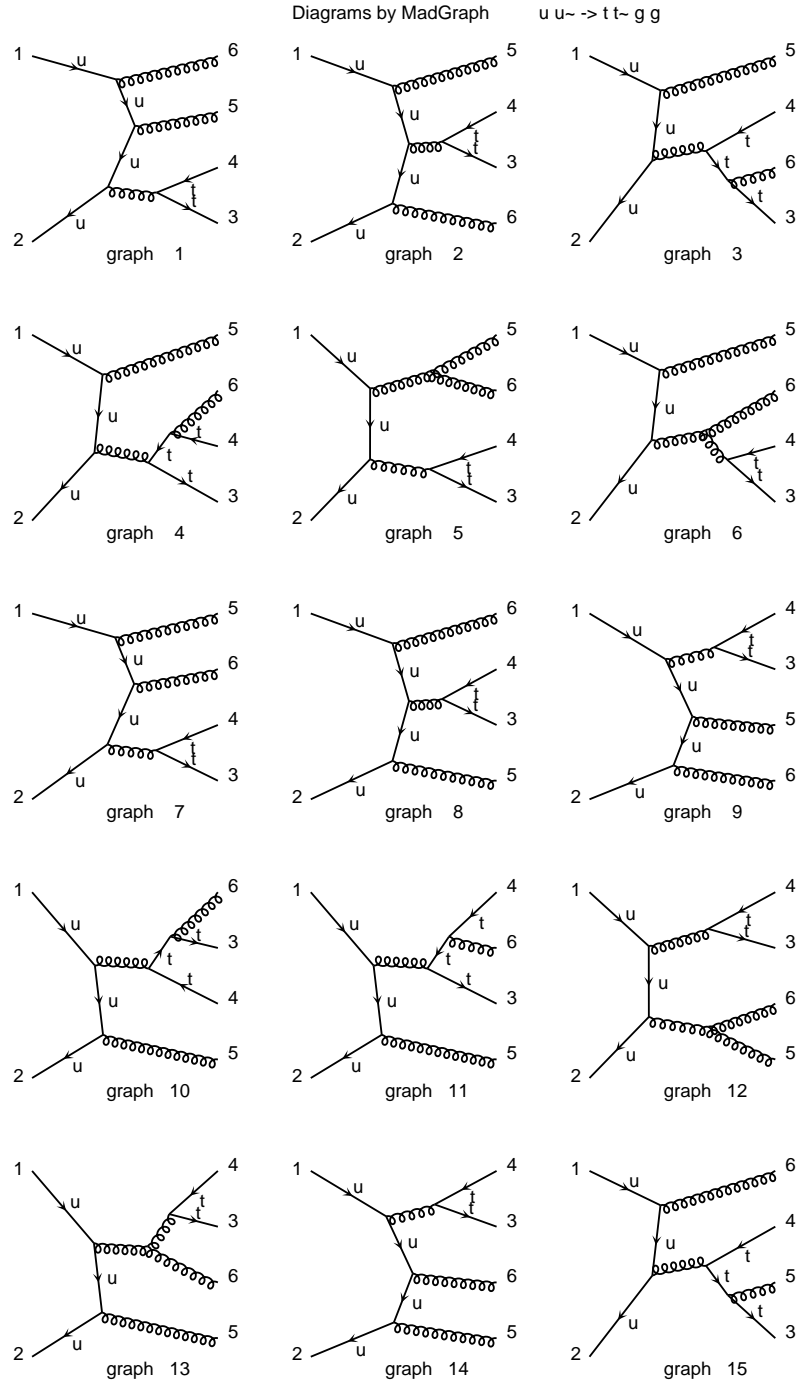
Figure 5.7: *Contributing diagrams to* $qq \rightarrow t\bar{t}gg$ `MADGRAPH` *matrix element.*

Diagrams by MadGraph   u u~ -> t t~ g g

graph 16

graph 17

graph 18

graph 19

graph 20

graph 21

graph 22

graph 23

graph 24

graph 25

graph 26

graph 27

graph 28

graph 29

graph 30
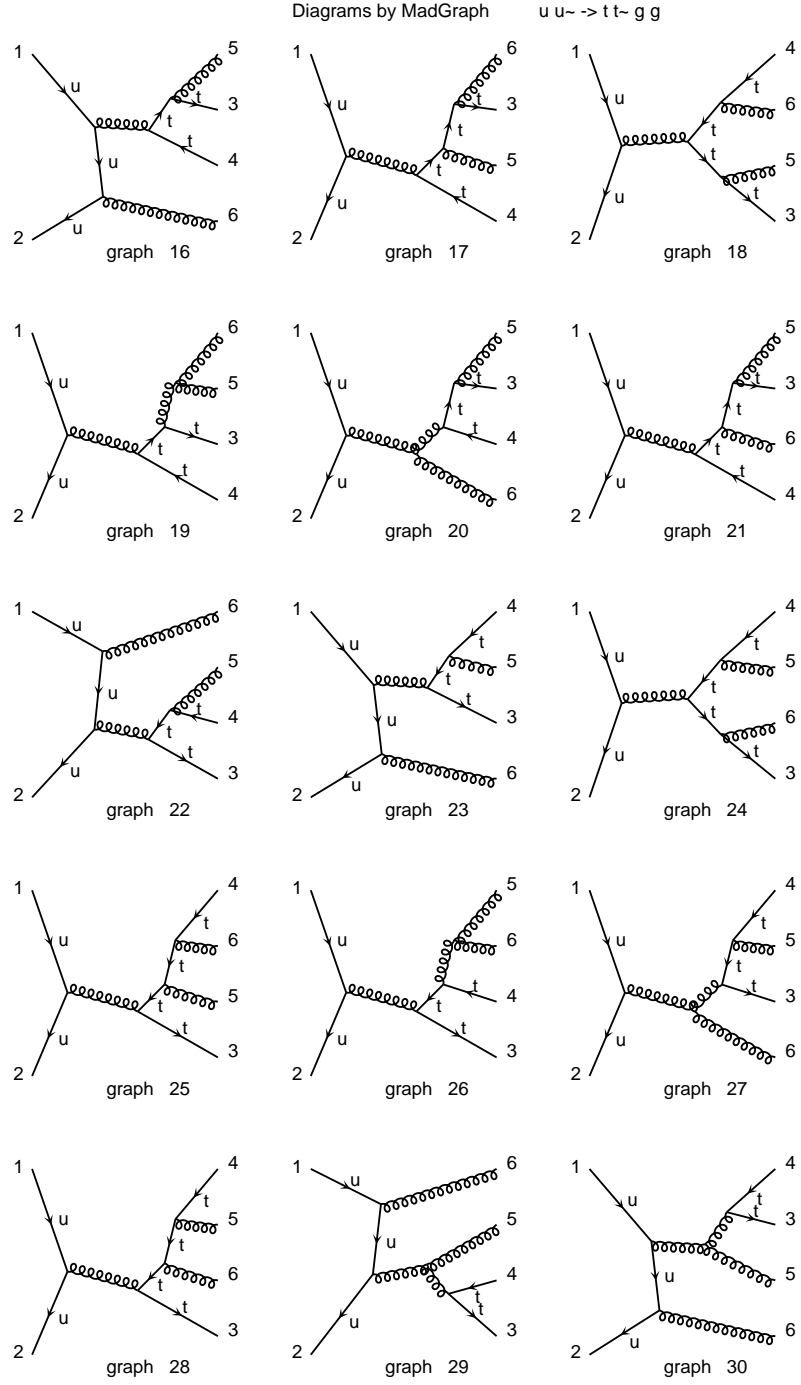
Figure 5.8: *Contributing diagrams to* $qq \to t\bar{t}gg$ `MADGRAPH` *matrix element (cont.).*
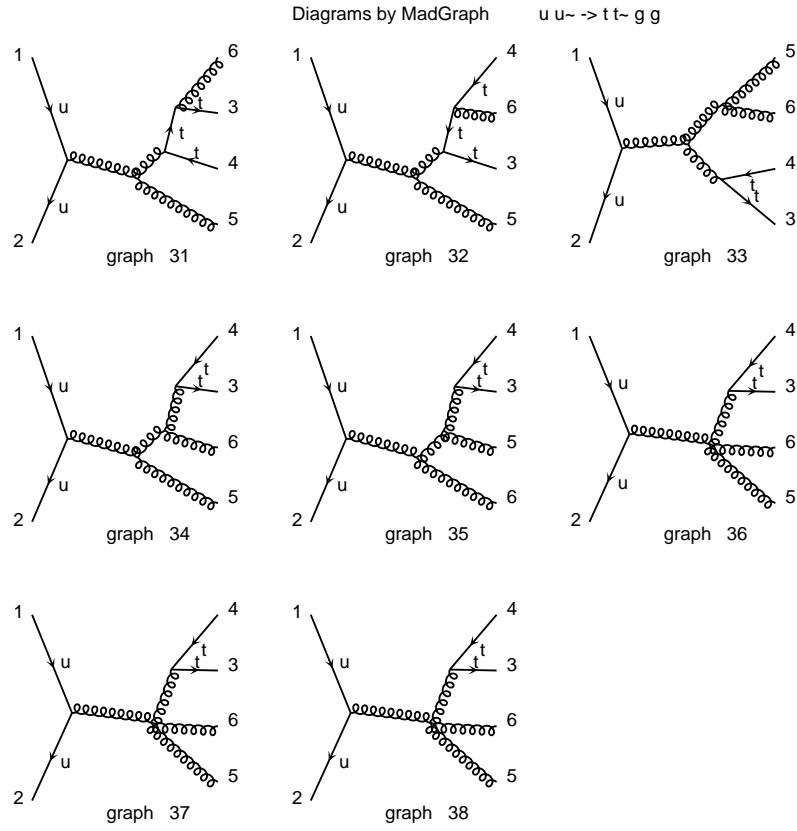
Figure 5.9: *Contributing diagrams to* $qq \rightarrow t\bar{t}gg$ `MADGRAPH` *matrix element (cont.).*

5.2.3 Jet Energy Corrections

Raw measured jet energies are corrected for both detector effects (*e.g.* cracks in the detector) and physics effects (*e.g.* missing energy due to neutrinos in semi-leptonic decays). These corrections are briefly described in the following sections.

Relative Jet Energy Scale

The relative jet energy scale is a generic jet correction applied to remove the η-dependence of the calorimeter response of forward jets relative to those in the central region. This correction must be applied first, *i.e.* all further jet corrections assume "central" jets with no η-dependence.

Absolute Jet Energy Scale

The absolute energy scale is a generic jet correction that accounts for energy losses due to both detector response and fragmentation effects. Electron and pion test-beam data as well as isolated pions in min-bias[9] events were used to determine the detector response.

---

[9]Minimum bias events are events which are triggered solely by the beam-beam counters and are generally soft QCD interactions. The min-bias cross-section is on the order of millibarns.

Parton Specific Corrections

In addition to the above generic jet corrections, the following top specific jet corrections[33] are applied separately for:

- generic b-jets (identified by an SECVTX tag)

- b-jets containing a semi-leptonic $b \rightarrow \mu\nu X$ (identified by an SLT tag)

- b-jets containing a semi-leptonic $b \rightarrow e\nu X$ (identified by an SLT tag)

- non b-jets (not tagged by either SECVTX or SLT)

These corrections were derived from a study of $t\bar{t}$ events generated with HERWIG.

5.2.4 Jet Counting

Jets in CDF are normally counted if the uncorrected E_T of the jet exceeds a certain threshold, *e.g.* Njet15 might be the number of jets in the event with $E_T > 15$ GeV. I, however, count jets *after* jet corrections are applied, that is, I count[10] a jet if its corrected E_T exceeds a certain threshold E_T^{thresh}. This is done because accurate jet energies will be crucial when forming the template jet multiplicity distributions. Moreover, counting jets in this way, facilitates comparison to theoretical cross sections which are usually expressed in terms of parton level energies. In this thesis, jet

---

[10]Here I mean counting jets to get the jet multiplicity distributions, N_{jet}. Jets are counted in the standard way for event selection.

counting thresholds of 15, 20, and 25 GeV are employed to get a crude estimate of how gluon(quark) emission depends on E_T.

5.2.5   Check of Background Monte Carlo

The background estimates given in section 4.9 are tabulated as a function of standard CDF jet multiplicity (uncorrected $E_T > 15$ GeV). In this analysis, jets are counted after corrections, so how the background estimates change when jet corrections are applied must be investigated. In other words, in order to achieve:

$$N_{jet}^{bkgnd} \xrightarrow{corr} N_{jet}^{bkgnd'}$$

one needs to know how the background transforms under jet corrections. `VECBOS` $W + 2j$ with $b\bar{b}$ is used to model this transformation. Note, it is the transformation of the shape of the jet multiplicity distribution that is being modeled. The normalization is left unchanged. This is ensured by scaling the entries bin by bin in the uncorrected jet multiplicity distribution of the `VECBOS` MC, to match the calculated (uncorrected) background numbers enumerated in Table 4.9.

To check that `VECBOS` adequately models the background transformation, I use the $W + 1$ jet (uncorrected $E_T > 15$ GeV) bin of the data, because this is virtually all background. I perform the jet corrections[11] and compare the resulting jet multiplicity distributions to those derived after the correction of the $W + 1$ jet (uncorrected

---

[11]To maximize the statistics of the data sample, jet corrections are applied to all the calorimeter clusters in the event, not only the one jet with uncorrected $E_T > 15$ GeV

$E_T > 15$ GeV) bin of the MC. The comparison plots are shown in Figure 5.10. Good agreement between data and MC is seen; thus, I conclude VECBOS adequately models how the background jet multiplicity distribution transforms under jet corrections.

5.2.6 Templates

The theoretical jet multiplicity distributions described above are normalized to unit area. These form the templates $\varepsilon_i^{t\bar{t}}, \varepsilon_i^{t\bar{t}j}, \varepsilon_i^{t\bar{t}jj}$ and ε_i^{bkgnd} used in the likelihood function given in sub-section 5.1.1. These templates are shown for the three counting thresholds, $E_T^{thresh} = 15, 20, 25$ GeV, in Figures 5.11, 5.12, 5.13. Examining, for example, the $E_T^{thresh} = 15$ GeV case, shows the $t\bar{t}$ distribution peaking in the 4 jet bin (as you would expect from the $bb\ell\nu jj$ final state) with some contribution to higher jet multiplicity resulting from PYTHIA's PS model for the decay phase of the event. The $t\bar{t}j$ and $t\bar{t}jj$ distributions, however, peak in the 5 jet and 6 jet bins respectively, showing the presence of the production phase gluons(quarks) originating in the MADGRAPH matrix elements.

5.3 Checks of Fitter

The performance of the above maximum likelihood fit is checked against many pseudo-experiments. A single pseudo-experiment consists of a sample of fake data one would expect if the CDF experiment were repeated with the same integrated
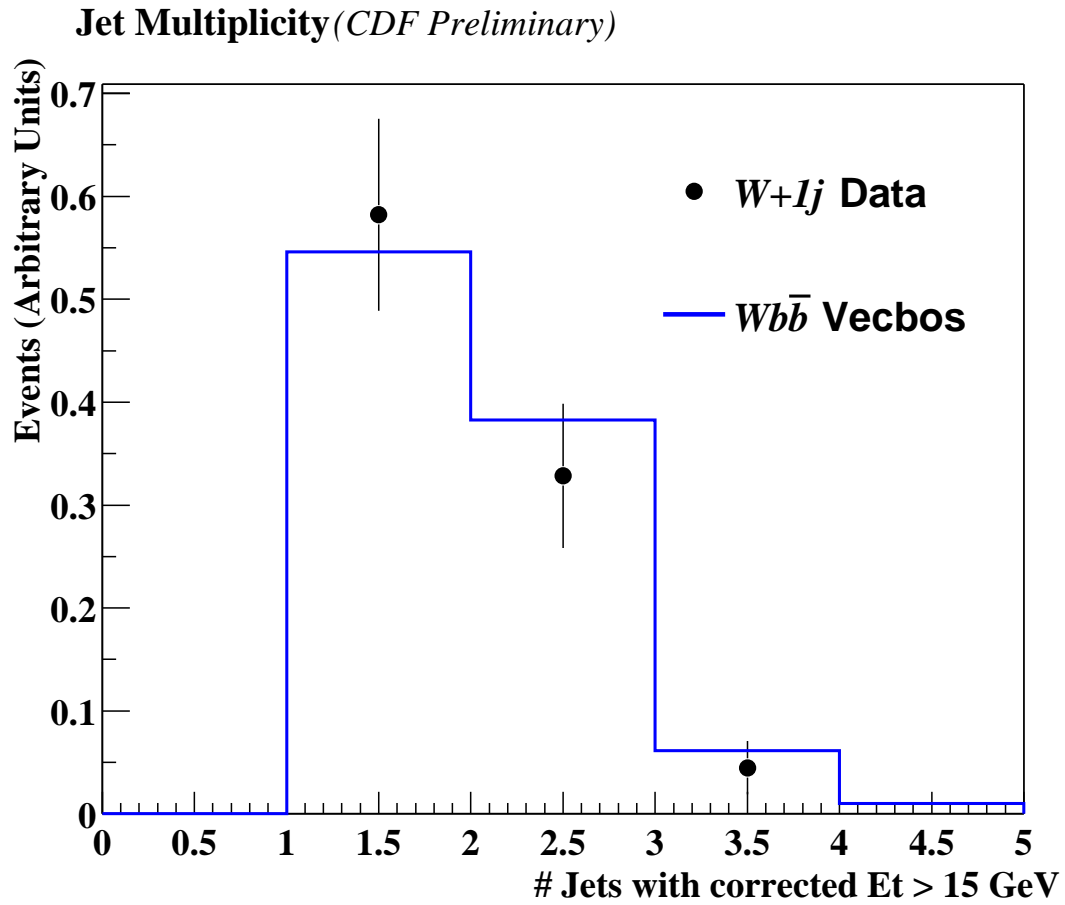
Figure 5.10: *Comparison of jet multiplicity distributions* after *jet corrections in data and* VECBOS $W + 2j$ *with* $b\bar{b}$ *forced Monte Carlo. Data are taken from the* $W + 1j$ *bin (uncorrected* $E_T > 15$ GeV*) which is all background, but is otherwise put through all selection cuts. Same is done for MC.*
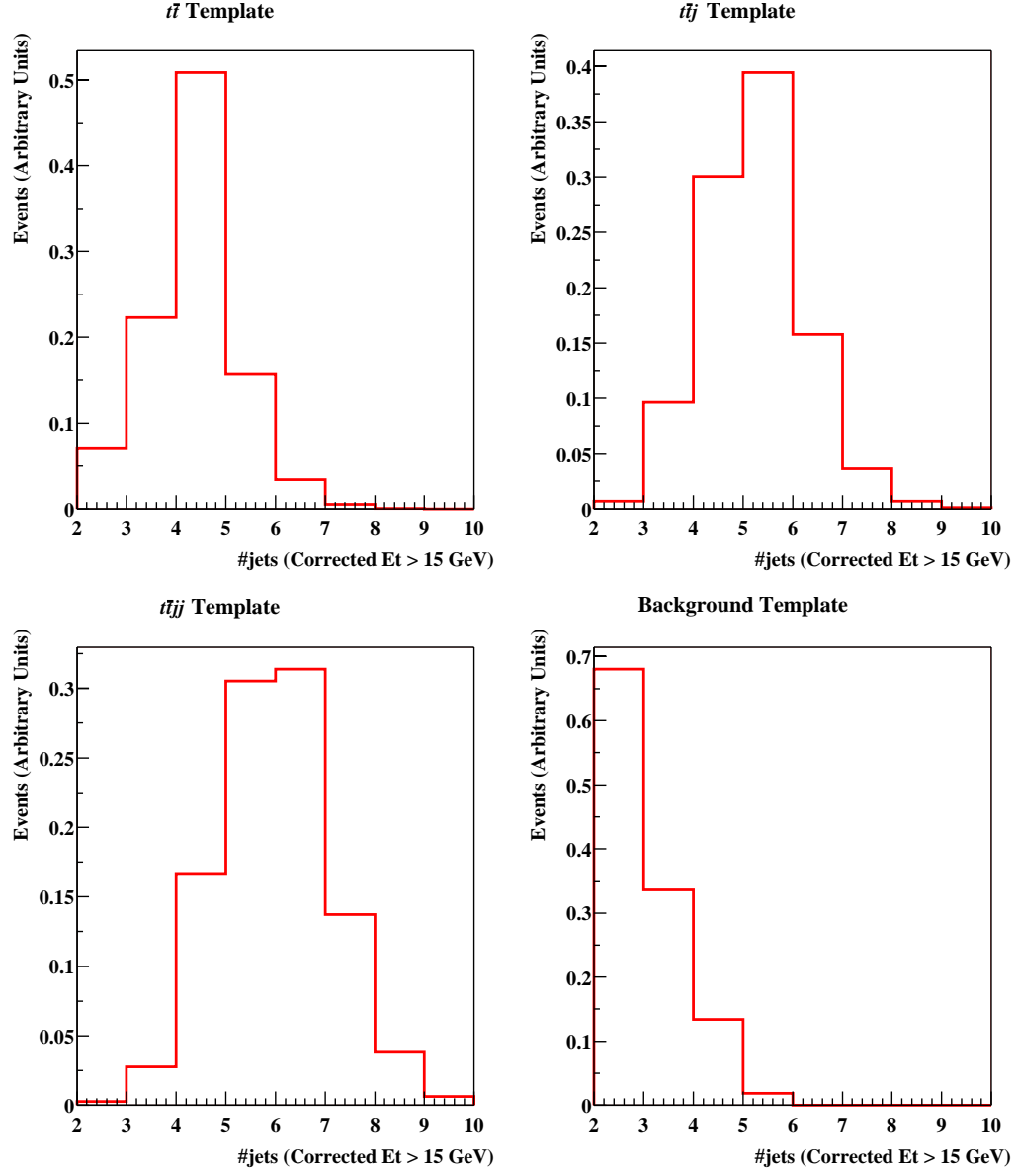
Figure 5.11: *Jet Multiplicity Distribution Templates for* $E_T^{thresh} = 15$ *GeV*
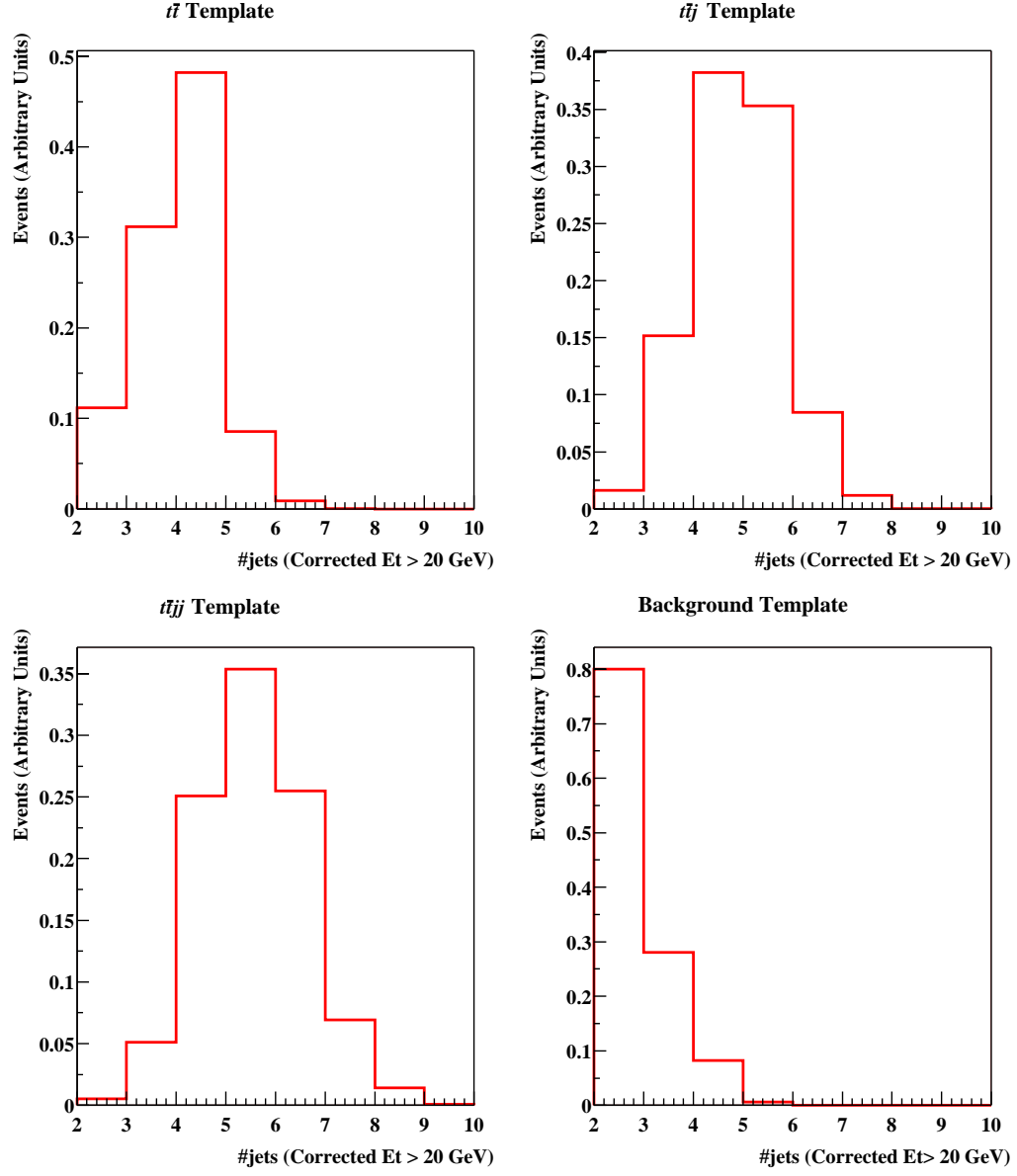
Figure 5.12: *Jet Multiplicity Distribution Templates for* $E_T^{thresh} = 20 \ GeV$
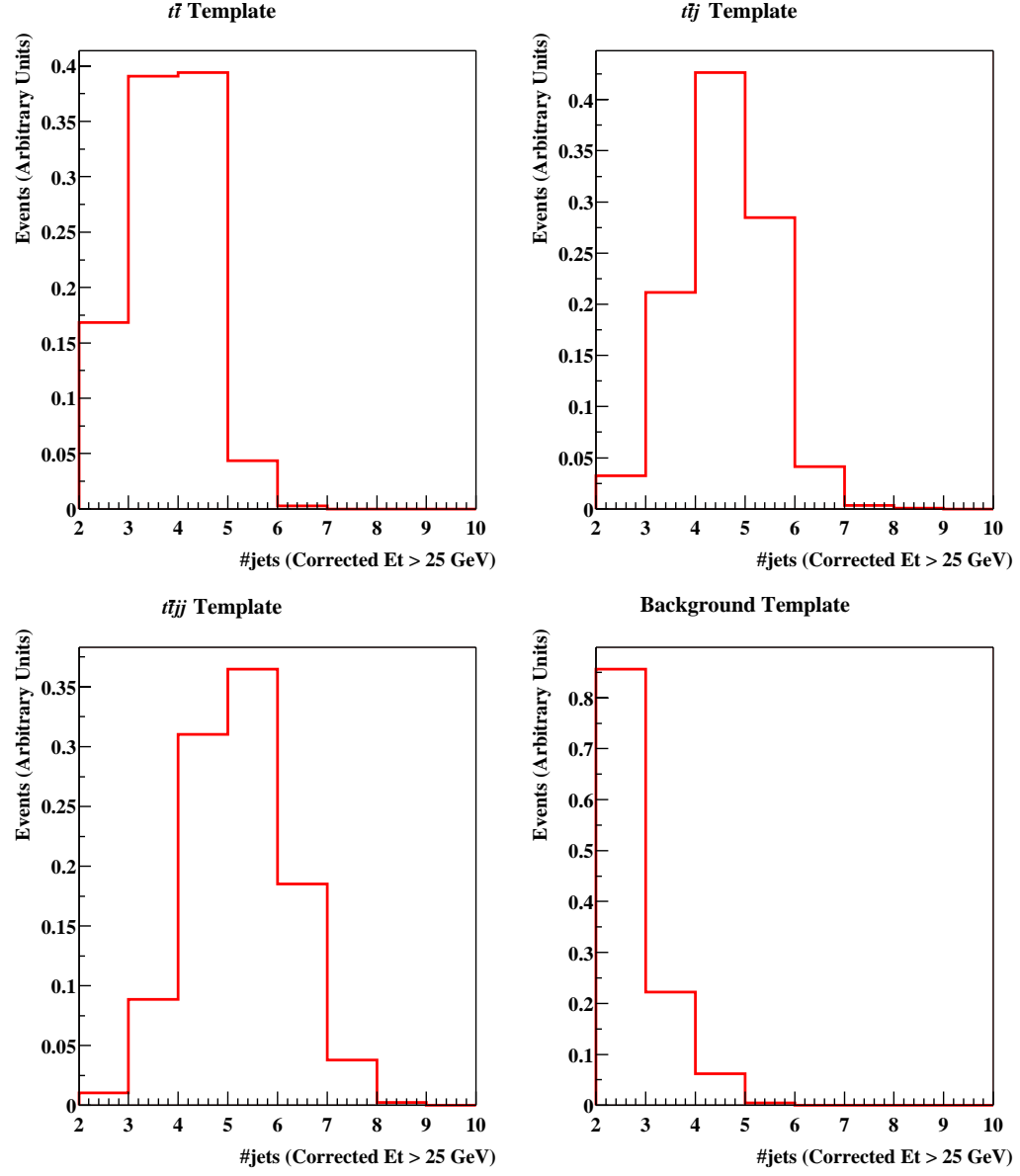
Figure 5.13: *Jet Multiplicity Distribution Templates for* $E_T^{thresh} = 25$ *GeV*

luminosity. In the context of the current analysis, a pseudo-experiment is a jet multiplicity distribution with contributions from $t\bar{t}, t\bar{t}j, t\bar{t}jj$, and background processes. This jet multiplicity distribution is generated by the following procedure:

1. Signal and background rates are estimated

$$\mu_{t\bar{t}X} = 35 = 50.72\% \; n_{tot}^{data}$$

$$\mu_{bkgnd} = 34 = 49.28\% \; n_{tot}^{data}$$

2. Since μ_{bkgnd} which appears in the likelihood via the $\mathcal{L}_{Gaussian}$ term is known with finite precision, it is gaussian-fluctuated within its uncertainty, $\sigma_{bkgnd} = 4.7$

$$\mu_{bkgnd} \xrightarrow{Gaussian} \mu'_{bkgnd}$$

3. A reasonable number of events for the mean expected value of each signal process is chosen

$$\mu_{t\bar{t}} = 20 = 28.99\% \; n_{tot}^{data}$$

$$\mu_{t\bar{t}g} = 10 = 14.49\% \; n_{tot}^{data}$$

$$\mu_{t\bar{t}gg} = \mu_{t\bar{t}g}(\frac{\mu_{t\bar{t}g}}{\mu_{t\bar{t}}}) = 7.24\% \; n_{tot}^{data}$$

4. The number of events for each process to be included in the pseudo-experiment are determined by a poisson fluctuation about the expected number of events

$$\mu_{t\bar{t}} \xrightarrow{Poisson} N_{t\bar{t}}$$

$$\mu_{t\bar{t}g} \xrightarrow{Poisson} N_{t\bar{t}g}$$

$$\mu_{t\bar{t}gg} \xrightarrow{Poisson} N_{t\bar{t}gg}$$

$$\mu'_{bkgnd} \xrightarrow{Poisson} N_{bkgnd}$$

5. Finally, the jet multiplicity for each of the $N_{process}$ events determined above, is determined by throwing a random number against the normalized jet multiplicity template for that process.

10,000 of such pseudo-experiments were generated. For each of the 10,000 pseudo-experiments, the fit is then performed by MINUIT with the likelihood function $\mathcal{L}$ described above. The resulting distributions of the fit parameters are shown in Figure 5.14. The pull distributions for each of the fitted parameters are plotted in Figure 5.15 where pull is defined as for fit parameter f, with input μ:

$$\frac{f - \mu}{\sigma_f} \tag{5.7}$$

The fit distributions are centered at their input values with pull distributions that have means which deviate from zero at levels which are far below the statistical uncertainty of the measurement. The standard deviations of the pull distributions are essentially equal to one. The negative skew, and poor gaussian fit, of the $t\bar{t}j$ pull distribution is a direct effect of poisson statistics. The poisson distribution is asymmetric about its mean, so too will be the poisson fluctuated pseudo-experiments. For comparison, an ideal (in the sense of a perfectly correct fit) poisson "pull" distribution has been

generated for 100,000 events with an expected mean of 10 (the number of expected $t\bar{t}j$). This distribution is plotted directly below the $t\bar{t}j$ pull distribution in Figure 5.15. It can be seen that there is good agreement between these distributions. These facts indicate the fitter is performing adequately.

5.4 Fit Results on Data

The likelihood fit described in sub-section 5.1.1 is applied to the 70 events selected from the CDF Run 1A+1B dataset three times with the jet multiplicity templates with $E_T^{thresh} = 15, 20, 25$ GeV. This is done to get a crude estimate of the E_T dependence of the gluon radiation. Since the data does not populate jet multiplicity bins greater than six, bin 6 is made to be inclusive, $i.e. \geq 6$ jets. The fit is therefore over 5 bins. I am fitting for 3 parameters, so the fit has $5 - 3 = 2$ degrees of freedom. In, the following discussion, I refer it to this fit as "$t\bar{t} + t\bar{t}j + t\bar{t}jj$". The results are displayed in Table 5.1. The errors quoted are those calculated by the MINOS algorithm in the MINUIT minimization package[30], except for the error on the $t\bar{t}jj$ fraction which is calculated by hand using the error matrix provided by MINUIT. The MINOS algorithm numerically applies the likelihood ratio method in which the s-standard deviation errors are determined from the contour given by the α' such that

$$\log \mathcal{L}(\alpha') = \log \mathcal{L}_{max} - s^2/2 \tag{5.8}$$

Test of Fitter (10,000 P.E.)
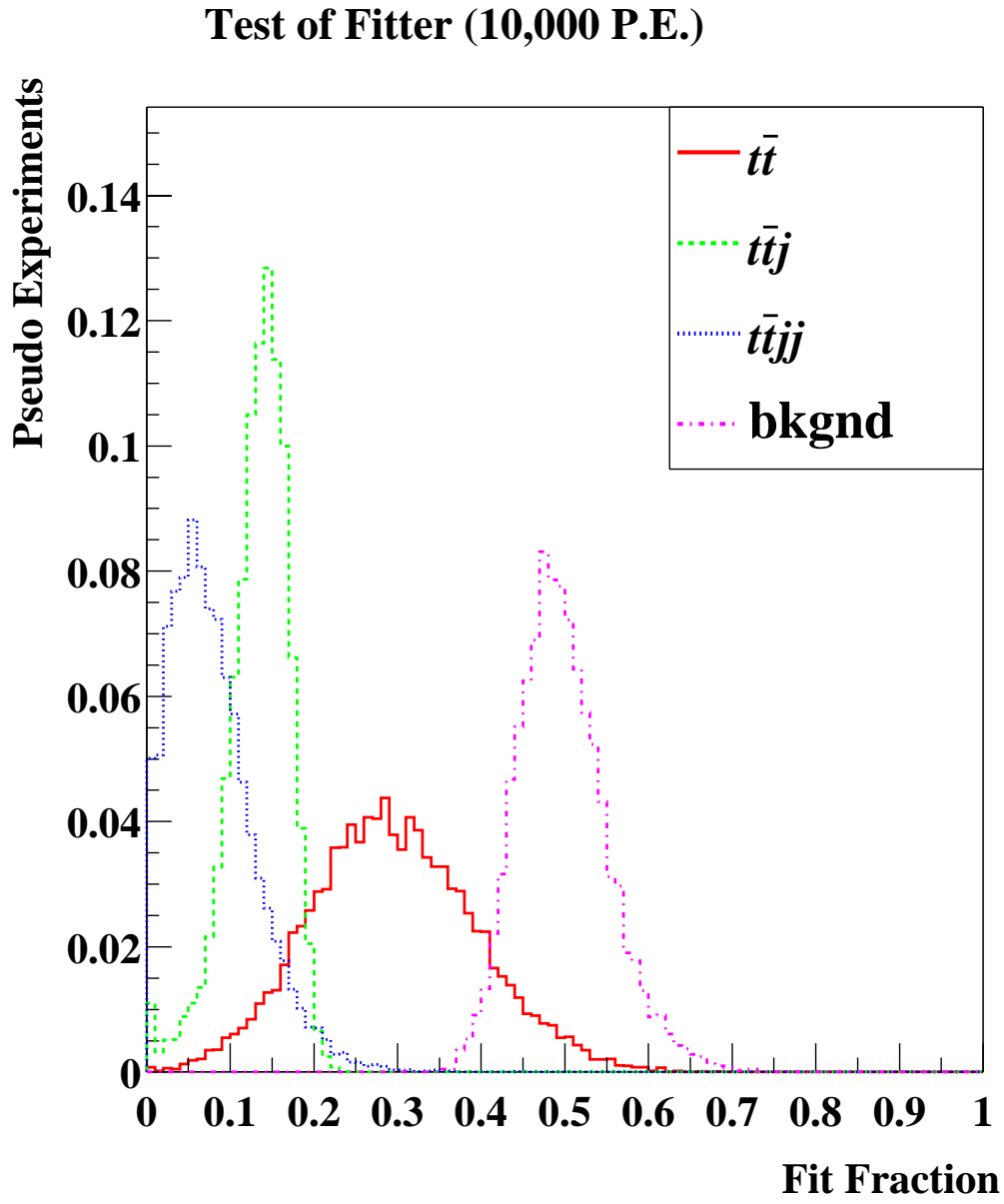
Figure 5.14: *Distributions of fitted fractions for input values .2899, .1449, .0724, .4928 for $f_{t\bar{t}}, f_{t\bar{t}j}, f_{t\bar{t}jj}, f_{bkgnd}$ respectively*
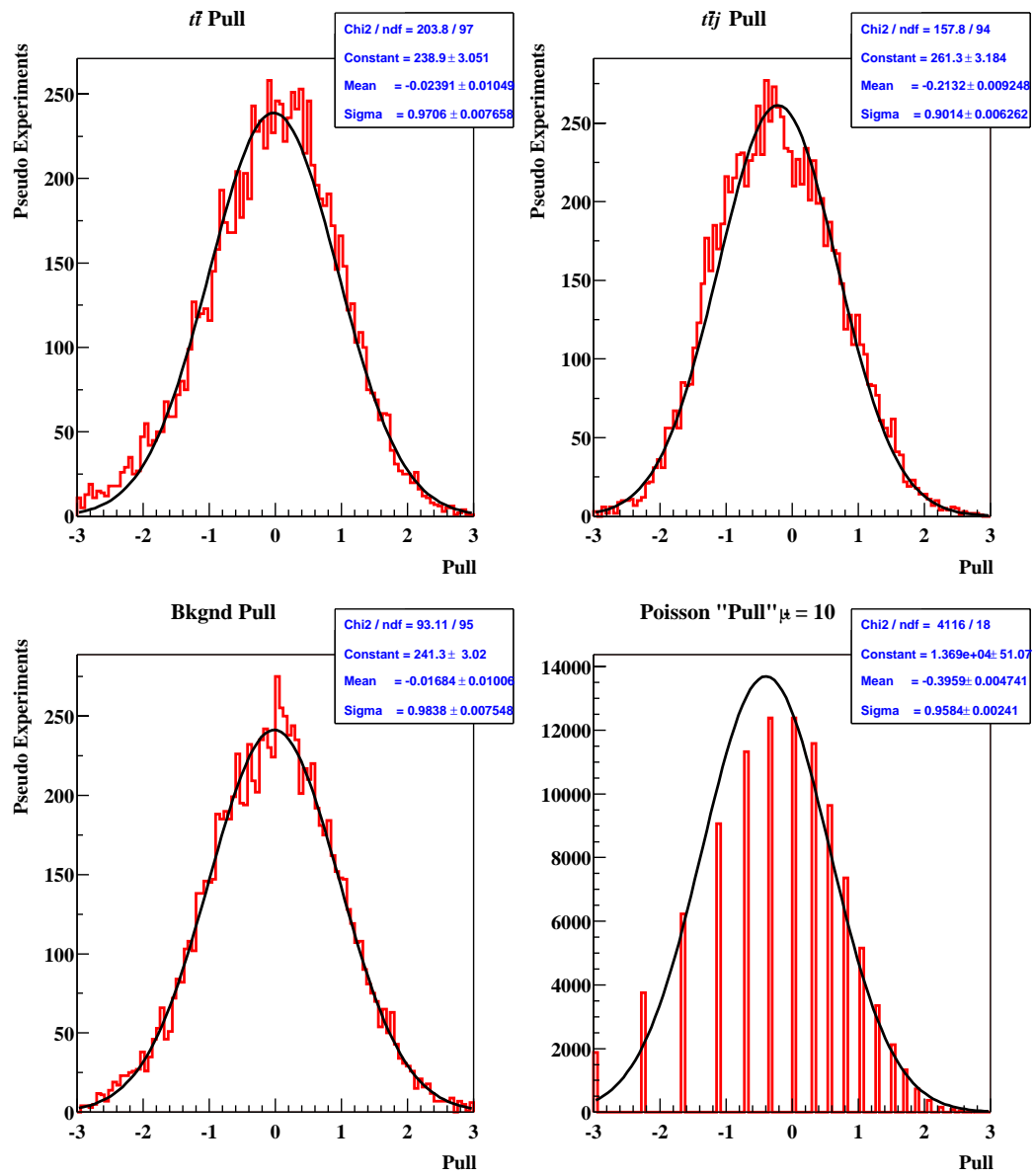
Figure 5.15: *Pull Distributions*

These errors are statistical only.

The small fitted fractions for $t\bar{t}j$ suggest that the $t\bar{t}jj$ component may be negligible after all, and that perhaps a better fit to the data could be obtained by removing the $t\bar{t}jj$ term from the likelihood function. This modified likelihood fit is applied to the data as before. In, the following discussion, I refer it to this fit as "$t\bar{t} + t\bar{t}j$". The results are displayed in Table 5.2. The errors quoted are those calculated by the MINOS algorithm in the MINUIT minimization package[30] and are statistical only.

For completeness, I have also fit the data with both the $t\bar{t}j$, and $t\bar{t}jj$ terms removed, leaving only the $t\bar{t}$ template. Recall from section 5.2.6 that this template is $t\bar{t}$ plus decay phase radiation. This fit therefore tests the hypothesis that all radiation in the event is due to the decay phase. In the following discussion, I refer it to this fit as "DPR only". The results are displayed in Table 5.3. The errors quoted are those calculated by the MINOS algorithm in the MINUIT minimization package[30] and are statistical only.

Jet multiplicity distributions of the CDF data for each jet energy threshold with each of the three fits overlaid is displayed in Figures 5.16,5.17,5.18.
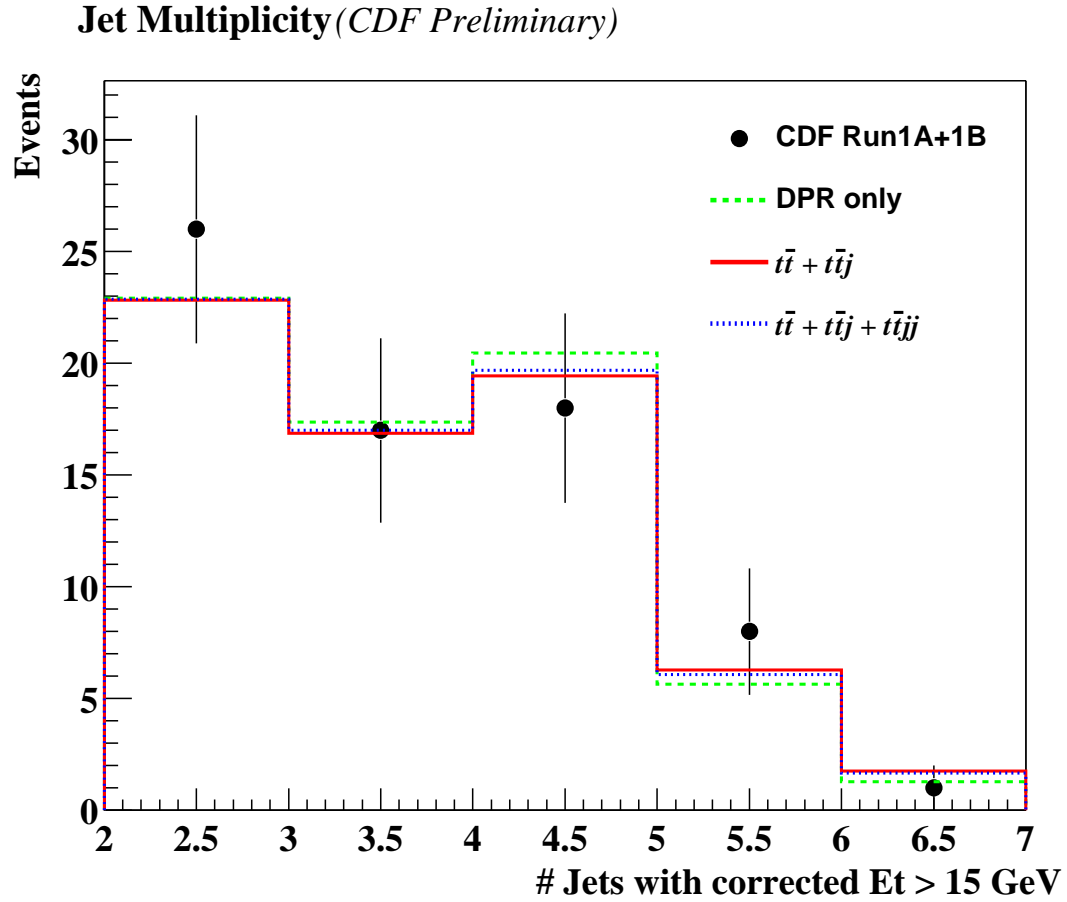
Figure 5.16: *CDF Run 1A+1B data jet multiplicity for jets with corrected $E_T > 15$ GeV, together with the DPR only, $t\bar{t} + t\bar{t}j$, and $t\bar{t} + t\bar{t}j + t\bar{t}jj$ fits overlaid.*
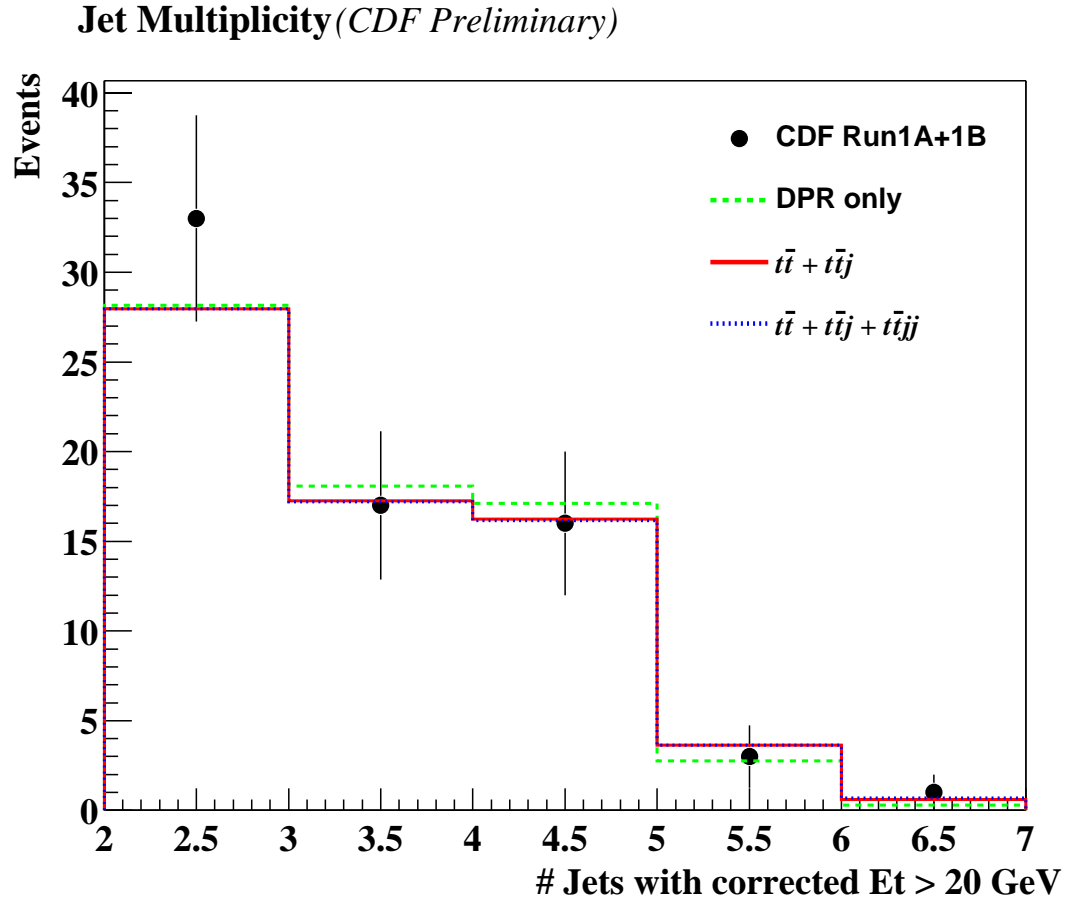
Figure 5.17: *CDF Run 1A+1B data jet multiplicity for jets with corrected $E_T > 20$ GeV, together with the DPR only, $t\bar{t} + t\bar{t}j$, and $t\bar{t} + t\bar{t}j + t\bar{t}jj$ fits overlaid.*
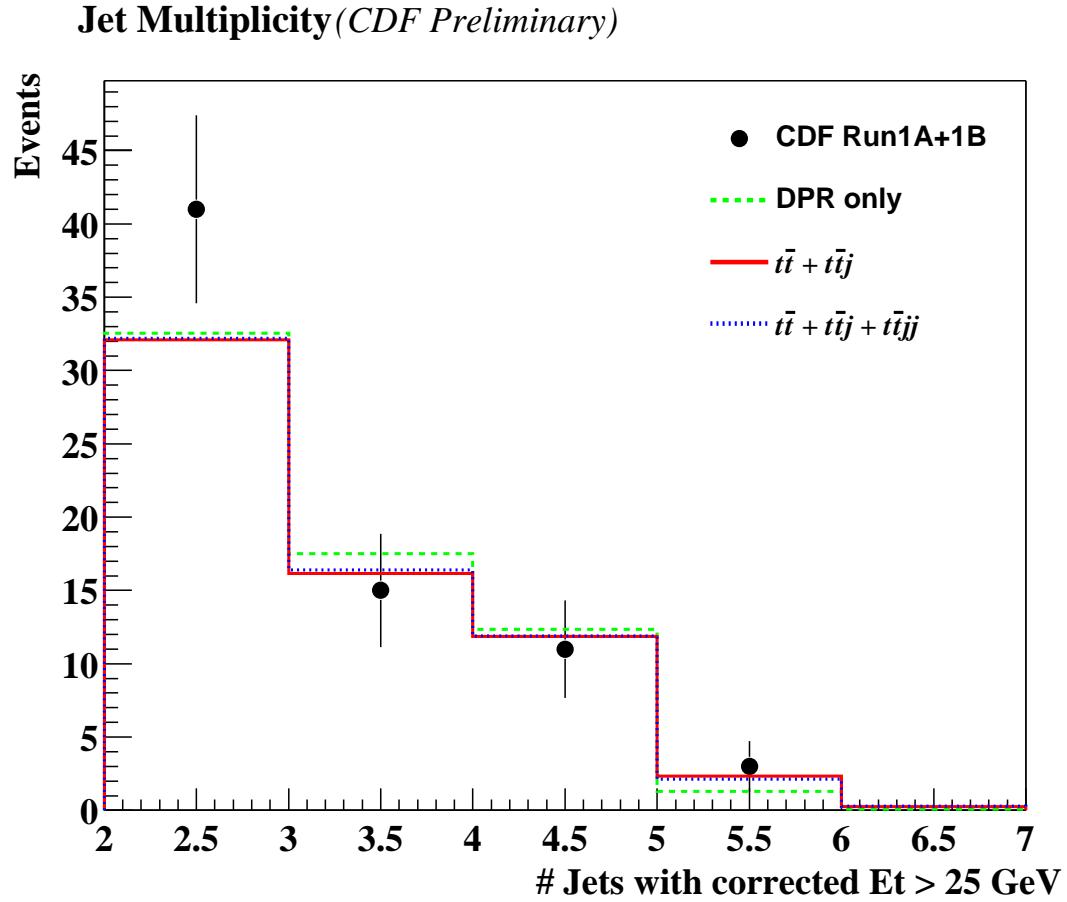
Figure 5.18: *CDF Run 1A+1B data jet multiplicity for jets with corrected $E_T > 25$ GeV, together with DPR only, $t\bar{t} + t\bar{t}j$, and $t\bar{t} + t\bar{t}j + t\bar{t}jj$ fits overlaid.*

Fraction	E_T^{thresh}	Fitted Value
$t\bar{t}$	15 GeV	$0.4197^{+0.1446}_{-0.1246}$
$t\bar{t}$	20 GeV	$0.3626^{+0.1261}_{-0.1108}$
$t\bar{t}$	25 GeV	$0.3038^{+0.1246}_{-0.1096}$
$t\bar{t}j$	15 GeV	$0.03053^{+0.0585}_{-0.0787}$
$t\bar{t}j$	20 GeV	$0.0459^{+0.0461}_{-0.0514}$
$t\bar{t}j$	25 GeV	$0.0443^{+0.0431}_{-0.0480}$
$t\bar{t}jj$	15 GeV	$0.0022^{+0.0090}_{-0.0118}$
$t\bar{t}jj$	20 GeV	$0.0058^{+0.0128}_{-0.0140}$
$t\bar{t}jj$	25 GeV	$0.0064^{+0.0141}_{-0.0154}$
$bkgnd$	15 GeV	$0.5093^{+0.0573}_{-0.0565}$
$bkgnd$	20 GeV	$0.5232^{+0.0569}_{-0.0561}$
$bkgnd$	25 GeV	$0.5443^{+0.0569}_{-0.0561}$

Table 5.1: *Results of likelihood fit as a function of E_T^{thresh} using full fit.*

Fraction	E_T^{thresh}	Fitted Value
$t\bar{t}$	15 GeV	$0.4040^{+0.1561}_{-0.1455}$
$t\bar{t}$	20 GeV	$0.3642^{+0.1304}_{-0.1239}$
$t\bar{t}$	25 GeV	$0.2838^{+0.1343}_{-0.1297}$
$t\bar{t}j$	15 GeV	$0.0453^{+0.1049}_{-0.0865}$
$t\bar{t}j$	20 GeV	$0.0511^{+0.0841}_{-0.0591}$
$t\bar{t}j$	25 GeV	$0.0658^{+0.0903}_{-0.0653}$
$bkgnd$	15 GeV	$0.5105^{+0.0576}_{-0.0566}$
$bkgnd$	20 GeV	$0.5229^{+0.0570}_{-0.0561}$
$bkgnd$	25 GeV	$0.5460^{+0.0570}_{-0.0563}$

Table 5.2: *Results of likelihood fit as a function of E_T^{thresh} using $t\bar{t}j$ fit.*

Fraction	E_T^{thresh}	Fitted Value
$t\bar{t}$	15 GeV	$0.4611^{+0.1059}_{-0.0952}$
$t\bar{t}$	20 GeV	$0.4314^{+0.1041}_{-0.0931}$
$t\bar{t}$	25 GeV	$0.3734^{+0.1031}_{-0.0912}$
$bkgnd$	15 GeV	$0.5061^{+0.0570}_{-0.0561}$
$bkgnd$	20 GeV	$0.5171^{+0.0567}_{-0.0558}$
$bkgnd$	25 GeV	$0.5379^{+0.0566}_{-0.0560}$

Table 5.3: *Results of likelihood fit as a function of E_T^{thresh} using $t\bar{t}$ only fit.*

5.4.1 Goodness of Fit

To evaluate the goodness-of-fit of the three fits performed on the data, a χ^2 test is performed[12]. In 1952, William G. Cochran authored a definitive review of Pearsons's χ^2 test in which he says:[34]

> Since χ^2 has been established as the limiting distribution of X^2 in large samples, it is customary to recommend, in applications of the test, that the smallest expected number in any class should be 10 or (with some writers) 5. If this requirement is not met in the original classification, combination of neighboring classes until the rule is satisfied is recommended.

Following this prescription, I merge the last two bins in each histogram, which satisfies the criterion for $E_T^{thresh} = 15$ GeV measurements, but not for the $E_T^{thresh} = 20, 25$ GeV cases. Further merging is not possible since only 1 degree of freedom remains. Fortunately, Cochran goes on to say "the numbers 10 and 5 appear to be arbitrarily chosen" and advocates allowing one expectation to be as low as one-half providing the remainder are above the conventional limits[35]. This relaxed requirement is satisfied in $E_T^{thresh} = 20, 25$ GeV measurements. The resulting reduced chi-squares and the accompanying confidence levels of the fits are given below:

- $E_T^{thresh} = 15$ GeV

  - DPR only fit: $\chi^2_\nu = 1.4022$, C.L. = 23.64%

  - $t\bar{t} + t\bar{t}j$ fit: $\chi^2_\nu = 0.8699$, C.L. = 35.09%

---

[12]The Kolmogorov-Smirnov test is not used despite it being well suited to low statistics application, because it is only valid for continuous distributions, whereas the one in question is highly discrete.

$- \; t\bar{t} + t\bar{t}j + t\bar{t}jj$ fit: $\chi_\nu^2 = 0.9948$, C.L. $= 31.86\%$

- $E_T^{thresh} = 20$ GeV

  $-$ DPR only fit: $\chi_\nu^2 = 0.8776$, C.L. $= 34.89\%$

  $- \; t\bar{t} + t\bar{t}j$ fit: $\chi_\nu^2 = 0.9116$, C.L. $= 33.97\%$

  $- \; t\bar{t} + t\bar{t}j + t\bar{t}jj$ fit: $\chi_\nu^2 = 0.9091$, C.L. $= 34.06\%$

- $E_T^{thresh} = 25$ GeV

  $-$ DPR only fit: $\chi_\nu^2 = 3.3058$, C.L. $= 6.90\%$

  $- \; t\bar{t} + t\bar{t}j$ fit: $\chi_\nu^2 = 2.2499$, C.L. $= 13.36\%$

  $- \; t\bar{t} + t\bar{t}j + t\bar{t}jj$ fit: $\chi_\nu^2 = 2.3592$, C.L. $= 12.45\%$

From the above numbers, it is evident that all three hypotheses (DPR only, $t\bar{t}+t\bar{t}j$, $t\bar{t} + t\bar{t}j + t\bar{t}jj$) fit the data equally.

5.5   Systematic Uncertainties on the Measurement

This section investigates sources of systematic error in the cross-section ratio measurement. These systematic uncertainties were estimated by re-making jet multiplicity templates for the signal (and sometimes background) processes in which a systematic effect had been varied by some amount (*e.g.* one standard deviation). Nine sets of 10,000 pseudo-experiments are generated as described in section 5.3 with input

values taken from the central values of each of the fits performed in section 5.4. Likelihood fits are performed with the shifted templates. The shift between each of the resulting fit fractions for each pseudo-experiment and those obtained with the default templates is calculated as follows for each process, $t\bar{t}, t\bar{t}j, t\bar{t}jj$ and background:

$$f_{process}^{shifted} - f_{process}^{default} \tag{5.9}$$

These quantities are histogrammed for each process, for all pseudo-experiments, and the mean of this distribution is taken to be the magnitude of the systematic shift. A sample of such a histogram is given in Figure 5.19. The estimated systematic uncertainties calculated in this way are summarized in Tables 5.4-5.6. Individual systematic uncertainties are summed in quadrature to yield the total systematic uncertainty associated with the measurement. Details on the calculation of each systematic uncertainty are listed below:

- **Jet Energy Scale**

  Since this measurement is presented as a function of corrected jet energy, it is expected that the uncertainty in the jet corrections applied will be a significant source of systematic error. To quantify this effect, jet multiplicity templates were re-made for both signal and background process with shifts in each of the sources of systematic uncertainty in the jet corrections that produce a net change of $+1\sigma$ and -1σ in the jet energy scale. $\delta\langle f_{proc}\rangle_{JetEnergy}$ is taken to be half the symmetrized difference between $\langle f_{proc}\rangle_{+1\sigma}$ and $\langle f_{proc}\rangle_{-1\sigma}$.

- **Top Quark Mass**

  The top mass is not known very precisely, and this may be a small source of systematic error. To quantify this effect, jet multiplicity templates were re-made for the signal processes with the top mass set to 170 GeV and 180 GeV instead of the default 175 GeV. The default template was used for the background. $\delta\langle f_{proc}\rangle_{M_{top}}$ is taken to be half the symmetrized difference between $\langle f_{proc}\rangle_{M_t=170}$ and $\langle f_{proc}\rangle_{M_t=180}$.

- **Parton Density Function**

  The choice of parton distribution functions used in the Monte Carlo was arbitrary and may be a small source of systematic error. To quantify this effect, jet multiplicity templates were re-made for the signal processes with the parton distribution function set GRV 94 L0 instead of the default CTEQ4L. The default template was used for the background. $\delta\langle f_{proc}\rangle_{PDF}$ is taken to be the symmetrized difference between $\langle f_{proc}\rangle_{GRV94}$ and $\langle f_{proc}\rangle_{CTEQ4L}$.

- **Monte Carlo Statistics**

  The jet multiplicity templates used in the fit were made with a finite number of events and thus themselves contain statistical uncertainty which may be a source of small systematic error. To quantify this effect, jet multiplicity templates were re-made for both the signal and background processes with 1 standard deviation fewer events generated than used for the making of the

default templates. $\delta\langle f_{proc}\rangle_{MCstats}$ is taken to be the symmetrized difference between $\langle f_{proc}\rangle_{-1\sigma}$ and $\langle f_{proc}\rangle_{default}$.

- **Renormalization Scale, μ**

  The choice of renormalization scale used in the Monte Carlo was arbitrary and may be a small source of systematic error. To quantify this effect, jet multiplicity templates were re-made for the signal processes with the renormalization scale set to $2M_{top}$ and $M_{top}/2$ instead of the default M_{top}. The default template was used for the background. $\delta\langle f_{proc}\rangle_{\mu}$ is taken to be half the symmetrized difference between $\langle f_{proc}\rangle_{2M_t}$ and $\langle f_{proc}\rangle_{M_t/2}$.

- **Delta R cut**

  The choice of the ΔR cut imposed in the generation of the templates may be a significant source of systematic error. To quantify this effect, jet multiplicity templates were re-made for the signal processes without the ΔR requirement for gluon matching (see Appendix D). The default template was used for the background. $\delta\langle f_{proc}\rangle_{\Delta R}$ is taken to be the symmetrized difference between $\langle f_{proc}\rangle_{no\Delta R}$ and $\langle f_{proc}\rangle_{default}$.

- **Decay Phase Radiation (DPR)**

  The modeling of decay phase radiation by the parton-shower routines in the Monte Carlo may under(over)-estimate the radiation which would be a large

source of systematic error. To quantify this effect, jet multiplicity templates were re-made for the signal processes with $+10\%(-10\%)$ augmentation(reduction) in the decay phase radiation contribution. Entries in the $t\bar{t}$ template with greater than four jets are assumed to be due to decay phase radiation. Entries in the $t\bar{t}j$ template with greater than five jets are assumed to be due to decay phase radiation. Entries in the $t\bar{t}jj$ template with greater than six jets are assumed to be due to decay phase radiation. $\delta\langle f_{proc}\rangle_{DPR}$ is taken to be half the symmetrized difference between $\langle f_{proc}\rangle_{+10\%}$ and $\langle f_{proc}\rangle_{-10\%}$.

5.6 Cross Section Ratio

Having fitted the data and extracted the fraction of the $t\bar{t}j$ events, all that remains is to convert this fraction into a $t\bar{t}j/t\bar{t}X$ cross-section ratio.

The cross section for a given process is given by the following expression:

$$\sigma = \frac{N_{obs}}{\epsilon \cdot \int \mathcal{L}dt} \tag{5.10}$$

where ϵ is the total event detection efficiency and $\int \mathcal{L}dt$ is the total integrated luminosity delivered to the experiment. The efficiency is in general a complicated function of many parameters. For example, the efficiency for detecting an inclusive $t\bar{t}$ event may be calculated as follows[36]:

$$\epsilon_{t\bar{t}X} = A_{t\bar{t}X} \cdot \epsilon_{|z_{vtx}|} \cdot \epsilon_{trig} \cdot \epsilon_{leptonid} \cdot \epsilon_{tag} \tag{5.11}$$
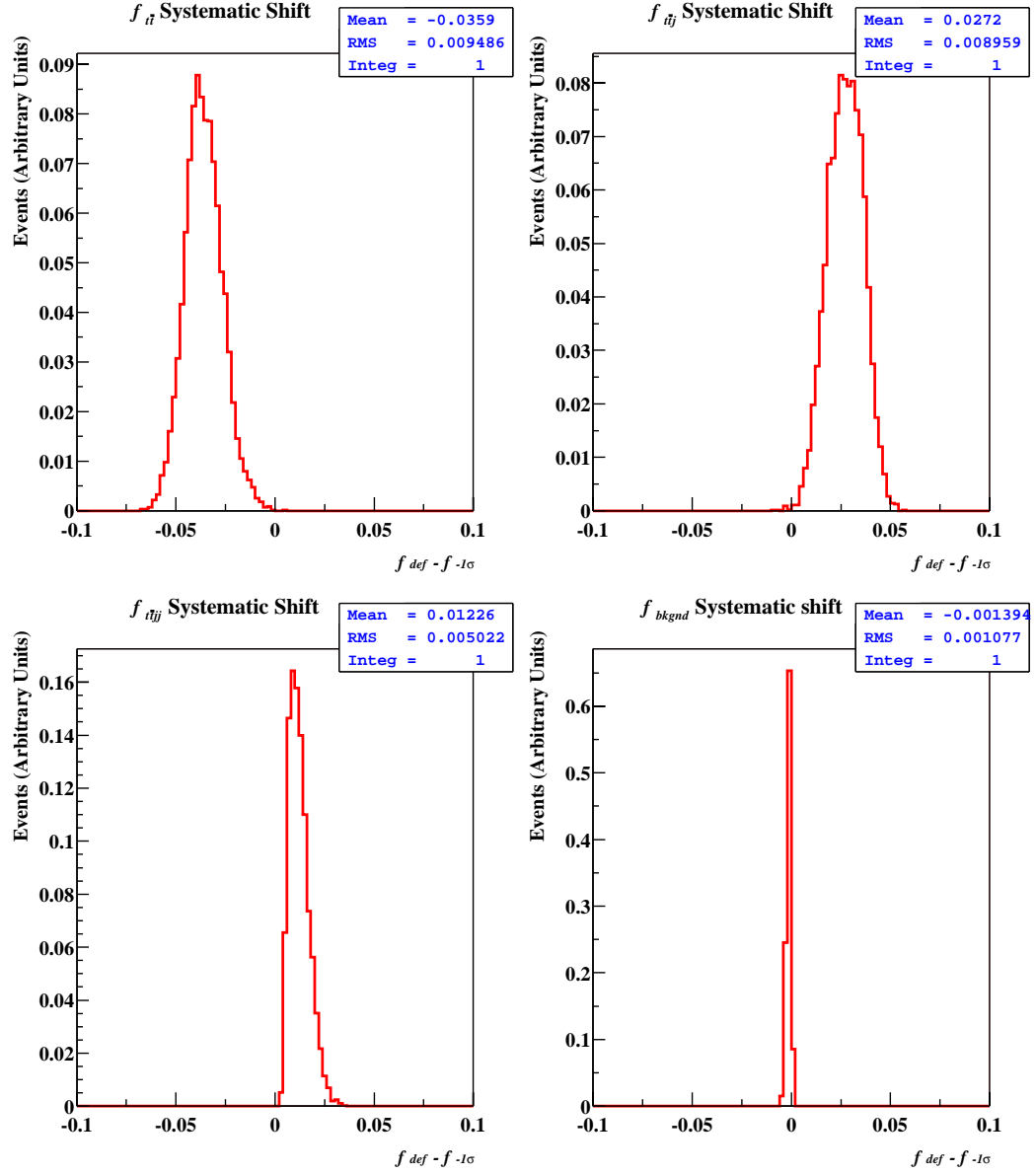
Figure 5.19: *Representative histogram of systematic shift induced in fitted fractions by changing jet energy down one standard deviation.*

E_T^{thresh}	Systematic	$\delta_{f_{t\bar{t}}}$	$\delta_{f_{t\bar{t}j}}$	$\delta_{f_{t\bar{t}jj}}$	$\delta_{f_{bkgnd}}$
15 GeV	Jet Energy	±0.0700	±0.0332	±0.0116	±0.0104
	M_{top}	±0.0002	±0.0000	±0.0001	±0.0005
	μ	±0.0061	±0.0054	±0.0012	±0.0003
	PDF	±0.0105	±0.0080	±0.0025	±0.0000
	MC stats	±0.0033	±0.0032	±0.0011	±0.0009
	ΔR	±0.0108	±0.0066	±0.0045	±0.0001
	DPR	±0.0139	±0.0101	±0.0035	±0.0004
	TOTAL	±0.0733	±0.0368	±0.0132	±0.0105
20 GeV	Jet Energy	±0.0421	±0.0240	±0.0089	±0.0052
	M_{top}	±0.0031	±0.0000	±0.0001	±0.0005
	μ	±0.0050	±0.0054	±0.0012	±0.0003
	PDF	±0.0032	±0.0053	±0.0007	±0.0002
	MC stats	±0.0031	±0.0022	±0.0010	±0.0000
	ΔR	±0.0162	±0.0085	±0.0077	±0.0000
	DPR	±0.0089	±0.0057	±0.0025	±0.0003
	TOTAL	±0.0417	±0.0225	±0.0133	±0.0053
25 GeV	Jet Energy	±0.0503	±0.0120	±0.0082	±0.0125
	M_{top}	±0.0014	±0.0000	±0.0001	±0.0005
	μ	±0.0043	±0.0054	±0.0012	±0.0003
	PDF	±0.0006	±0.0001	±0.0006	±0.0000
	MC stats	±0.0054	±0.0024	±0.0015	±0.0007
	ΔR	±0.0187	±0.0081	±0.0102	±0.0001
	DPR	±0.0055	±0.0031	±0.0016	±0.0003
	TOTAL	±0.0544	±0.0159	±0.0133	±0.0125

Table 5.4: *Estimates of (absolute) systematic uncertainties for the $t\bar{t} + t\bar{t}j + t\bar{t}jj$ fit.*

E_T^{thresh}	Systematic	$\delta_{f_{t\bar{t}}}$	$\delta_{f_{t\bar{t}j}}$	$\delta_{f_{bkgnd}}$
15 GeV	Jet Energy	±0.0853	±0.0574	±0.0115
	M_{top}	±0.0004	±0.0001	±0.0001
	μ	±0.0091	±0.0075	±0.0005
	PDF	±0.0128	±0.0127	±0.0000
	MC stats	±0.0028	±0.0076	±0.0007
	ΔR	±0.0170	±0.0173	±0.0002
	DPR	±0.0186	±0.0176	±0.0004
	TOTAL	±0.0904	±0.0647	±0.0115
20 GeV	Jet Energy	±0.0527	±0.420	±0.0058
	M_{top}	±0.0042	±0.0001	±0.0001
	μ	±0.0043	±0.0075	±0.0005
	PDF	±0.0059	±0.0026	±0.0000
	MC stats	±0.0064	±0.0058	±0.0002
	ΔR	±0.0188	±0.0191	±0.0001
	DPR	±0.0123	±0.0111	±0.0005
	TOTAL	±0.0516	±0.0404	±0.0058
25 GeV	Jet Energy	±0.0642	±0.0315	±0.0136
	M_{top}	±0.0004	±0.0001	±0.0001
	μ	±0.0075	±0.0075	±0.0005
	PDF	±0.0002	±0.0008	±0.0001
	MC stats	±0.0095	±0.0071	±0.0010
	ΔR	±0.0280	±0.0284	±0.0002
	DPR	±0.0073	±0.0062	±0.0004
	TOTAL	±0.0715	±0.0441	±0.0136

Table 5.5: *Estimates of (absolute) systematic uncertainties for the $t\bar{t} + t\bar{t}j$ fit.*

E_T^{thresh}	Systematic	$\delta_{f_{t\bar{t}}}$	$\delta_{f_{bkgnd}}$
15 GeV	Jet Energy	±0.0133	±0.0055
	M_{top}	±0.0003	±0.0000
	μ	±0.0001	±0.0006
	PDF	±0.0030	±0.0011
	MC stats	±0.0016	±0.0006
	ΔR	±0.0000	±0.0000
	DPR	±0.0038	±0.0015
	TOTAL	±0.0142	±0.0059
20 GeV	Jet Energy	±0.0101	±0.0041
	M_{top}	±0.0011	±0.0000
	μ	±0.0001	±0.0006
	PDF	±0.0019	±0.0007
	MC stats	±0.0009	±0.0004
	ΔR	±0.0000	±0.0000
	DPR	±0.0020	±0.0008
	TOTAL	±0.0078	±0.0032
25 GeV	Jet Energy	±0.0220	±0.0091
	M_{top}	±0.0006	±0.0000
	μ	±0.0009	±0.0006
	PDF	±0.0003	±0.0000
	MC stats	±0.0005	±0.0003
	ΔR	±0.0002	±0.0000
	DPR	±0.0010	±0.0004
	TOTAL	±0.0221	±0.0092

Table 5.6: *Estimates of (absolute) systematic uncertainties for the DPR only fit.*

where

$A_{t\bar{t}X} \equiv$ the combined geometric and kinematic acceptance

$\epsilon_{|z_{vtx}|} \equiv$ the efficiency of the cut on the primary vertex

$\epsilon_{trigger} \equiv$ the efficiency of the high p_T lepton triggers

$\epsilon_{tag} \equiv$ the efficiency for b-tagging at least one jet

In this analysis, however, the goal is not to calculate a cross-section, but rather a cross-section ratio:

$$\frac{\sigma_{t\bar{t}j}}{\sigma_{t\bar{t}X}} = \frac{N_{t\bar{t}j}/[(A_{t\bar{t}j} \cdot \epsilon_{|z_{vtx}|} \cdot \epsilon_{trig} \cdot \epsilon_{leptonid} \cdot \epsilon_{tag}) \cdot \int \mathcal{L}dt]}{N_{t\bar{t}X}/[(A_{t\bar{t}X} \cdot \epsilon_{|z_{vtx}|} \cdot \epsilon_{trig} \cdot \epsilon_{leptonid} \cdot \epsilon_{tag}) \cdot \int \mathcal{L}dt]} \tag{5.12}$$

which has the nice feature that many of the terms in the efficiency can, in principle, cancel each other out. In fact, *a priori*, it appears that, due to the very similar event topologies of the $t\bar{t}j, t\bar{t}X$ processes, in the current analysis, this cancellation may be maximal. In fact, it is only the acceptance, defined by:

$$A \equiv \epsilon_{lep} \cdot \epsilon_{\not{E}_T} \cdot \epsilon_{2j} \cdot \epsilon_{rem} \tag{5.13}$$

with

$\epsilon_{lep} \equiv$ the efficiency of lepton id cuts of sections 4.3,4.4

$\epsilon_{\not{E}_T} \equiv$ the efficiency of the missing transverse energy cut in section 4.5

$\epsilon_{2j} \equiv$ the efficiency of the 2 jet cut in section 4.8

$\epsilon_{rem} \equiv$ the efficiency of the Z, dilepton, and cosmic removals in sections 4.6,4.7

where there could be a process dependent efficiency. This acceptance was computed

Fit	E_T^{thresh}	$A_{t\bar{t}j}$	$A_{t\bar{t}X}$
$t\bar{t} + t\bar{t}j + t\bar{t}jj$	15 GeV	0.8065 ± 0.0028	0.8067 ± 0.0026
	20 GeV	0.8065 ± 0.0028	0.8068 ± 0.0025
	25 GeV	0.8065 ± 0.0028	0.8068 ± 0.0025
$t\bar{t} + t\bar{t}j$	15 GeV	0.8065 ± 0.0028	0.8068 ± 0.0025
	20 GeV	0.8065 ± 0.0028	0.8069 ± 0.0025
	25 GeV	0.8065 ± 0.0028	0.8069 ± 0.0024

Table 5.7: *Acceptance for $t\bar{t}j, t\bar{t}X$.*

for $t\bar{t}$ and $t\bar{t}X$[13] and the results tabulated in Table 5.7. The acceptances are equal within errors. Thus, the relative cross-section is simply given by the fitted fraction $f_{t\bar{t}j}$:

$$\frac{\sigma_{t\bar{t}j}}{\sigma_{t\bar{t}X}} = \frac{f_{t\bar{t}j}}{1 - f_{bkgnd}} \tag{5.14}$$

The resulting $t\bar{t}j$ cross-section ratio for each of the three E_T^{thresh} choices is given in Table 5.8 for both the $t\bar{t} + t\bar{t}j$ and $t\bar{t} + t\bar{t}j + t\bar{t}jj$ fits.

5.7 Limits using Feldman-Cousins Technique

As mentioned in section 5.4, the errors quoted above are those calculated by the likelihood-ratio approximation algorithm MINOS. This is an approximation which may

[13]$t\bar{t}X$ is taken to be composed of $t\bar{t}$ and $t\bar{t}j$ in the fractions found by the fits.

Fit	E_T^{thresh}	Cross-Section Ratio
$t\bar{t} + t\bar{t}j + t\bar{t}jj$	15 GeV	$0.0622^{+0.1205}_{-0.1613}(stat.) \pm 0.0750(sys.)$
	20 GeV	$0.0964^{+0.0986}_{-0.1096}(stat.) \pm 0.0472(sys.)$
	25 GeV	$0.0974^{+0.0967}_{-0.1072}(stat.) \pm 0.0350(sys.)$
$t\bar{t} + t\bar{t}j$	15 GeV	$0.0927^{+0.2160}_{-0.1789}(stat.) \pm 0.1322(sys.)$
	20 GeV	$0.1073^{+0.1781}_{-0.1264}(stat.) \pm 0.0847(sys.)$
	25 GeV	$0.1450^{+0.2019}_{-0.1478}(stat.) \pm 0.0973(sys.)$

Table 5.8: *Cross-section ratio $t\bar{t}j/t\bar{t}X$ as a function of E_T^{thresh}. Statistical and systematic errors included.*

encounter difficulties near a physical boundary. These difficulties can be statistical (*e.g.* incomplete coverage of the confidence interval) and/or interpretational (*e.g.* an unphysical error - a negative mass). In the current analysis, the measured cross-section ratios are sufficiently close to the physical boundary of zero that the latter difficulty manifests itself. One natural approach when a measured value is close to a physical boundary is to report a one-sided confidence interval, an upper limit in the current case. Unfortunately, if the decision to report a one-sided versus two-sided confidence is based on the data (as would be the case in this analysis), these limits will not yield complete coverage either[37]. The "unified approach" developed by Feldman and Cousins offers a remedy to this dilemma. The Feldman-Cousins algorithm always yields a physically allowable confidence interval, and still maintains

complete coverage whether a one-sided, or two-sided interval is preferred by the data.

Feldman-Cousins confidence intervals of 1 sigma, 90%, and 95% were constructed for the $t\bar{t} + t\bar{t}j$ fit for each of the three E_T^{thresh} choices. The details of these constructions are given in Appendix F. The resulting confidence intervals are shown in Figures 5.20,5.21,and 5.22. From these, the following 90% C.L. upper limits are obtained on the cross-section ratio $\sigma_{t\bar{t}j}/\sigma_{t\bar{t}X}$ for $E_T^{thresh} = 15$, 20, 25 GeV.

- $\left(\frac{\sigma_{t\bar{t}j}}{\sigma_{t\bar{t}X}}\right)_{E_T^{thresh}=15GeV} \leq 0.425$ (90% C.L.)

- $\left(\frac{\sigma_{t\bar{t}j}}{\sigma_{t\bar{t}X}}\right)_{E_T^{thresh}=20GeV} \leq 0.400$ (90% C.L.)

- $\left(\frac{\sigma_{t\bar{t}j}}{\sigma_{t\bar{t}X}}\right)_{E_T^{thresh}=25GeV} \leq 0.460$ (90% C.L.)

Feldman-Cousins Confidence Intervals

Figure 5.20: *Feldman-Cousins 1 sigma (light band), 90% (grey band), and 95% (dark band) Confidence Intervals for $t\bar{t} + t\bar{t}j$ fit, $E_T^{thresh} = 15$ GeV. The dashed line is drawn at the value of x obtained from the CDF data.*

Feldman-Cousins Confidence Intervals

Figure 5.21: *Feldman-Cousins 1 sigma (light band), 90% (grey band), and 95% (dark band) Confidence Intervals for $t\bar{t} + t\bar{t}j$ fit, $E_T^{thresh} = 20$ GeV. The dashed line is drawn at the value of x obtained from the CDF data.*

Feldman-Cousins Confidence Intervals
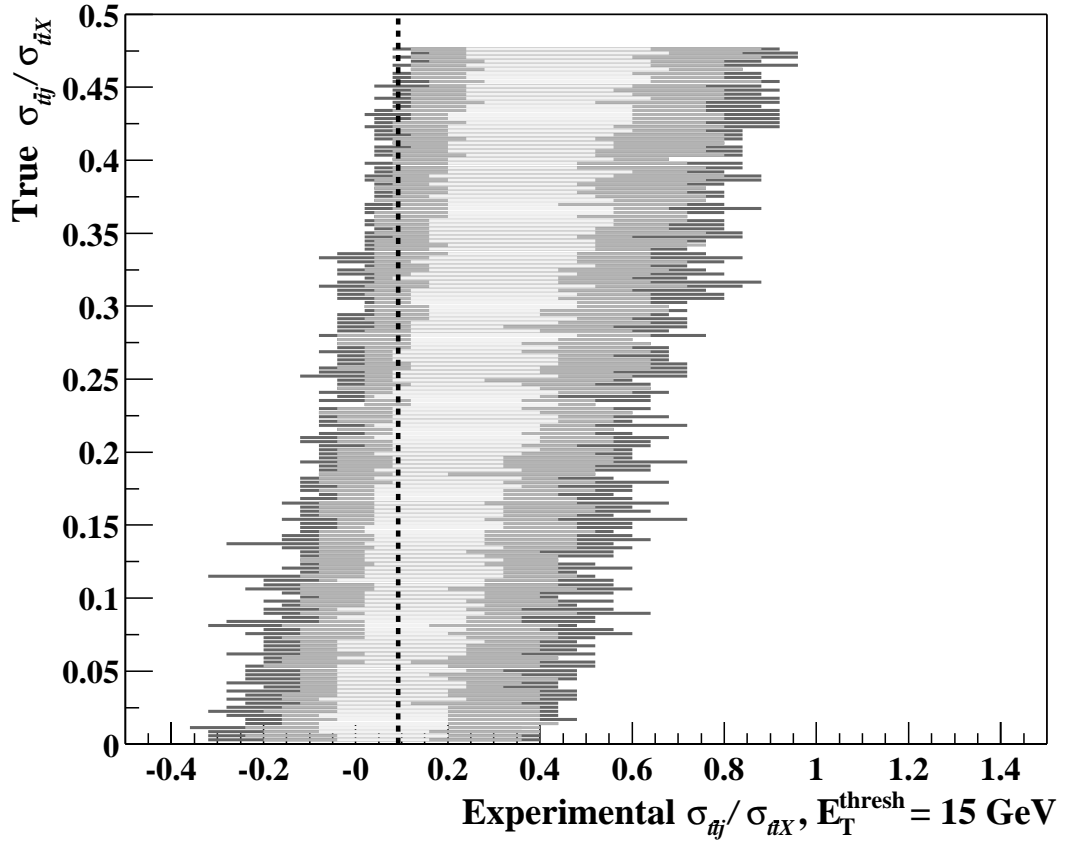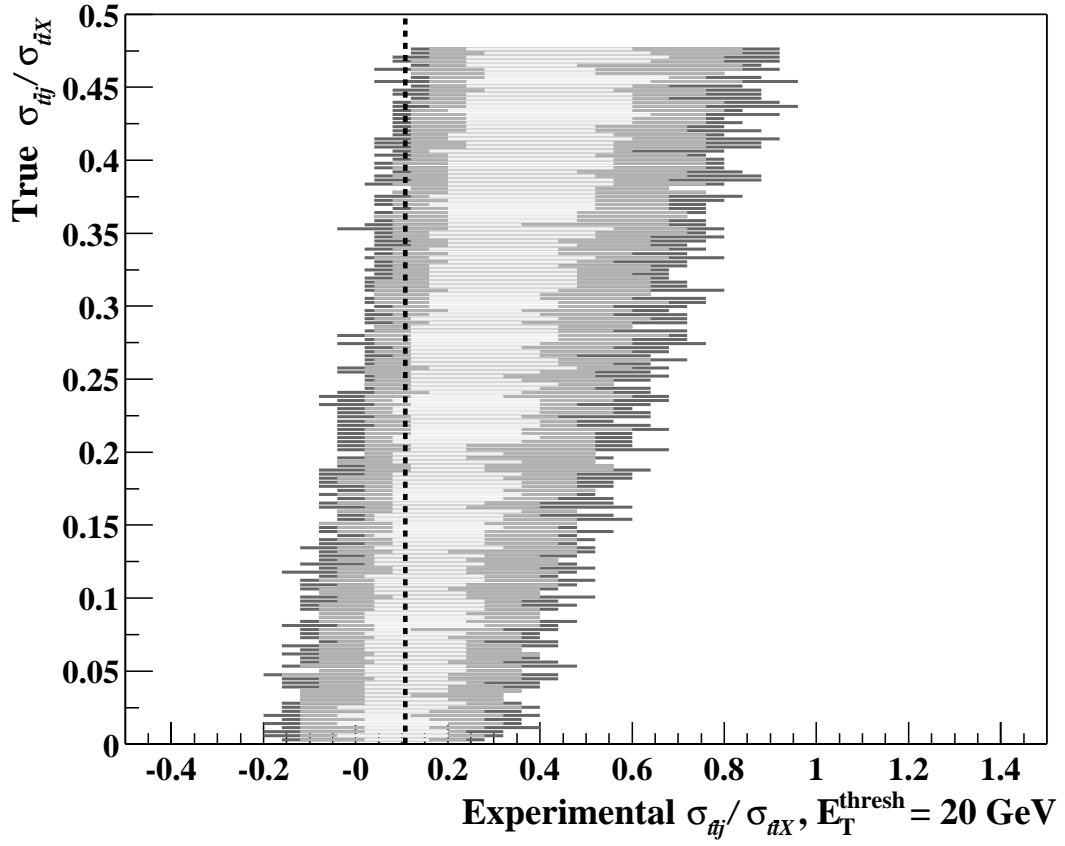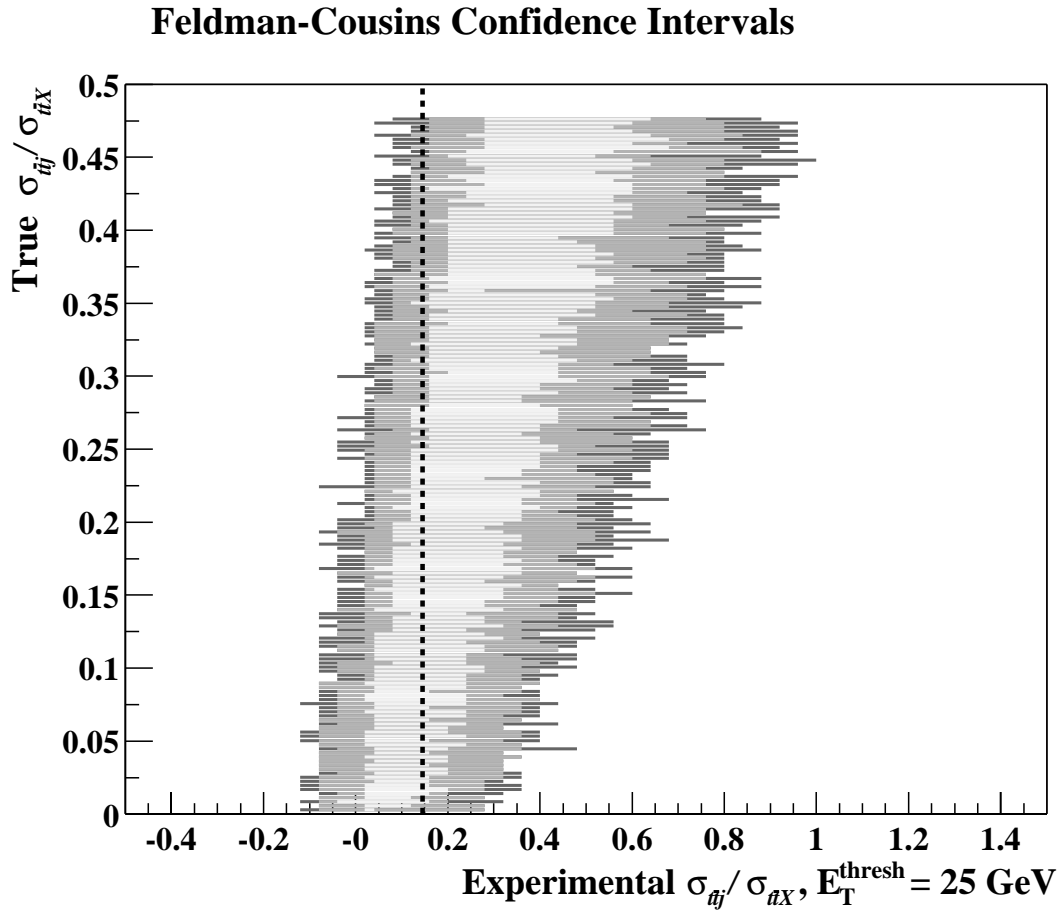

Figure 5.22: *Feldman-Cousins 1 sigma (light band), 90% (grey band), and 95% (dark band) Confidence Intervals for $t\bar{t}+t\bar{t}j$ fit, $E_T^{thresh} = 25$ GeV. The dashed line is drawn at the value of x obtained from the CDF data.*

Chapter 6

Comparison to Theory

6.1 Theoretical Expectation

Having measured the cross-section ratio $\sigma_{t\bar{t}j}/\sigma_{t\bar{t}X}$ from the CDF Run 1A+1B data, I compare this measurement to that predicted from theory.

The exact LO `MADGRAPH`[32] matrix elements used in this study (described in sub-section 5.2.1) predict the following cross-section ratios[1] using CTEQ4L for the parton distribution functions, and M_{top} as the renormalization scale:

$$\left(\frac{\sigma_{t\bar{t}j}}{\sigma_{t\bar{t}X}}\right)_{E_T^{thresh}=15GeV} = 0.2950 \pm 0.1180$$

$$\left(\frac{\sigma_{t\bar{t}j}}{\sigma_{t\bar{t}X}}\right)_{E_T^{thresh}=20GeV} = 0.2250 \pm 0.0900$$

$$\left(\frac{\sigma_{t\bar{t}j}}{\sigma_{t\bar{t}X}}\right)_{E_T^{thresh}=25GeV} = 0.1775 \pm 0.0710$$

The errors quoted above are due to the uncertainty in the choice of renormalization scale.

Within the errors of the measurement, and the errors on the prediction, the theoretical prediction is consistent with the experimental result. For comparison, the measured and predicted cross-section ratios are plotted overlaid as a function of E_T^{thresh} in Figure 6.1.

---

[1] $\sigma_{t\bar{t}j}$ is calculated from the matrix elements by Monte Carlo methods, and $\sigma_{t\bar{t}X}$ is taken to be the NNLO top cross-section calculated by Kidonakis[38].
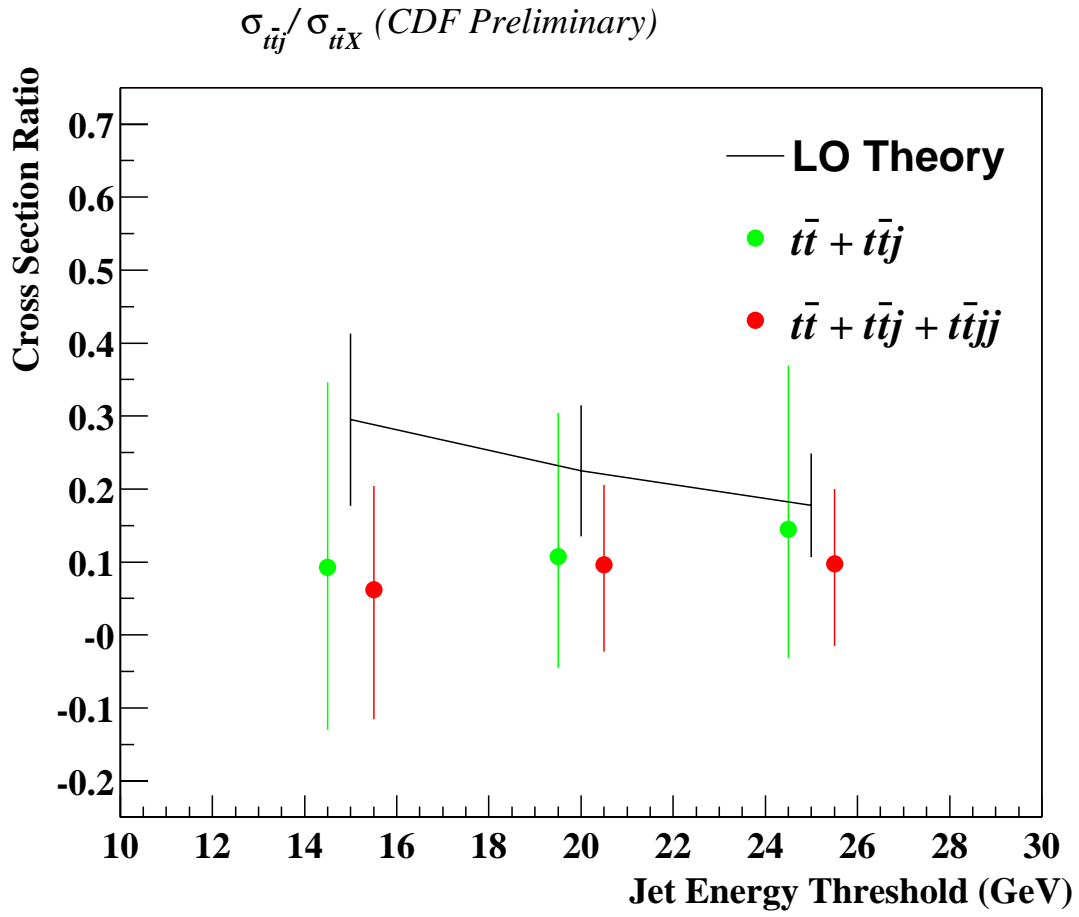
Figure 6.1: *Measured and predicted $t\bar{t}j/t\bar{t}X$ cross-section ratios as a function of E_T^{thresh}*

Chapter 7

Conclusions

7.1 Conclusions

The production cross section ratio $\frac{\sigma_{t\bar{t}j}}{\sigma_{t\bar{t}X}}$ has been measured from 106.0 ± 4.1 pb^{-1} of data collected by CDF during Run1A and Run1B of the Tevatron in the lepton + jets channel using SVX tags for jet counting thresholds of 15, 20, and 25 GeV corrected E_T. This was done with and without the assumption of the $t\bar{t}jj$ process, with the result that inclusion of $t\bar{t}jj$ process, while not inconsistent with the data, appears to be unnecessary. The cross section ratio assuming only the $t\bar{t}j$ process is measured to be:

- $(\frac{\sigma_{t\bar{t}j}}{\sigma_{t\bar{t}X}})_{E_T^{thresh}=15GeV} = 0.0927^{+0.2160}_{-0.1789}(stat.) \pm 0.1322(sys.)$

- $(\frac{\sigma_{t\bar{t}j}}{\sigma_{t\bar{t}X}})_{E_T^{thresh}=20GeV} = 0.1073^{+0.1781}_{-0.1264}(stat.) \pm 0.0847(sys.)$

- $(\frac{\sigma_{t\bar{t}j}}{\sigma_{t\bar{t}X}})_{E_T^{thresh}=25GeV} = 0.1450^{+0.2019}_{-0.1478}(stat.) \pm 0.0973(sys.)$

It was not possible, however, to exclude the possibility that the radiation was due to the decay phase only.

The above cross-section ratios have been compared to LO theoretical predictions. Agreement within errors is found.

Feldman-Cousins confidence intervals were constructed for the $t\bar{t} + t\bar{t}j$ fit for each of the three E_T^{thresh} choices. From these, the following 90% C.L. upper limits were obtained on the cross-section ratio $\sigma_{t\bar{t}j}/\sigma_{t\bar{t}X}$ for $E_T^{thresh} = 15$, 20, 25 GeV.

- $\left(\frac{\sigma_{t\bar{t}j}}{\sigma_{t\bar{t}X}}\right)_{E_T^{thresh}=15 GeV} \leq 0.425$ (90% C.L.)

- $\left(\frac{\sigma_{t\bar{t}j}}{\sigma_{t\bar{t}X}}\right)_{E_T^{thresh}=20 GeV} \leq 0.400$ (90% C.L.)

- $\left(\frac{\sigma_{t\bar{t}j}}{\sigma_{t\bar{t}X}}\right)_{E_T^{thresh}=25 GeV} \leq 0.460$ (90% C.L.)

The limited sensitivity of this measurement is due entirely to the small sample of top events collected by CDF during Run 1A+1B of the Tevatron. Errors in this measurement are dominantly statistical for the same reason. Run 2A of the Tevatron has recently begun and CDF is scheduled to collect 20 times the data of Run 1A+1B before its completion in $\sim$ 2004. Moreover, the Tevatron is now colliding beams at $\sqrt{s} = 2.0$ TeV, which yields a higher cross-section for top production. Finally, CDF has a new detector with an appreciably larger acceptance for b-quarks and leptons, which results in a higher detection efficiency for top events. Combining these effect, CDF expects to detect 40 times the number of tops in Run 1A+1B in Run 2A.

The expected performance of this analysis on this larger dataset is studied on pseudo-experiments of simulated Run 2A data and is presented in Appendix E. It is found that with the increased statistics of Run 2A, this analysis will have the sensitivity to conclusively reject the decay-phase radiation only hypothesis. It will also have significant ability to distinguish between $t\bar{t}j$ and $t\bar{t}jj$ events. With this added discernibility, the application of the measurement result to top mass reconstruction, as a means of constraining renormalization scale choice in the $t\bar{t}$ + jets calculations,

and as background to $t\bar{t}H$ as discussed in subsection 2.2.4 will be possible.

Appendix A

List of Selected Events

Run	Event	Primary Lepton
40190	98182	e
41627	87219	e
47439	128290	e
45776	386857	e
46357	511399	μ
47689	80060	μ
60766	299452	e
61167	368226	e
63883	935	e
64126	52063	e
64916	499208	e
64997	46557	e
65022	34157	e
65298	907072	e
65384	266051	e

Table A.1: *Run 1A+1B W + 2j events passing all cuts*

Run	Event	Primary Lepton
65470	4390	e
66103	563542	e
66412	121506	e
67692	420568	e
68044	53510	e
68374	364586	e
69520	136405	e
69683	21986	e
69709	173294	e
68464	275644	e
60705	93795	μ
61377	114526	μ
63603	4029	μ
63946	43019	μ
65741	654870	μ

Table A.2: *Run 1A+1B W + 2j events passing all cuts* cont.

Run	Event	Primary Lepton
65750	106257	μ
66103	743101	μ
66518	203555	μ
68231	157759	μ
68423	3326	μ
68593	37659	μ
68637	225974	μ
68774	150313	μ
69498	36574	μ
69761	157205	μ
TOTAL	40	

Table A.3: *Run 1A+1B W + 2j events passing all cuts* cont.

Run	Event	Primary Lepton
46269	44897	e
43096	47223	e
46818	221912	μ
61074	103772	e
64934	416715	e
66573	107219	e
67824	281883	e
67899	82457	e
70627	56836	e
56911	114159	e
59124	31243	μ
61548	284898	μ
65025	152	μ
65277	209495	μ
67879	407958	μ
67971	55023	μ
TOTAL	16	

Table A.4: *Run 1A+1B W + 3j events passing all cuts*

Run	Event	Primary Lepton
40758	44414	e
45879	123158	μ
59698	31639	e
63247	65096	e
63641	3054	e
68006	44672	e
69683	135095	e
68464	547303	e
64811	438617	μ
67515	298909	μ
68312	821014	μ
68739	425355	μ
69781	266905	μ
56669	21631	μ
TOTAL	14	

Table A.5: *Run 1A+1B $W+ \geq 4j$ events passing all cuts*

Appendix B

List of Level 2 Triggers Used in Data Selection

Run	Lepton	Trigger
1A	e	CEM_9*
1A	e	MET_20*
1A	μ	MET_35_TEX*
1A	μ	MET_35_TWO*
1A	μ	CMU_CMP_CFT_9_2*
1A	μ	CMNP_CFT_9_2*
1A	μ	CMUP_CFT_9_2*
1A	μ	CMX_CFT_9_2*
1A	μ	CMX_CFT_9_2_ET*
1A	μ	CMX_CFT_9_2_V5*

Table B.1: *Level 2 triggers required for Run 1A*

Run	Lepton	Trigger
1B	e	CEM_16_CFT_12*
1B	e	MET_20*
1B	μ	MET_35_TEX*
1B	μ	MET_35_TWO*
1B	μ	CMNP_CFT_12_5DEG_V*
1B	μ	CMUP_CFT_12_5DEG_V*
1B	μ	CMNP_JET*
1B	μ	CMU_CMP_JET*
1B	μ	CMNP_CFT_12_5DEG_M*
1B	μ	CMUP_CFT_12_5DEG_M*
1B	μ	CMX_CFT_12_5DEG_V*
1B	μ	CMX_JET*
1B	μ	CMX_CFT_12_5DEG_M*
1B	μ	CMX_CFT_12_5DEG_E*

Table B.2: *Level 2 triggers required for Run 1B*

Appendix C

Choice of p_T^{min} and $\Delta R(gg)^{min}$ in Matrix Elements

As mentioned in section 5.2.1, it is necessary to place a lower limit on the momentum of the gluon(s) in the $t\bar{t}g$, $t\bar{t}gg$ matrix elements to remove the soft singularity. Any value greater than zero will suffice to accomplish this removal. Beyond this, where the cutoff is placed depends on how one intends to use the Monte Carlo. For example, if one wishes to normalize to the inclusive cross section and thereby obtain a matrix element corrected Monte Carlo estimate of inclusive $t\bar{t}$ production (as a background estimate for, say, a single-top measurement), one would have to impose the cutoff, $p_T^{min} \simeq 3$ GeV, as below this value the cross-section given by the matrix element exceeds the CDF inclusive measurement[1]. In this analysis, however, where the matrix elements are being used to generate jet multiplicity shapes without regard to normalization, this cutoff requirement is unnecessarily low. The standard calorimeter cluster

---

[1]A parton shower model, like that employed by PYTHIA must take over below this threshold via some smooth transition. This is just what Dave Rainwater and I have planned for a more general release of this MC.

threshold employed in CDF being 7 GeV uncorrected E_T, analyses (such as this one)
that utilize this algorithm are insensitive to 3 GeV parton-level energy gluons. In fact,
as can be seen from Figure C.1 which plots the corrected E_T spectrum of all jets in
$t\bar{t}j$ events, this insensitivity extends up to 12 GeV in corrected E_T. For this analysis,
though, there exists another concern. To ensure that feed-up/feed-down in jet energy
due to detector effects is properly taken into account (via $\texttt{QFL}'$), one must generate
Monte Carlo events sufficiently below the threshold at which one counts jets. The
cutoff of $p_T^{min} = 10$ GeV is a conservatively chosen balance between this concern and
the above inefficiency. The choice of $\Delta R(gg)^{min}$ to remove the collinear singularity in
the $t\bar{t}gg$ matrix element is similar, but simpler. Any non-zero choice is sufficient, but
since this analysis uses a cone size of 0.4 to cluster jets, it is not sensitive to gluons
separated by $\Delta R < 0.4$, hence $\Delta R(gg)^{min} < 0.4$ is needlessly inefficient. A choice of
$\Delta R(gg)^{min} > 0.4$ would introduce a bias toward event topologies with well separated
jets. Thus, the choice $\Delta R(gg)^{min} = 0.4$ is made to avoid bias, yet remain efficient in
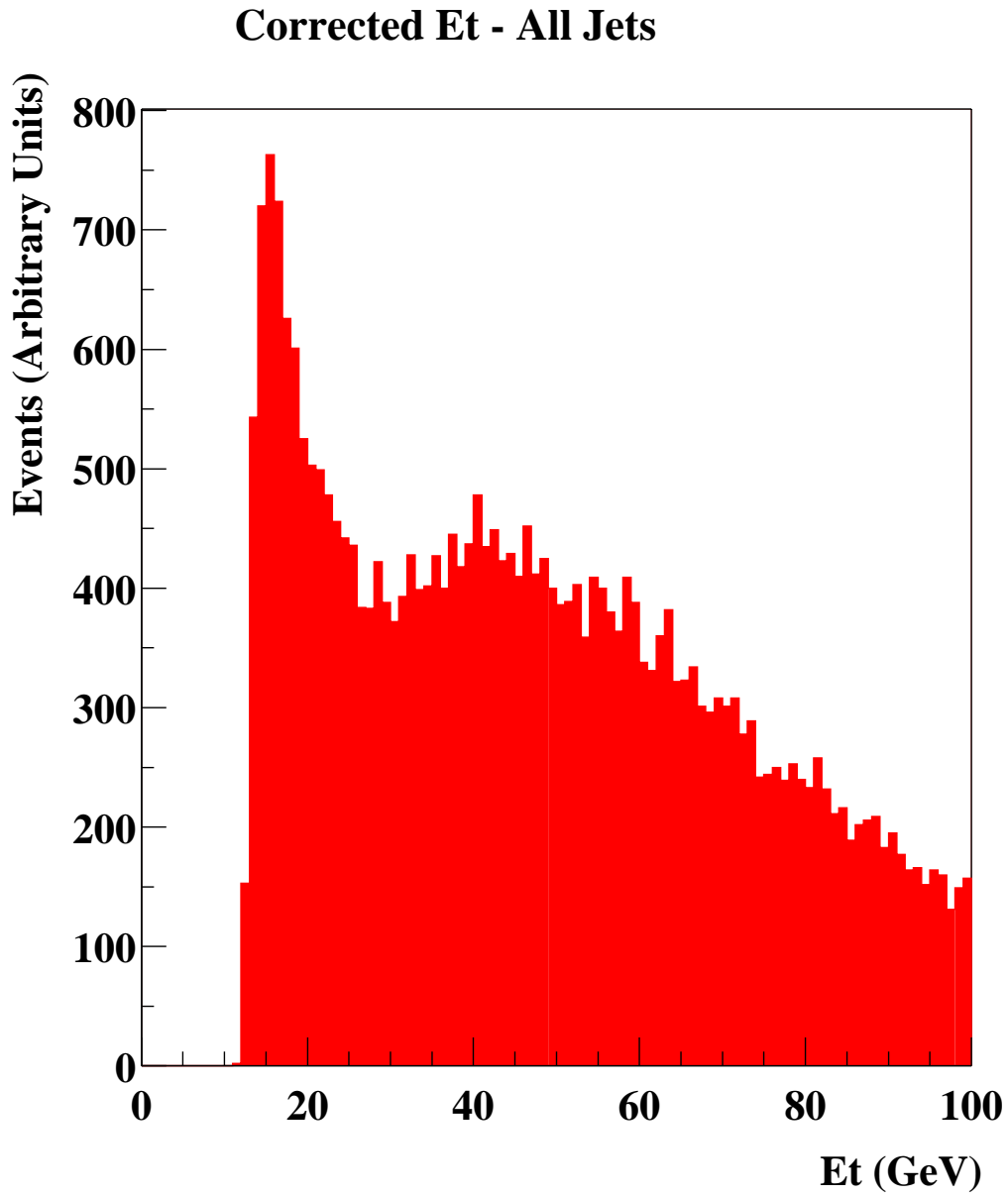generation of the $t\bar{t}jj$ templates.

Corrected Et - All Jets

Figure C.1: *Corrected E_T spectrum, all jets, from $t\bar{t}j$ MC.*

Appendix D

Choice of ΔR cut in Matching Gluons to Jets

To identify the jet that resulted from the gluon(quark) in a $t\bar{t}j, t\bar{t}jj$ event, ΔR is computed between the parton-level momentum vector of the gluon(quark) and the jet-axes of all jets in the event after `QFL`$'$ simulation. The results of this computation are shown for $t\bar{t}j$ events in the top plot of Figure D.1. The peak at low ΔR is occurs when the momentum vectors of the gluon(quark) and it's corresponding jet are aligned. The width of this peak indicates typical ΔR values of such an aligned gluon(quark)-jet pair, suggesting a matching requirement of 0.5 in ΔR which is chosen. The effect of this choice will is studied as a systematic error.

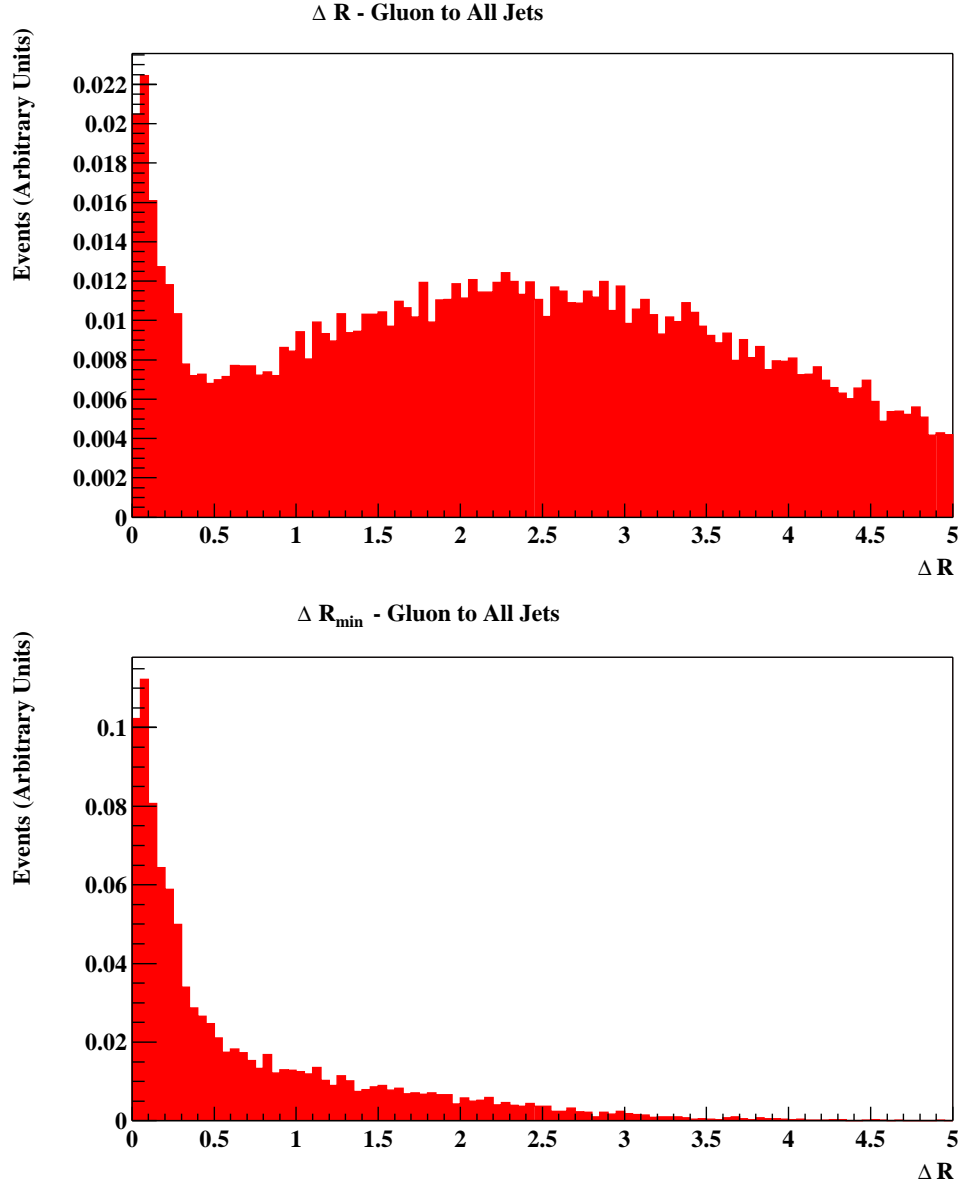Figure D.1: *Plots of ΔR between parton level momentum and reconstructed jet axes. Top plot is ΔR between the gluon and all other jets in the event. The lower plot is ΔR between the gluon and the one jet to which it matched best.*

Appendix E

Expected Performance in Run 2A

10,000 pseudo-experiments were generated in the manner described in section 5.3, except that the signal and background amounts were increased by a factor of 40, which is a conservative estimate of the top dataset that CDF expects to collect in Run 2A due to increases in luminosity, cross-section, and acceptance. The fit described in section 5.1.1 is then performed on each of these 10,000 pseudo-experiments. The resulting distributions of the fit parameters are shown in Figure E.1. Note, that with the increased statistics, these distributions are considerably more narrow, and separated, than those shown previously in Figure 5.14. Consequently, the sensitivity of this analysis is expected to be enhanced greatly if repeated in Run 2A.

As a further test of the performance of this analysis with the increased statistics expected in Run 2A of the Tevatron, one of the 10,000 pseudo-experiments was selected at random and taken to be a simulated Run 2A CDF dataset. The three fits described in section 5.4 were applied to this simulated data. A jet multiplicity
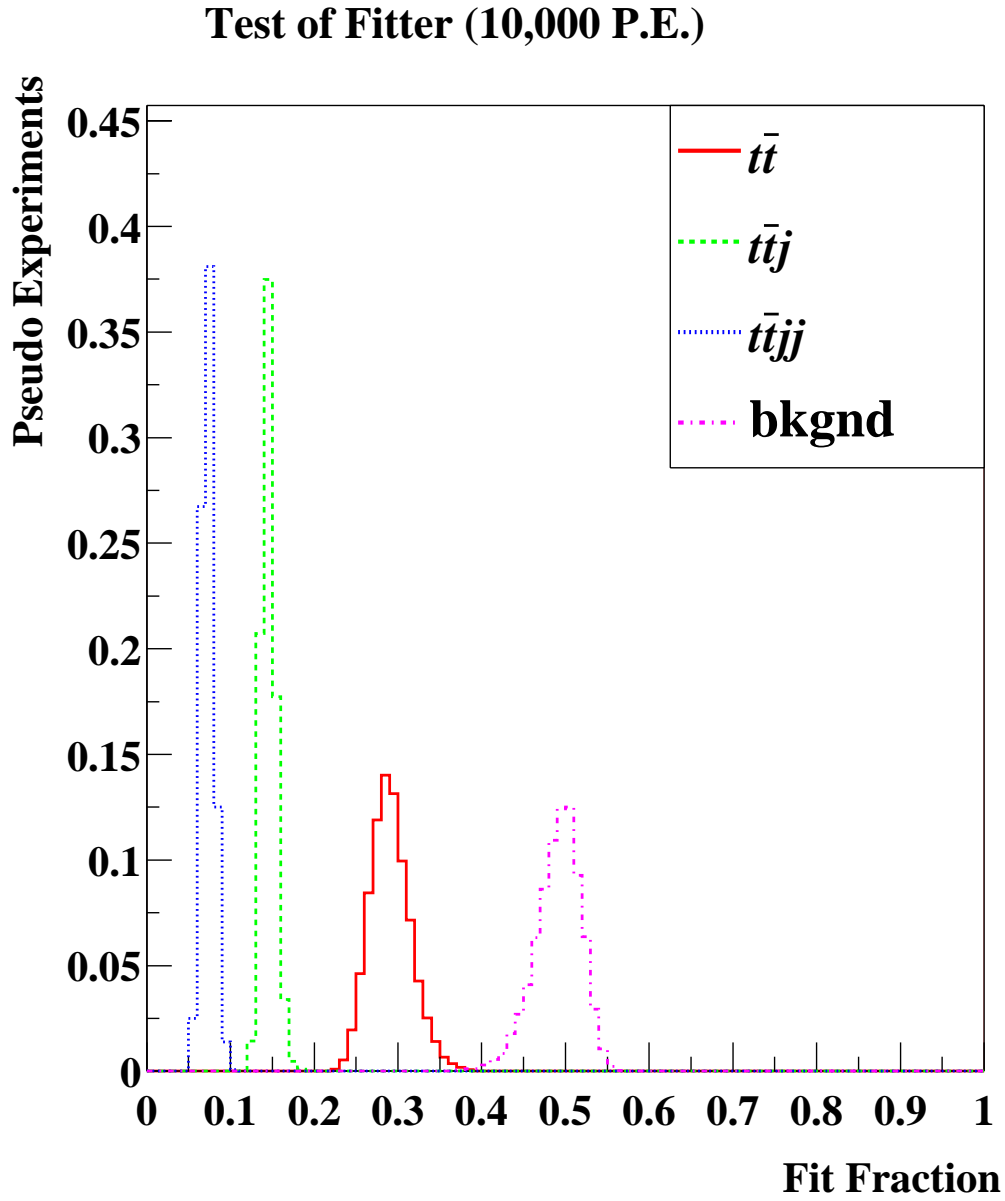
Figure E.1: *Distributions of fitted fractions for input values .2899, .1449, .0724, .4928 for $f_{t\bar{t}}, f_{t\bar{t}j}, f_{t\bar{t}jj}, f_{bkgnd}$ respectively with factor of 40 increase in statistics as is expected in Run 2a.*
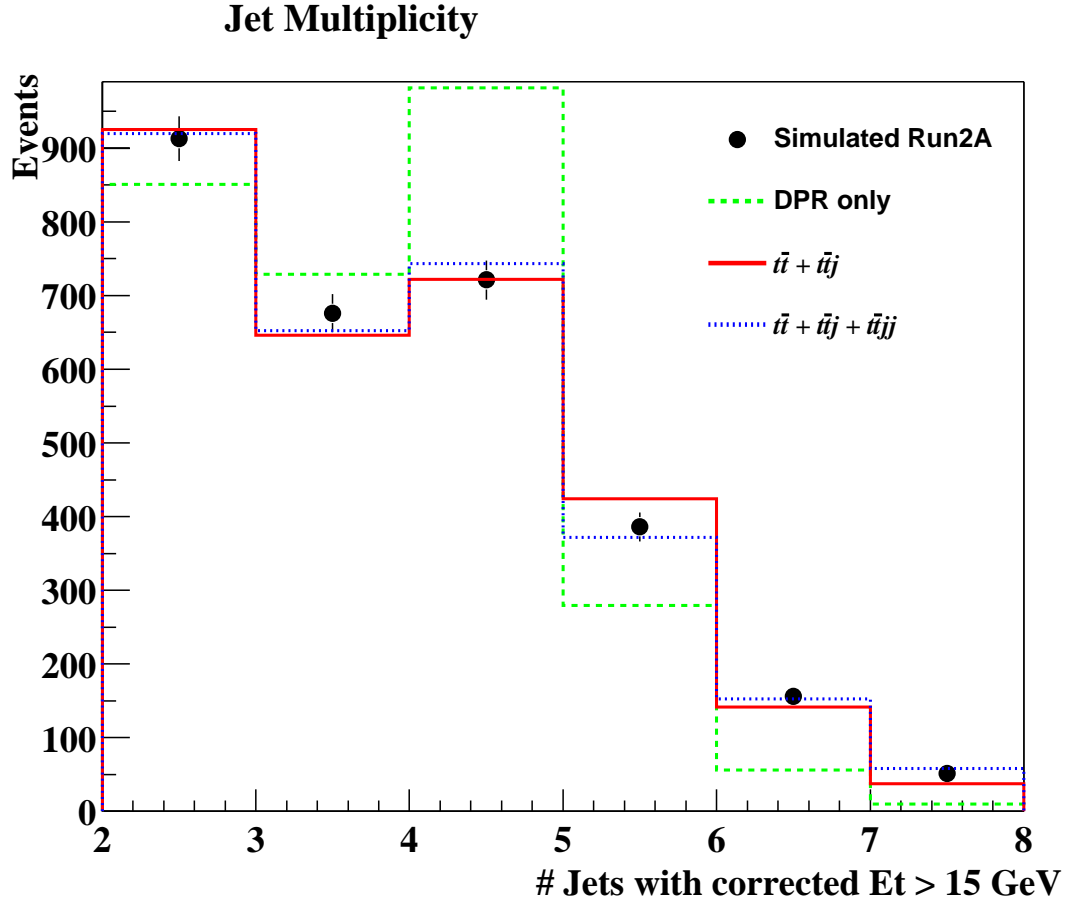
Figure E.2: *Simulated CDF Run 2A data jet multiplicity for jets with corrected $E_T > 15$ GeV, together with the DPR only, $t\bar{t} + t\bar{t}j$, and $t\bar{t} + t\bar{t}j + t\bar{t}jj$ fits overlaid.*

distribution of the simulated CDF data for a jet energy threshold of 15 GeV with each of the three fits overlaid is displayed in Figure E.2.

To evaluate the goodness-of-fit of the three fits performed on the simulated data, a χ^2 test is performed. The low expectation concerns raised in subsection 5.4.1 are not relevant here. The fit is over 6 bins. I fit for 3 parameters, so the fit has $6 - 3 = 3$ degrees of freedom.

The resulting reduced chi-squares and the accompanying confidence levels of the fits are given below:

- $E_T^{thresh} = 15$ GeV

  - DPR only fit: $\chi_\nu^2 = 76.578$, C.L. $= 0.00\%$

  - $t\bar{t} + t\bar{t}j$ fit: $\chi_\nu^2 = 3.3805$, C.L. $= 1.74\%$

  - $t\bar{t} + t\bar{t}j + t\bar{t}jj$ fit: $\chi_\nu^2 = 1.0602$, C.L. $= 36.46\%$

This pseudo-experiment was generated under the $t\bar{t} + t\bar{t}j + t\bar{t}jj$ hypothesis. This is consistent with the above numbers, which indicate for this pseudo-experiment we would be able to reject the DPR only and $t\bar{t} + t\bar{t}j$ hypotheses based on goodness-of-fit.

Thus, it can be seen that with the increased statistics of Run 2A, this analysis will be sensitive enough to distinguish between not only the DPR only hypothesis and the $t\bar{t} + t\bar{t}j$, $t\bar{t} + t\bar{t}j + t\bar{t}jj$ hypotheses (collectively), but also between the $t\bar{t} + t\bar{t}j$ and $t\bar{t} + t\bar{t}j + t\bar{t}jj$ hypotheses themselves.

Appendix F

Feldman-Cousins Limits

The construction of the Feldman-Cousins confidence intervals for a measured value, x_0, which is an estimator of the true but unknown physical quantity, μ proceeds by mapping out the two-dimensional space spanned by all possible experimental values of x, and all possible true values of μ. The two-dimensional $\mu - x$ space is mapped out by performing pseudo-experiments, $i.e.$ for a given μ, pseudo-experiments are performed to find all possible experimental values, x. In the context of the current analysis, μ is the cross-section ratio $\sigma_{t\bar{t}j}/\sigma_{t\bar{t}X}$. The procedure applied in this analysis, and resulting in the limits quoted in section 5.7, is described in what follows:

1. For $\mu = N_{t\bar{t}j}$ from 0.1 to 18.0 events $(\sigma_{t\bar{t}j}/\sigma_{t\bar{t}X} \approx 0\%$ to $50\%)$ 1,000 pseudo-experiments were generated in the manner described in section 5.3 for a total of 180,000 pseudo-experiments.

2. Each of the 180,000 pseudo-experiments were fit with the $t\bar{t} + t\bar{t}j$ fit, and the results histogrammed. This histogram is the distribution of all possible experi-

mental values x, for a given μ.

3. For each value of x, the μ for which the probability density $P(\mu|x)$ is greatest is found. This is denoted μ_{best}.

4. For each value of μ, the following ratio is computed for all x.

$$R(x) = \frac{P(x|\mu)}{P(x|\mu_{best})}$$

5. For each value of μ, x_1, x_2 are found such that the following expression is true, where α is the desired confidence level and $x_1 < x_2$ by construction.

$$R(x_1) = R(x_2) = \int_{x_1}^{x_2} P(x|\mu)dx = \alpha$$

6. The $x1, x2$ form horizontal bands which are plotted for each μ.

7. A limit is extracted by drawing a vertical line through the measured value, x_0, on the horizontal axis. The confidence interval for μ includes all values of μ for which this vertical line intercepts a horizontal band formed by a x_1, x_2 pair.

Bibliography

[1] M. Peskin, and D. Schroeder, *An introduction to Quantum Field Theory*, p. 198, Addison Wesley, 1995.

[2] S. Glashow, "Partial-Symmetries of Weak Interactions," Nucl. Phys. **22** (1961) 579.

[3] A. Salam, "Relativistic groups and analyticity," Proc 8th Nobel Symposium Aspenasgarden (1968) 367.

[4] S. Weinberg, "A Model of Leptons," Phys. Rev. Lett **19**(1967) 1264.

[5] UA1 Collaboration, "Experimental Observation of Isolated Large Transverse Energy Electrons with Associated Missing Energy at $\sqrt{s} = 540$ GeV," Phys. Lett. **B122** (1983) 103.

[6] UA1 Collaboration, "Experimental Observation of Lepton Pairs of Invariant Mass around 95 GeV/c^2 at the SPS Collider," Phys Lett. **B126** (1983) 398.

[7] UA2 Collaboration, "Evidence for $Z^0 \rightarrow e^+e^-$ at the CERN $\bar{p}p$ Collider," Phys. Lett. **B129** (1983) 130.

[8] http://http://www-visualmedia.fnal.gov/VMS_Site/v_photographs.html.

[9] W. Greiner and A. Schafer, *Quantum Chromodynamics*, p. 145. Springer ,1994.

[10] M.Drees and S. Martin, "Implications of SUSY Model Building," hep-ph/9504324 (1995).

[11] F. Abe *et. al.* (The CDF Collaboration), "Observation of Top Quark Production in $\bar{p}p$ Collisions with the CDF detector at Fermilab," Phys.Rev. Lett. **74**(1995) 2626.

[12] Bhat, Prosper and Snyder, "Top Quark Physics at the Tevatron", hep-ex/9809011 (1998).

[13] L.Orr and T. Stelzer, "Gluon Radiation in t anti-t Production at the Tevatron p anti-p Collider," Phys.Rev.D51:1077-1085 (1995).

[14] CDF Collaboration, "Measurement of the Top Quark Mass with the Collider Detector at Fermilab," Phys. Rev. D63:032003 (2001).

[15] J. Goldstein et al., Phys. Rev. Lett. **86**, 9 (2001).

[16] http://www-cdf.fnal.gov/grads/tips/thesis_tips.html#cdfpics.

[17] J.D. Jackson, *Classical Electrodynamics*, p. 718, John Wiley & Sons, 1975.

[18] Particle Data Group, Eur. Phys. J. C 3, 1-794 (1998).

[19] S.Belaforte et al., "σ_{BBC} Derivation and Results," CDF 2361 (1994).

[20] D.Cronin-Hennessy et al., "Luminosity at CDF," CDF 4721 (1998).

[21] Top Group, "Sample Selection for Run 1B Top Search," CDF 2966 (1996).

[22] D.Gerdes, "Study of Conversion Removal for the Lepton+Jets Sample," CDF 2903 (1995).

[23] G. Unal, "Background Summary for the top SVX Analysis," CDF 3389 (1995).

[24] G. Corcella and M.H. Seymour, "Matrix Element Corrections to Parton Shower Simulations of Heavy Quark Decay," hep-ph/9809451.

[25] F.A. Berends et al., "On the production of a W and jets at hadron colliders," Nucl. Phys B **357** 32 (1991).

[26] T. Sjostrand, Computer Physics Commun. **82** 74 (1994).

[27] P.Giromini et al., "Search for New Particles $X \rightarrow b\bar{b}$ Produced in Association with W Bosons at $\sqrt{s} = 1.8$ TeV," CDF 4112 (1997).

[28] L. Orr, Univ. of Rochester, private communication.

[29] D. Rainwater, FNAL Theoretical Physics, private communication.

[30] CERN Program Library, Minuit - function minimization and error analysis, D506.

[31] J.Andre and T.Sjostrand, "A Matching of Matrix Elements and Parton Showers," hep-ph/970839

[32] T. Stelzer and W.F. Long, Computer Physics Commun. **81** 357 (1994).

[33] A.Caner et al., "Jet Corrections for Top Mass Fitting," CDF 2469 (1994).

[34] W.G. Cochran, Annals of Mathematical Statistics, **23** 3 (1952).

[35] J.T. Roscoe and J.A. Byars, Journal of the American Statistical Association, **66** 336 (1971).

[36] D.Glenzinski., "Ttbar Acceptance Calculation for the Run1B SVX-Btag Analysis," CDF 3403(1995).

[37] G. Feldman and R. Cousins, Phys. Rev. D **57** 3873 (1998).

[38] N. Kidonakis, "Top Quark Total and Differential Cross Sections at NNLO and NNLL," hep-ph/0009013 (2000).